Fabrication and Evaluation of Polymer Nanocomposites for Space Radiation Shielding Application

by

Elahe Cheraghi

A thesis
presented to the University of Waterloo
in fulfillment of the
thesis requirement for the degree of
Doctor of Philosophy
in
Systems Design Engineering

Waterloo, Ontario, Canada 2022

Examining Committee Membership

The following served on the Examining Committee for this thesis. The decision of the Examining Committee is by majority vote.

External Examiner	Raghavan Jayaraman Associate Professor, Dept. of Mechanical Engineering, University of Manitoba
Supervisor(s)	John T.W. Yeow Professor, Dept. of Systems Design Engineering, University of Waterloo
Internal Member	Nasser Lashgarian Azad Associate Professor, Dept. of Systems Design Engineering, University of Waterloo
Internal Member	Nima Maftoon Assistant Professor, Dept. of Systems Design Engineering, University of Waterloo
Internal-external Member	Adrian Gerlich Professor, Dept. of Mechanical and Mechatronic Engineering, University of Waterloo

Author's Declaration

I hereby declare that I am the sole author of this thesis. This is a true copy of the thesis, including any required final revisions, as accepted by my examiners.

I understand that my thesis may be made electronically available to the public.

Abstract

Protecting astronauts and space crow from hazardous radiation is critical in space missions. Conventional metallic material such as aluminum (Al) and its alloys have been widely used for shielding the harmful space radiations, including high energy electrons. However, due to the issue of extra secondary radiation generation and heavy weight, metallic materials are not satisfying for modern applications and long-distance space missions. Among various materials for shielding the space radiations, low atomic-number materials, including hydrogen, are demonstrated as the most efficient materials; however, the feasibility and safety issues of these materials have limited their applications.

Employing hydrogen-rich polymer nanocomposites is one of the approaches to replace high atomic number metals. Polymer-based nanocomposites can provide enough shielding against hazardous radiations with less secondary radiation generation and lower weight, in addition to improved mechanical and physical properties. By reviewing literature, bismuth oxide (Bi_2O_3), multi-walled carbon nanotube (MWCNT), hexagonal-boron nitride (h-BN), and MXene nanomaterials were selected to enhance properties of polydimethylsiloxane (PDMS) polymer.

In first step, PDMS/Bi_2O_3 and PDMS/MWCNT nanocomposites with different weight percentages (wt.%) of nanofillers. Then, photon shielding effectiveness of fabricated nanocomposites were studied with utilizing diagnostic x-ray with 60, 70, 80, and 90 keV energies. Flexible thin multilayer nanocomposites with alternating PDMS/Bi_2O_3 and PDMS/MWCNT layers were fabricated and characterized.

Afterward, the role of nanofillers embedded in PDMS polymer matrix on shielding efficiency were studied by comparing the electron attenuation properties of PDMS/MWCNT, PDMS/Bi_2O_3, and PDMS/MWCNT/Bi_2O_3 nanocomposite with pure PDMS and Al. The results indicate that the addition of Bi_2O_3 and MWCNT in PDMS matrix can significantly improve the electron attenuation of the pure polymer. PDMS/MWCNT/Bi_2O_3 also has weight advantage in comparison with Al as it attenuates the same electron radiation energies with lower areal density. However, enhanced thermal and mechanical properties of the proposed nanocomposite are required to make it a promising candidate for electron radiation shielding in space applications. As a result, an

optimization of nanocomposites has been accomplished by applying it in a layered structure. For this purpose, hydrogenated boron nitride (OHBN) and the novel 2D nanomaterials, MXene, were added to PDMS polymer matrix separately. A multilayer nanocomposite of PDMC/BN, PDMS/MXene, and PDMS/MWCNT/Bi_2O_3 layers were developed with enhanced thermal and shielding properties. The developed multilayer structure was fabricated with 5 different areal densities and studied for high energy electron radiation attenuation, under electron beam with energies of 9, 12, 16, and 20 MeV. According to the high ratio of radiation shielding effectiveness and weight of the developed nanocomposite, it is highly potential to be applied as the space shielding material.

Acknowledgements

Firstly, I would like to mention my sincere gratitude to Professor John T.W. Yeow, my supervisor, for his encouragement and guidance through my PhD journey. He always helped me in all the time of my research with his immense knowledge and amazing support. I could not have imagined having a better advisor and mentor for my Ph.D. study.

I thank my kind colleagues in our lab and my lovely friends for their encourage and support during this wonderful journey. Special thanks to Dr. Siyuan (Johnny) Chen for all his support. During my PhD, there were many moments and many challenges that I could not overcome without Dr. Chen's help.

Lastly, I would like to thank my family for believing in me, trusting me, and giving me unconditional love and encouragement all the time.

Dedication

Dedicated to my parents, Hassan and Fezzeh.

Table of Content

List of Figures

List of Tables

List of Abbreviations

SPE	Solar Particle Events
GCR	Galactic Cosmic Rays
HZE	High Energy and Atomic Number Particles
TID	Total Ionization Dose
ISS	International Space Station
Z	Atomic Number
HDPE	High-Density Polyethylene Poly
PDMS	Polydimethylsiloxane
CNT	Carbon Nanotubes
MWCNT	Multi-Walled Carbon Nanotubes
-COOH	Carboxyl
h-BN	Hexagonal Boron Nitride
FBN	Functionalized Boron Nitride
LEO	Low-Earth-Orbit
CME	Coronal mass ejections
CTE	Coefficient of thermal expansion
GEO	Geostationary orbit
SEE	Single Event Effect
NCRP	National Council on Radiation Protection and Measurement
SEB	Single-Event Burnout
SEL	Single-Event Latch-Up
SEU	Single Event Upset
UHMW- HDPE	Ultrahigh Molecular Weight High Density Polyethylene
MMC	Metal Matrix Composite
PE	Polyethylene

PMMA	Poly (Methyl Methacrylate)
SWCNT	Single-Walled Carbon Nanotubes
PMP	Poly (4-Methyl-1-Pentene)
BIC	Backup Ion Chamber
DIC	Diagnostic Ion Chamber
RS	Rang Shifter
WET	Water Equivalent Thickness
LaRC	Langley Research Center
LH_2	Liquid Hydrogen
LINAC	Linear Particle Accelerator
FEA	Field Emission Arrays
FTIR	Fourier Transform Infrared
SEM	Scanning Electron Microscopy
XRD	X-Ray Diffraction
XPS	X-Ray Photoelectron Spectroscopy
EDX	Energy-Dispersive X-Ray Spectroscopy
TGA	Thermogravimetric Analysis
DSC	Differential scanning calorimetry
GRRCC	Grand River Regional Cancer Centre
AE	Attenuation Efficiency
CSDA	Continuous Slowing Down Approximation

Chapter 1 Introduction

1.1 Motivations

Space is one of the most complex and extreme environments. It is filled with high-energy radiations and particles, moving at very high speeds that approach thousands of kilometers per hour. The high energy radiations in space are different from what we experience on earth, and human exposure to these radiations can cause severe health problems (either immediate or delayed). Besides, space radiation can cause the degradation of electronic devices and induce irreversible damages [1][2]. Therefore, protecting astronauts and hardware from hazardous ionizing radiations during space missions is vital.

To design suitable shielding material, it is necessary to have more information about the space radiation. Different types of radiation are mainly coming from three different sources: particles from trapped energetic radiation, solar particle events (SPE), and galactic cosmic rays (GCR). Each of the radiations has a specific requirement to be shielded. For example, high mass density materials are required to protect spacecraft from energetic electrons trapped in Van Allen radiation belts. High atomic number particles (HZE) are comprising a low quantity of the GCR radiations (about 1–2%), but they can interact with high specific ionization and contribute about 50% of the long-term space radiation dose in humans. Another type of hazardous radiation is secondary radiation, with less energy (compared to main radiations) but in high quantity and more damage on astronauts and spacecraft [3]. Secondary radiations (like electron particles) are produced from primary radiation interaction with the atoms of shielding materials. Although the interaction of radiations with matter depends on various parameters such as kinetic energy, they make 100% radiation attenuation unachievable due to the electromagnetic cascades [4]. The space shielding materials should limit the radiation dose to the lowest level so that long-time space missions can be implemented.

Modern spacecraft have been equipped with different radiation shielding materials among which aluminum (Al) is the most applied [5][6]. According to the special properties of Al, including high

strength and lightweight, Al and its alloys have been known as significant shielding components on spacecraft and satellites since the Apollo missions [7]. Al has been interpreted as a reference shielding material. Al structures with areal densities ranging between 2 – 20 g/cm^2 have been used on different parts of the International Space Station (ISS). However, the development of state-of-art materials with lower atomic numbers is highly demanding in future space applications.

Due to the shielding principles for space application, shielding materials can effectively protect spacecraft from space radiations if i) they have high electron density which leads to increasing the electromagnetic interaction between target electrons and the incident charged particles; ii) they produce less secondary radiations; iii) they are light in weight and can reduce the transportation cost [3][8]. According to these requirements, materials containing low atomic number (low-Z) elements have attracted expansive interest in the design of radiation shielding materials for space applications. For instance, a high hydrogen content material, including water and liquid hydrogen, has been investigated for space radiation shielding application. However, according to the feasibility and safety issues, they are not suitable to be widely applied on spacecraft [9][10].

In recent decades, researchers have studied the radiation shielding properties of various polymers [11]. Pure polymers are usually composed of low-Z elements (hydrogen in particular), which makes them suitable for space radiation shield application [1][12][13][14]. High-density polyethylene (HDPE) is one of the most suggested polymers for this application. However, HDPE can only be applied as an associate shielding layer with Al as it is suffering from poor thermal stability, low working temperature range, and extremely high thermal expansion. According to the harsh environment of space, polymers with sufficient thermal stability should be considered and investigated for this application, such as polydimethylsiloxane (PDMS).

In addition, many studies have shown the enhancement of thermal and mechanical properties of polymers by adopting the extraordinary advantages of nanomaterials. Owing to their unique chemical, physical and mechanical properties, especially very high surface area, nanomaterial has been known as effective fillers to improve the radiation resistance of polymer nanocomposites compared to pure polymer [15][16]. Low-Z materials such as boron nitride (BN) and carbon-based nanofillers are known as excellent candidates for this application because of their high thermal conductivity and mechanical strength. Studies have shown the potential of CNT nanocomposites

in proton and electron radiation shielding enhancement [17][18][19]. It was also found that multi-walled carbon nanotubes (MWCNT) can provide extra stability against radiations [20][21][22]. Additionally, based on the shielding theory, high atomic number (high-Z) materials (including bismuth) are good candidates for electron shielding because of their superb ability to absorb and shield photons and electrons [23][24][25]. However, the content of high-Z nanofiller should be increased in order to stop the electrons with very high energies. This will increase the chance of secondary radiation generation as well as sacrificing the nanocomposite weight advantages. On the one hand, high-Z fillers are required to efficiently shield the ionizing radiations. On the other hand, low-Z fillers would decrease the weight and the chance of secondary radiation generation. To overcome this problem, different fillers can be used in a multi-layered shielding structure [26].

A layer-by-layer assembly method can efficiently help to prepare nanocomposite with various atomic number nanofillers concentrated in different layers [27][28]. Homogeneously dispersing more than one filler in a polymer is always challenging, especially if various concentrations of different types of fillers with different shapes and sizes are embedded in a polymer matrix. Different type of nanomaterials with various concentration requires distinct dispersion methods, but it is difficult to use one method to mix them [29][30]. To overcome this problem, different fillers can be used in a multi-layered shielding structure [26]. Low-Z fillers (such as BN), medium-Z (such as titanium (Ti) and molybdenum (Mo)), and high-Z nanofillers (Bi_2O_3) can be homogeneously embedded in a polymer matrix and applied as different layers to enhance the shielding performance.

Therefore, investigations of high-energy radiation shielding properties of PDMS nanocomposites, as a low-cost commercially available polymer with excellent thermal stability, would potentially inspire broad research. Not only do polymer-based nanocomposites have immense potential to be applied for space radiation shielding, but also the multilayer nanocomposites which are filled with low-Z, medium-Z, and high-Z elements at the same time would be an appealing alternative to replace conventional material in various space applications, though they have attracted limited attention thus far.

1.2 Objectives

The purpose of this study (Fabrication and Evaluation of Structural Polymer Nanocomposites for Space Radiation Shielding Application) is to develop a polymer-based nanocomposite for space radiation shield application that can be used to compete with conventional material. To achieve this, the study is broken down into three secondary objectives, as described below:

- **Investigation of Appropriate Materials and Composition for Radiation Shielding Tests with X-ray Shielding Measurement**

The first objective was to develop the PDMS/Bi_2O_3 and PDMS/MWCNT nanocomposites with different weight percentages (wt.%) of nanofillers. The physical and mechanical properties of nanocomposites were characterized to find the optimized composition. Then the x-ray shielding properties of samples were evaluated using continuous x-ray with 60 to 90 keV energy. Additionally, multilayer nanocomposites in 2 to 5 layers were fabricated with alternately PDMS/Bi_2O_3 and PDMS/MWCNT layers and characterized for x-ray shielding with the same energies, to investigate the effect of layer structure on x-ray shielding efficiency.

- **Electron Radiation Shielding Test**

To study the effect of Bi_2O_3 and MWCNT on electron shielding efficiency of PDMS polymer, PDMS/Bi_2O_3, PDMS/MWCNT, and PDMS/MWCNT/Bi_2O_3 nanocomposites were fabricated. After characterizing the thermal and mechanical properties of nanocomposites, electron beams with energies of 9, 12, 16, and 20 MeV was used to simulate the extreme environment of space and irradiate the samples. The attenuation efficiency of all the samples was compared to that of the Al to evaluate the weight advantage of nanocomposites.

- **Optimization of Applied Nanofillers and Nanocomposite Structure**

A layer nanocomposite based on PDMS polymer was designed and fabricated with different nanofillers in different layers. Nanofillers with low-Z (BN) and medium-Z (Ti and Mo) were added to two different layers to minimize the Bi (as high-Z filler) content of PDMS/MWCNT/Bi_2O_3 nanocomposite. This approach helped to decrease the content of high-Z filler with least effect on the shielding efficiency.

1.3 Thesis Organization

This dissertation includes 7 chapters:

Chapter 1 is a brief introduction to the research background including the research motivation. Then provides the research objectives and thesis outline.

Chapter 2 provides a literature review about space radiations and their effects on humans and matter. Then there is an introduction to conventional and innovative radiation shielding materials.

Chapter 3 introduces the selected materials, fabrication methods, and shielding measurement tools used in this research.

Chapter 4 presents the fabrication and characterization of multilayer nanocomposite for x-ray shielding and provides a discussion on the effect of nanocomposite structure on shielding efficiency.

Chapter 5 exhibits the characterization of enhanced nanocomposite for high-energy electron beam shielding and follows by the electron shielding efficiency measurement.

Chapter 6 illustrates improved nanocomposite with a layered structure for electron radiation shielding, with minimum content of the high-Z filler, and enhanced shielding performance.

Chapter 7 includes a conclusion, the major contributions, and the future work.

Chapter 2 Background

The space environment with hazardous radiations is extremely dangerous for astronauts. For those space missions which are around the Earth, the magnetic field of the Earth is providing the major shielding against the space radiation exposures. However, for the space missions beyond the low earth orbit (LEO) like missions to Mars or other planets, the risks of exposure to hazardous space radiation become more severe [31].

Many experimental and theoretical investigations have introduced a variety of materials, such as heavy metals, for shielding the space radiations. However, due to the limitations of the metallic shielding materials, including secondary radiations generation, difficulties of manufacturing, high cost, and high weight, it has been a pressing matter to develop innovative highly efficient lightweight materials for shielding application.

2.1 Space Environment

The space environment is an extremely dynamic place, which is full of high energy particles and hazardous radiations. The source of the radiation is different from what we experience on earth (gamma rays for example), but they are particles from three different main sources: trapped energetic radiation, Solar Particle Events (SPE), and Galactic Cosmic Rays (GCR) (as shown in Figure 2-1). These radiations are one of the most important concerns in space missions because of their dangers to the astronauts' health and the electronics on board [3][31].

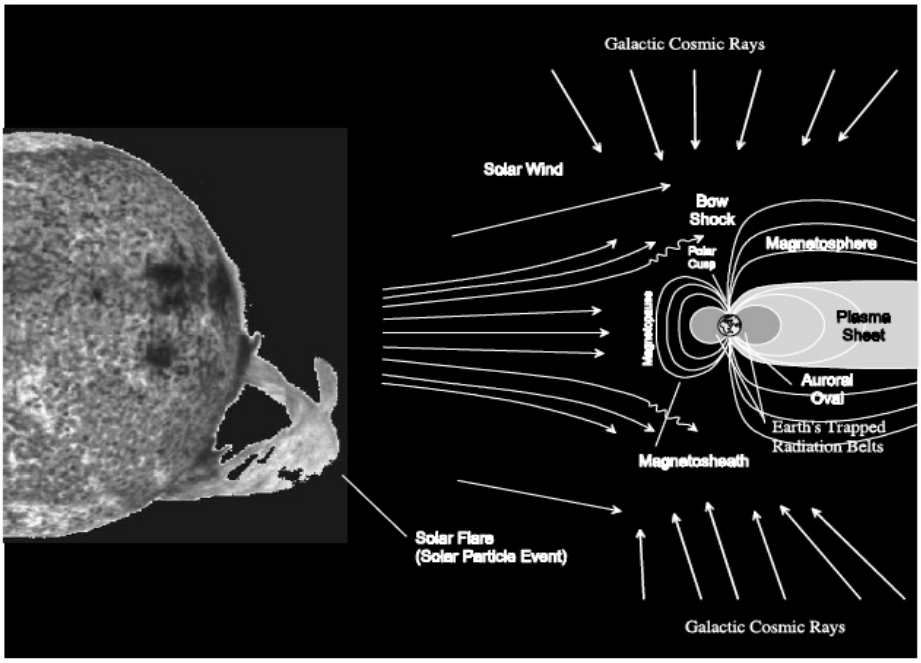

Figure 2-1. Space radiations [3]

2.1.1 Source of the space radiations

i) Galactic Cosmic Rays (GCR)

Coming from out of the solar system, the GCR is ionized atomic nuclei and subatomic particles (electrons and positrons) radiated by energetic objects like stars and supernovae. The contribution of electrons and positrons in GCR is small (∼2%), which can be easily stopped by even most light shielding parts (<5g/cm^2 Aluminum) on spacecraft. The other 98% are baryons particles (85% protons, 14% α particles, and ∼1% high atomic number high energy particles (HZEs)). Although HZE ions comprise a small number of GCR particles, these high atomic number ions (Z>10) with a very high energy (E>100GeV) supply a significant amount of GCR dose and are seriously harmful to astronauts. However, spacecraft materials can barely shield them [4].

The magnetic field of Earth in low Earth orbit and the solar activities in solar system can considerably affect flux of GCR particles. The energy of GCR particles in solar minimum and maximum (changing between 10 MeV to 10 GeV/nucleon) is shown in Figure 2-2. Near the Earth poles, high energy particles move toward the earth. Consequently, the flow of GCR particles exposed to the spacecraft in LEO increases and reaches a maximum. However, near the Earth

equator, the high energy particles move in parallel with the Earth, result in flux reaches a minimum in this area [31][32][33].

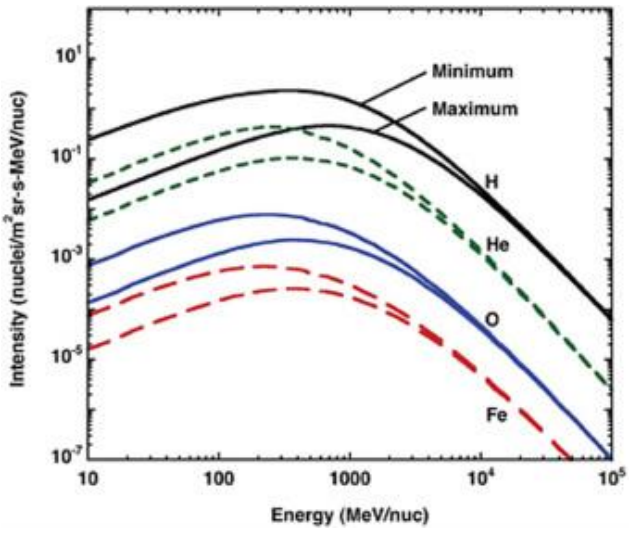

Figure 2-2. GCR particles energy in solar minimum and maximum [34]

ii) Solar Particle Event (SPE)

SPEs are accelerated particles (mainly proton), emitted by the Sun. There are three types of SPEs: solar wind, solar flare, and coronal mass ejections (CME). During the solar winds, particles including protons and of electrons projects outward from the Sun, with speed varying between 750 km/s and 400 km/s, and energy changing between 1.5 keV and 10 keV. Structural materials in spacecraft can easily shield the low energy particles from solar winds [35][36].

Solar flare is a sudden outburst of electromagnetic radiation from the Sun that arises in active solar regions around sunspots and can cause bursts of energy ($<6x10^{25}$ J). The duration of flare events is from minutes to hours. It can be characterized by large flows of electrons ($10^7/cm^2$ to $10^8/cm^2$), with an angle from 30° to 45° in solar longitude.

CME is the event of a significant burst of matter from the sun, which includes protons, electrons, and plasma. Along with the electromagnetic radiation, a small amount of HZE particles (Z<26) are also ejected from the sun, during the CME event. The CME is characterized by large fluxes of protons ($10^9/cm^2$) with an angle of 60° to 180° in solar longitude, and its duration is in the order

of days. The speed of particles changes between and 20 km/s to 3,200 km/s, with an average of 489 km/s [37][38][39].

iii) Trapped Energetic Radiation

Electrons and protons from SPE and GCR can interact with the magnetic field and atmosphere of the Earth. The interacted particles will then be trapped by the magnetic field and form the Van Allen radiation belt (Figure 2-3). Van Allen radiation belt consists of two belts: inner and outer. The inner belt is 100-10,000 km above the surface of the Earth and includes mainly protons and electrons with energies up to 5 MeV. The outer belt is 13,000-60,000 km above the ground and includes mainly electrons with energies less than 7 MeV. The energy of the trapped protons in inner belt increases as a function of altitude and goes up to hundreds of MeV with a broad peak between 150 MeV and 250 MeV [9][31][40].

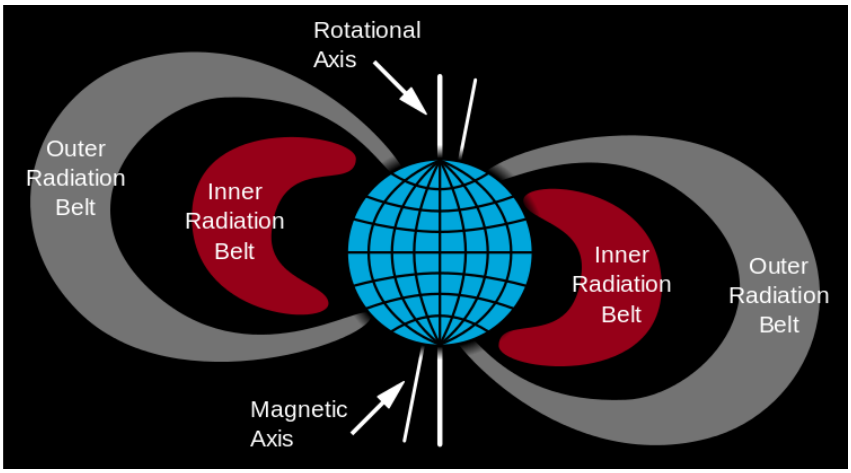

Figure 2-3. Van Allen Radiation Belt [14]

2.1.2 Effects of Humans Exposure to Space Radiation

Astronauts' exposure to ionizing space radiation and high energy particles results in health hazards. The effects of these exposures are related to various parameters, including particle energy level, radiation type, exposure time, and the absorbed dose. Many investigations have reported the danger of exposure to SPE and GCR space radiations. Some health risks, which are induced by space radiations, are cataracts, carcinogenesis, neural system damages, and cardiac problems [33][1].

Space radiations with high energy particles can induce damage effects on biological tissue, which results in immediate or delayed health issues. The human body's cell interaction with these particles may lead to cell death or irreparable genetic damages such as DNA mutations [41]. Furthermore, short exposure time or exposure to low energy particles may result in the damage on chromosomes and induce delayed effects like carcinogenesis and organ degradation [42].

Moreover, according to the threats from the space radiation environment, applied radiation shielding material should perform radiation-dose and the mass attenuation rates of more than 50%. The collected data of space missions demonstrated that the detected radiation dose by spacecraft could vary between 10.3 mGy/day and 1,154 mGy/day in Geostationary orbit (GEO) and 110-1,270 mGy/day in LEO [3]. Although various advanced materials have been used in space stations and spacesuits, astronauts can still be exposed to different radiations with energy changing from 80 mSv to 160 mSv/six-months, which is high in comparison with that of the Earth (2 mSv/year). However, radiation dose limits vary by gender and age of astronauts. Due to the National Council on Radiation Protection and Measurement (NCRP) report, the radiation dose limits in LEO is from 0.4 Sv to 1.7 Sv for female and 0.7 Sv to 3.0 Sv for male (as shown in Table 2-1) [43][44].

Table 2-1.Whole Body adequate dose limits for male and female at different ages [45]

Age	25 yrs	35 yrs	45 yrs	55 yrs
Male – limits (cSv)	70	100	150	190
Female – limits (cSv)	40	60	90	160

2.1.3 Radiation Effects on Electronic Devices

Induced radiation damage effects on electronics are mainly single event effects (SEE), displacement damage, and total ionization dose (TID) effects.

(i) Total ionization dose effects

Electronic devices consist of semiconductor and dielectric materials. Along the path of a radiation particle, electron-hole pairs that are created in dielectric materials result in the generation of

vacancies or trapped charges in regions near the interface between the semiconductor and dielectric layers.

(ii) Displacement damage

Atoms in the crystal lattice may be displaced by high energy particles (neutrons, protons, electrons, alpha particles, heavy ions, secondary electrons), resulting in changes in the material properties (Figure 2-4) [46].

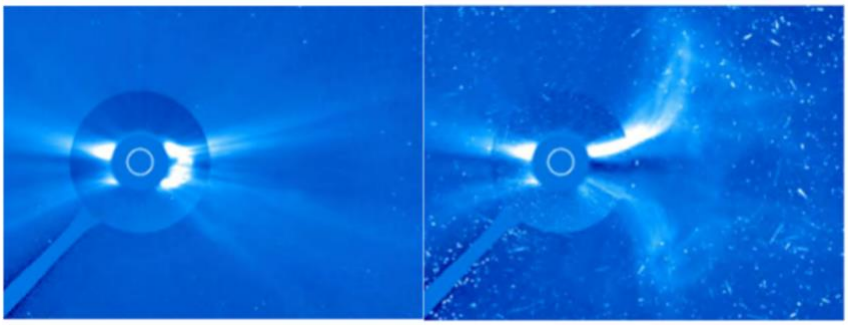

Figure 2-4. charge-coupled device photography of an electronic piece before and after displacement damage [46].

(iii) Single event effects

Ionizing particles (high-energy protons and HZE particles) can deposit energy to materials and cause permanent failure or soft errors. SEEs include single-event burnout (SEB), single-event latch-up (SEL), and single-event upset (SEU). SEB is a destructive state and can be a highly localized burnout of the drain-source in power MOSFET, and SEL is a potentially disastrous state leading to current exceeding on circuits. In addition, the SEU is an ionization particle-induced alter of condition (Figure 2-5) [47][48].

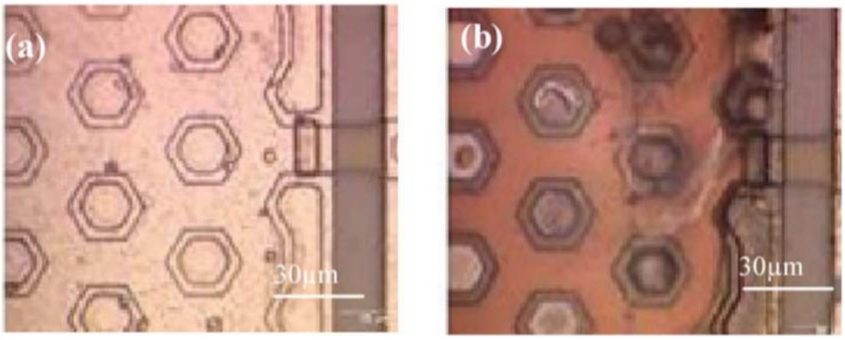

Figure 2-5. Photographs of a transistor before (a), and after (b) burning by the SEE [48].

2.1.4 Radiation Interaction with Target Material

When primary radiation particles of the trapped radiation belt, GCR, and the SPE pass through the shielding materials, nuclear interactions occur and result in secondary radiation particle generation with energy changing between 0.001 GeV and 5 GeV.

Nuclear interactions are mainly categorized into two types: projectile and target fragmentation. Different factors may affect this interaction, including the collision angle, the charge, and the kinetic energy. Neutral prions and γ-rays produced during the nuclear reactions can lead to electromagnetic cascades.

HZE high energy particles interact with the target material and lead to the projectile fragmentation. This interaction results in high-energy secondary electron and neutrons generation. The high energy secondary particles interact with materials and continue the nuclear reactions. The target fragmentation is the result of interaction between trapped GCR particles and heavy atom nucleus or carbon and oxygen nuclei in the human body [3][49].

In summary, during space travels, high-energy radiation can affect astronauts and result in serious health problems. Besides, the space radiation has damage effects on electronic components and structural materials in the spacecraft. Therefore, well-designed radiation shielding materials are critical in space exploration missions [3][41][50][51].

2.2 Radiation Shielding Principles

In order to shield HZE particles and protons effectively, shielding components should have high electron density. In addition, an efficient shielding structure should minimize the shielding atoms' fragmentation and maximize the probability of projectile fragmentation.

2.2.1 Shielding Protons and HZE Ions

HZE particles and high energy protons with positive electric charges are thousands of times greater than electrons in mass. Besides, the volume of nucleus is only about 10% of the atom's volume. As a result, when HZE particles and protons are passing through the shielding materials, they rarely interact with a nucleus, and their energy is lost mostly by interaction with electrons and exciting or ionizing atoms. Therefore, it is essential to design or find new structures and materials with high electron density to shield hazardous radiations of HZE particles and protons. Equation 1 is a model to calculate the electron density (number of electrons per unit volume) [52].

Equation 2-1

$$\text{Electron density} = \mathrm{N}\left(\frac{\mathrm{Z}}{\mathrm{A}}\right)$$

Z: the material atomic number, A: Z + number of neutrons, N: the Avogadro's number=$6.022\mathrm{X}10^{23}$.

Due to the equation, the electron density is related to two parameters: the ratio of Z/A and the material density. Space shielding materials should have low density and be lightweight. Therefore, to design suitable radiation shielding materials, the Z/A ratio should be considered as a critical factor. Materials with higher Z/A ratio are more efficient for shielding applications. Figure 2-6 shows the Z/A ratio corresponding to atoms with the atomic number from Z = 1 to Z = 90. According to Figure 2-6, the hydrogen atom has the highest Z/A ratio (more than 50% in comparison with the other atoms).

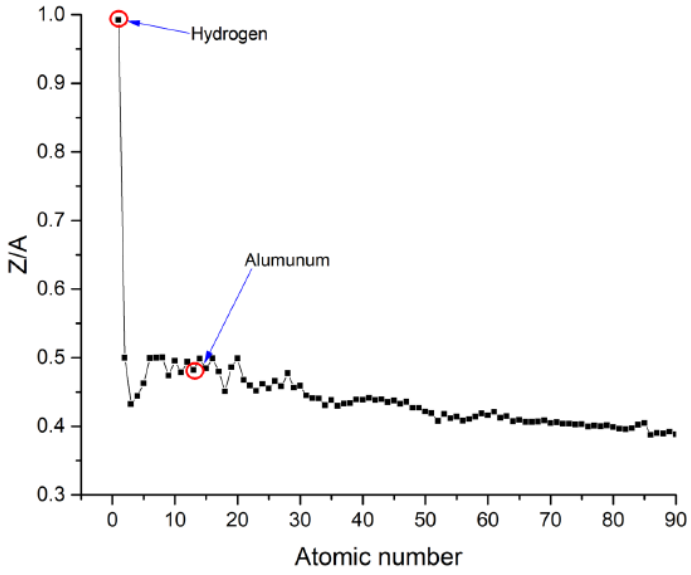

Figure 2-6. Z/A ratio for different atoms (1<Z< 90)

Minimum target atoms fragmentation and maximum probability of projectile fragmentation are other factors that should be considered in radiation shielding materials. HZE particles and protons lose most of their energy when interact with electrons, but nuclear reactions can happen when incident particles have high kinetic energies. It should be mentioned that energy transfer of the high energy particles radiation is directly proportional to the atomic number of particles. Therefore, when incident HZE particles fragment into ions with smaller atomic number, the kinetic energy is almost the same as the primary HZE particles, but the total dose equivalent is decreased [53].

2.2.2 Shielding electrons

When electron radiations passing through a material, Coulomb interaction happens between electron particles and atoms of shielding material. However, since electron particles have the same mass as the electron in matter, the collusion results in billiard-ball collisions that can produce much more scattering. For electrons with more than 10 keV energies, larger energy-loss happens during each collision. Therefore, much longer range and lower ionization density electron has in shielding materials compared to positive ions [54].

However, for electrons with lower energy, Coulomb interaction with positively charged nucleus bends the electrons and results in bremsstrahlung x-ray radiation generation. The energy of this

secondary photon depends on scattering angle, atomic number Z, and the energy of incident electrons. In addition, electron energy loss because of the bremsstrahlung radiation highly depends on Z, as equation shows:

Equation 2-2

$$\frac{Z_{radioactive}}{Z_{electronic}} \approx \frac{ZE}{800\ MeV}$$

As can be indicated from the equation, high-Z materials (Z = 80-90) can produce larger number of photons in comparison with low-Z materials, since low-Z materials stop high energy electrons (10-100 MeV) by ionization. Therefore, since more energy can deposit into high-Z materials, they can attenuate greater electron energy. However, low-Z materials create fewer secondary radiations (mostly Auger electrons and Bremsstrahlung radiation) by less electron attenuation [3]. As a result, the advantages of both high- (i.e. high stopping power) and low-Z (i.e. less secondary radiations) materials should be adapting into shielding product to efficiently shield electron radiations [19][55][56].

2.2.2 Shielding secondary radiations

As discussed in previous sections, there are two types of secondary radiations. One from electron radiation interaction with matters (secondary electrons and photons), and the other is that of proton interacting (secondary neutrons). Secondary electron and photon shielding are achievable as described above. But typical strategy for neutron shielding includes two steps. First, the fast neutrons should be slow down and convert to thermal energies. Applying lightweight elements in the shielding structure can be helpful in this regard. Hydrogen is useful as shielding material since the neutron's radiation energy can transfer to hydrogen nucleon during the collision. The equation below can be applied to explain the relation between transferred energy to a nucleus and neutron energy.

Equation 2-3

$$Q = \frac{smME_n}{(M+m)^2}$$

Q: transferred energy, m: the mass of received energy nucleus, E_n: neutron energy, and M: neutron atomic mass M.

For a single neutron, the atomic mass is always 1 (M = 1). According to the equation, hydrogen is the best material for neutron shielding since the mass of hydrogen atom is 1 (m=1), which means the incident neutron can transfer the maximum amount of energy to a hydrogen atom. Therefore, when the atomic mass increases, the transferred energy decreases. Polyethylene, water, concrete, and paraffin are the most used fast neutron moderating materials. However, each has its disadvantages: water needs to be frequently maintained, and evaporation of water may cause a reduction of shielding effectiveness. Paraffin is flammable, which induces further safety problems. Although concrete has been applied widely in nuclear stations and accelerator facilities, the weight problem makes it impossible for use in space applications [8].

The next step is to shield the thermal neutrons, which can be achieved by materials with high thermal cross-sections for neutron captures. Table 2-2 shows the stable isotopes of a variety of materials with approximately large thermal cross-sections. Boron, helium, and lithium isotopes (^{10}B, ^{3}He, and ^{6}Li, respectively) shield the thermal neutrons without γ-rays emission. Besides, isotopes with γ-ray production need more photon shielding [8]. More information regarding shielding the neutron particles can be find in the review paper that I have published [17].

Table 2-2. thermal cross-section of different stable isotopes

Z	Target isotope	Reaction product	Energy released (MeV)	Thermal Cross Section (Barn)
64	^{157}Gd	^{158}Gd + (g or ce)	7.937	254,000
64	^{155}Gd	^{156}Gd + (g or ce)	8.536	60,900
62	^{149}Sm	^{150}Sm + (g or ce)	7.985	40,140
48	^{113}Cd	^{114}Cd + (g or ce)	9.041	20,600
63	^{151}Eu	^{152}Eu + (g or ce)	6.305	9,200
2	^{3}He	p + t	0.7637	5,333
5	^{10}B	^{7}Li + a	2.79	3,838
71	^{176}Lu	^{177}Lu + (g or ce)	7.073	2,090
77	^{191}Ir	^{192}Ir + (g or ce)	6.199	954
3	^{6}Li	a + t	4.784	941
68	^{167}Er	^{168}Er + (g or ce)	7.771	659
72	^{177}Hf	^{178}Hf + (g or ce)	7.626	373
62	^{152}Sm	^{153}Sm + (g or ce)	5.868	206
45	^{103}Rh	^{104}Rh + (g or ce)	7.000	145

2.3 Conventional Materials for Radiation Shielding

In order to protect astronauts and the spacecraft electronics from hazardous radiations during the space missions, some materials have been developed. These materials mainly include aluminum and its alloys.

Al and its alloys are known as the standard materials for space radiation shielding applications for more than 50 years. According to the weight advantage of Al in comparison with other heavy metals, it is cost-effective in space applications. It also can endure the stresses that occur during space travel.

There are three types of Al alloys in aircraft bulk materials: the 2000 series (Al-Cu-Mg), the 6000 series (Al-Si-Mg), and the 7000 series alloys (Al-Zn-Mg-Cu). However, new engineered materials are appearing that can replace conventional metallurgy products. They are the aluminum-based

metal matrix composites (MMC), the low-density aluminum-lithium alloys, metal-polymer hybrid composites, and the powder metallurgy processed 7000 series alloys. Figure 2-7 and Figure 2-8 illustrate the incremental enhancements in yield strength and specific stiffness of aluminum alloys, respectively [57].

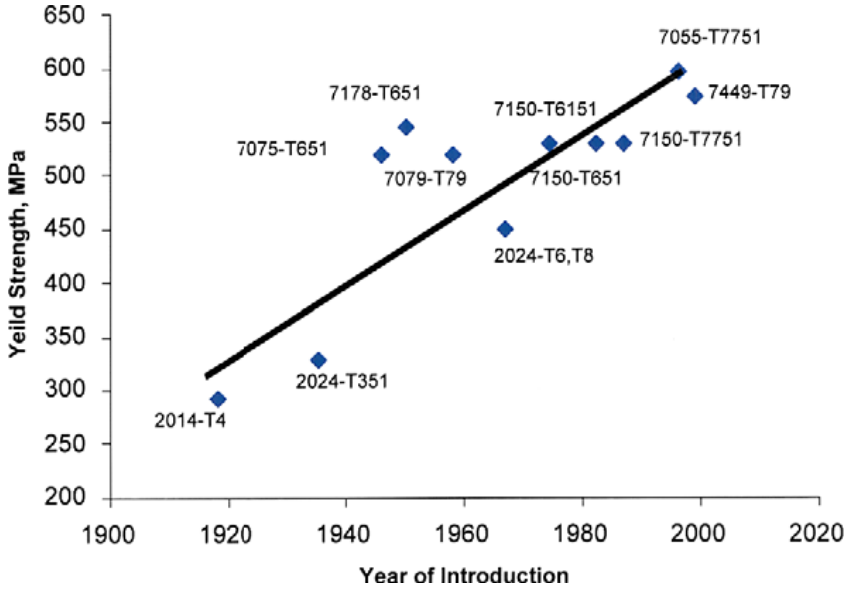

Figure 2-7. Yield strength of aluminum alloys is plotted based on the year of first-time application.

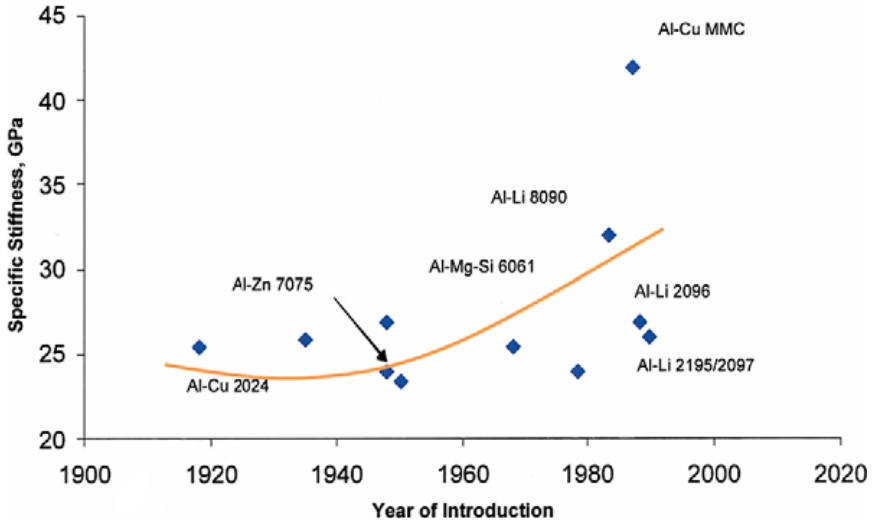

Figure 2-8. The modulus of aluminum alloy is density normalized and plotted as a function of the first-time application.

Regarding radiation shielding, shielding effectiveness of Al has been investigated for years [6]. The desired amount of radiation-dose attenuation rate in space missions, is more than 50%. Typically, Al with areal density of 2-5 g/cm^2 is used as radiation shielding walls of spacecraft. This number increases to about 20 g/cm^2 to fully stop 100 - 200 MeV proton radiation and protect payloads in several parts of ISS (Figure **2-9**). Studies also recommend 20 g/cm^2 Al as the effective shielding for Earth to Mars space missions [3][4][5].

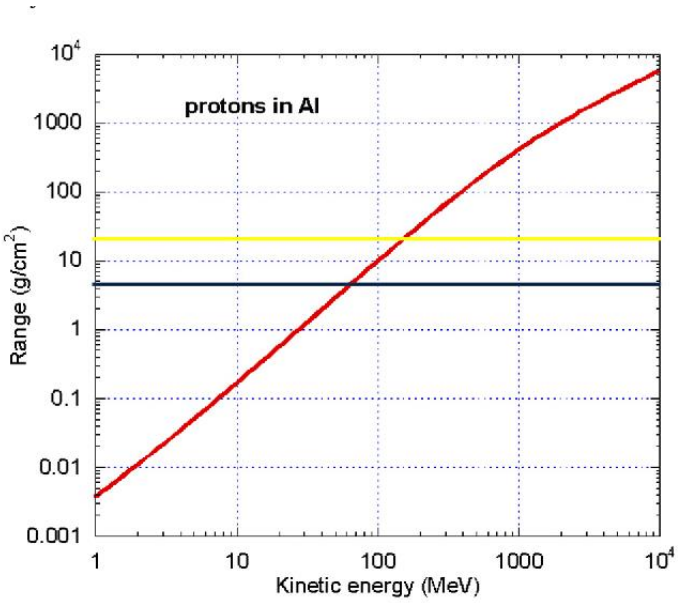

Figure 2-9. Energy-range relationship for protons in aluminum. Horizontal lines show thickness of the Al walls of spacecraft (5 g/cm^2, black line) and the effective thickness (20 g/cm^2, yellow line)

However, Al produces more secondary radiations during the interaction with protons in comparison with low-Z materials, such as polymers. Massively generated secondary particles, including neutrons, electrons, and photons will lead to extra damages to the astronauts and electronics. Furthermore, Al is high in weight, which can reduce the space travels duration and increase the cost because of the further fuel consumption.

2.4 Alternative Shielding Materials and Requirements

It has now become a priority to develop alternative radiation shielding materials to replace Al for radiation shielding application. These materials must have sufficient shielding efficiency and sometimes an improved protection against space radiations exposure. The important properties and requirements for the new shielding materials are listed and discussed in this section.

2.4.1 Thermal Property

One of the most important space environment effects on the spacecraft parts and devices is the incoming energy from sun since the exposure to sun in space is about 25% stronger than that on the ground. Also, the irradiated heat from the electronic devices such as photovoltaic cells, thermal control systems, batteries, radioisotope thermoelectric generator, science instruments are another effective heat sources [84].

In addition to heat sources, the heat dissipation in space is different in comparison with the surface of the earth, because of the oceans and atmosphere which act like heat sinks. On earth, day-night temperature variation is about $T_{mean} = \pm 10$ ℃ with an annual mean of $T_{annual\ mean} = 15$ ℃. These values changes to ±100 ℃ and 1 ℃, respectively, on an artificial satellite or generally the objects exposed to harsh environment of space [85].

Although, polymeric materials are highly recommended to be used in space such that the high-Z materials can be replaced, but extremely low heat conducting capacity of polymers limits their application. Photons, electrons, and phonons can transport energy in solid polymers. However, electrons cannot freely move in these materials. Thus, phonons are responsible for heat dissipation in polymers. Moreover, the thermal conductivity of the polymers can be affected by the environmental temperature and the crystallinity. For example, the conductivity of amorphous polymers would reduce smoothly when the temperature goes down from 100 K; however, the conductivity of polyethylene, which is a semicrystalline polymer, would decrease extremely below 100 K [58].

Therefore, it is essential to improve the thermal conductivity of polymers to keep materials temperature in the working temperature range.

2.4.2 Lifetime

In addition to attenuating projected radiation particles, an effective radiation shielding material should have high resistivity against radiation damage effects. A material that degrades quickly is not a promising shielding material for space missions. However, when polymers are irradiated by different radiations, can display damage effect including micro-cracking, crosslinking and session of the polymer chain, mass loss, etc. These effects can result in changes in physical and mechanical properties of composite's and alter the performance of materials from their original design.

2.4.3 Light Weight

High weight is another important concern that limits the use of High-Z materials. High weight of Al and its alloys increase the mission cost and decrease the mission lasting time because of the further fuel consumption [27][57]. Using materials with low areal density is one of the solutions to reduce the fuel costs.

2.4.4 Low Cost

The heavy weight and short lifetime of materials and components of spacecrafts can increase the mission cost because of further fuel consumption and the maintenance missions. To reduce the space mission cost, as mentioned previously, applying lightweight materials with long lifetime is necessary. Therefore, low atomic number (low-Z) components are highly recommended to be used in the space shielding structure [42].

2.4.5 Material Compatibility

Hydrogen is considered as the most effective material for space shielding application. However, applying pure hydrogen is limited due to the challenges of its transportation, storage, and safety concerns. During the recent decades, various hydrogen containing materials, such as BeH_2 and LiH have been investigated for designing high hydrogen content radiation shielding materials. However, some compounds such as BeH_2 has uncertainties in reactivity and toxicity. In addition, the safety issues, related to LiH, limit its application in shielding structure [9].

2.5 New Technologies

Due to the radiation shielding requirements discussed in previous section, suitable materials for space shielding application should has primary characteristics including suitable thermal properties to dissipate the heat, high electron density in order to enhance interactions between the incident charged particles and target electrons, light weight to reduce the cost, and fewer secondary particles generation. Therefore, lo-Z materials ($Z \leq 6$) have been considered to design a new generation of radiation shielding materials.

2.5.1 Low-Z Materials

(i) Hydrogen-Rich Materials

According to the previous sections, hydrogen is known as the most effective element for shielding application, since the hydrogen atom, with no neutron in its nucleus, has the highest Z/A ratio (Z/A=1). However, the difficulties of transportation, storage, and related safety issues limited the application of water and pure hydrogen. Therefore, researchers have considered hydrogen content materials.

Various hydrogen-containing materials have been investigated for designing high hydrogen content radiation shielding materials such as metallic hydrides, including BeH_2, MgH_2, $LiBH_4$, $NaBH_4$, and LiH. Table 2-3 shows the density of metallic hybrids and their hydrogen content as a weight percentage. As a result, LiH and $LiBH_4$ are mainly considered as potential materials to be studied. However, safety issues limit the viability of LiH. Also, some compounds such as BeH_2 has uncertainties in toxicity and reactivity [9][59].

Table 2-3. Hydrogen content and the density of metallic hydrides.

Material	**ZrH_2**	**LiH**	**$NaBH_4$**	**$LiBH_4$**	**BeH_2**	**TiH_2**	**MgH_2**
Density (g/cm^3)	5.56	0.78	1.07	0.66	0.65	3.75	1.45
H Wt.%	2.16	12.7	10.7	18.4	18.3	4.04	7.7

(ii) Hydrogen-Rich Polymers

According to the literature, pure polymers are considered as suitable materials for space radiation shielding application, since they usually construct from low-Z elements such as hydrogen and carbon. In comparison with metallic materials, polymers are lighter in weight, which is one of the advantages of these materials for space shielding applications. Various polymers are applied in space, including polyetherimide (PEI) and polyethylene (PE) [42][60].

Furthermore, PE $(CH_2)n$ has been deeply and widely investigated for radiation shielding application because of its high hydrogen content (14 wt.%) [61][62]. It is one of the materials that NASA has chosen to apply in space. However, pure PE cannot provide all the requirements for space application, and it is usually replaced by high-density polyethylene (HDPE) and ultrahigh molecular weight high-density polyethylene (UHMW-HDPE).

Zeitlin et al. (2006) reported the radiation shielding properties of different materials under HZE particle radiation [63]. Samples of hydrogen, PE, and PMMA with different densities and thickness were tested, and the δD was normalized to make the comparison between different samples.

Equation 2-4

$$\delta D_n = \delta D / sample\ thickness$$

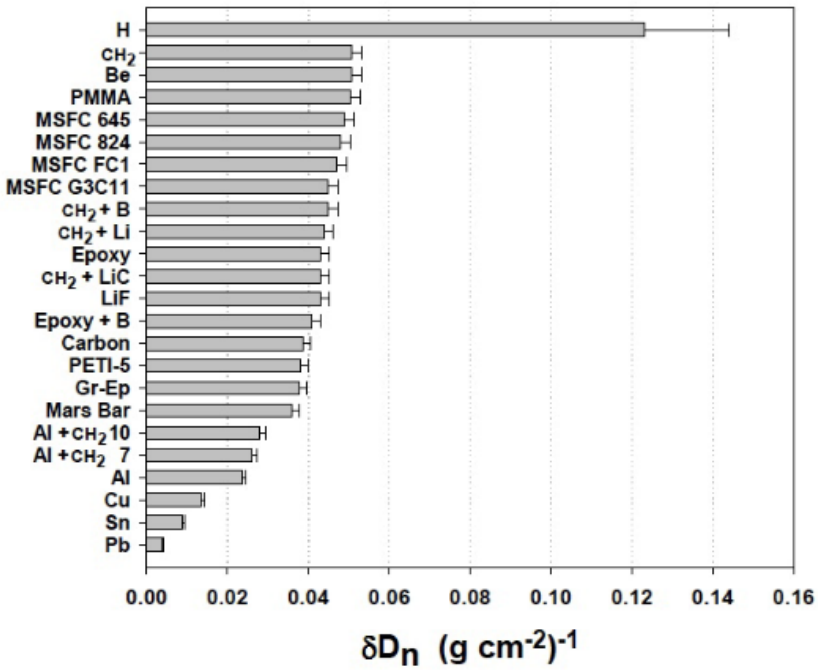

Figure 2-10. δDn of materials [63]

Figure 2-10 shows the results of the test. Samples with higher δDn (the normalized dose reduction) value would have better shielding effectiveness. The best shielding material is pure hydrogen. PE and low-Z materials like PMMA and Be are the other effective shielding materials in comparison with other composites.

However, compared to metallic materials, pure polymers have low thermal conductivity and week mechanical properties. These properties can be determined by monomer chains and crystallinity in polymers. Polymers with a higher degree of crystallinity can have more thermal stability. In addition, polymers containing covalent bonds are not strong enough in comparison with the metals [64][65].

Furthermore, the free-radical formation, which induces by high energy radiations, is the main reason for material properties degradation. Generally, the polymer backbone absorbs the ionized energy upon photon/particle radiation, and undergoes crosslinking and chain scission, as a result of free radical formation. Consequently, the properties of the polymer considerably changes [42].

2.5.2 Nanocomposites

Polymer composites reinforced by nanofillers are suggested to improve the properties of polymers including mechanical strength, thermal properties, and radiation shielding efficiency.

Upon irradiation, a free radical process can be initiated in the polymer backbone by the adsorbed ionizing energy. Consequently, the polymer undergoes crosslinking (results in increasing tensile strength but reducing elongation) and chain scission (reduction of elongation and tensile strength). Generally, the improvement in properties of the nanocomposite depends on a variety of factors, including the filler material properties, homogenous dispersion of the fillers in the polymer matrix, and interfacial interaction between the polymer and filler [66][67]. For example, polymer reinforcement with radiation-resistance nanomaterials has been shown to enhance the radiation efficiency of the nanocomposite [27][56].

Carbon-based nanomaterials are usually applied to reinforce polymers and improve the mechanical properties of composites because of their high strength-to-weight ratio [68][69]. Carbon nanotube (CNT) is a carbon nanomaterial that can enhance the properties of polymer nanocomposites according to its unique features such as considerably high tensile strength and elastic-modulus, excellent electrical and thermal conductivity, and high oxidation resistance [12]. Therefore, carbon composites are suitable materials in applications requiring lightweight and mechanical strength.

Although several groups have investigated the mechanical and thermal properties of polymer/CNT composites [70][71][72], only a few groups have studied the radiation shielding properties of carbon-based polymer composites [73][74]. For example, previously in our group, SWCNTs-based polymer composite was irradiated by a high-energy proton beam to investigate the stopping properties. The addition of SWCNT improved the shielding performance of composite in comparison with Al. In addition, composite containing SWCNT exhibited less secondary neutron generation compared to pure polymer and Al [18].

As discussed previously, secondary radiations (light ions, electrons, neutrons, and gamma rays) generated by the interaction between shielding materials and GCR are harmful to payloads. To stop electrons and absorb gamma rays, nanofillers with high bandgap and stopping power are required. Usually, high-Z Pb (stopping power 2.41 MeV cm^2/g) is applied to shield high energy x-

ray and gamma rays [56]. However, according to the toxicity of Pb, in recent years many studies have been conducted to develop lead-free shielding materials. In this regard, nanofillers with similar shielding properties as Pb have been embedded into the polymer matrix and compared with Pb [75][76]. Bismuth Oxide (Bi_2O_3) is one of the potential candidates to replace Pb and Al according to the high bandgap of 2.3-3.3 eV and higher total stopping power (Bi: 2.433 and Pb: 2.407 MeV cm^2/g at an electron energy of 10 MeV) [77][78].

In recent years, a new generation of carbon-base nanomaterials has been developed and considered for various application except the ionizing radiation shielding. Two-dimensional (2D) MXenes have attracted researchers' attention due to their unique properties such as thermal stability. Different types of MXenes can include various transition metal elements, such as Ti and Mo [79][79][80].

In addition, most of the polymers have low mechanical strength and thermal conductivity, both of which are required to be enhanced for radiation shielding applications. Several studies have focused on using fillers to improve the properties of polymers. As noted previously, the properties of polymer composites greatly depend on the filler materials and their physical and mechanical properties. Therefore, the carbon-based nanomaterials can improve the thermal and mechanical properties of polymers, because of the extremely high thermal conductivity and mechanical strength of the nanotubes and graphene [81][72]. In addition, boron nitride (BN) with high thermal conductivity can be applied as a nanofiller to enhance the thermal conductivity of polymer matrix [82][83].

2.5.2 Multilayer Structure

Applicable light-weight structures for space missions have been investigated by various research groups [84]. As mentioned in previous sections, lightweight materials such as pure polymers cannot efficiently attenuate the high energy radiations. In addition, heavy materials are highly potential to create secondary particles [85]. One of the current trends in modern space missions is applying multilayer design as shielding for extreme and complex hazardous space radiations that are difficult to shield by a single material. Each part of a multilayer structure associates with the other components in the structure, whilst accomplishing specific functions. This approach results

in a multifunctional structure with excellent thermal and mechanical properties, and great shielding efficiency.

In a research, A. Emmanuel et al. (2015) designed and fabricated a structural polyethylene composite reinforced with graphite fiber. They explained and showed the influence of the multilayer composite on shielding efficiency for space radiation shielding application [86]. X. Li's et al. (2018) has reported that polyethylene associated with Al can accomplish 6% weight reduction compared to pure Al when shielding GCR [53]. Also, based on research from NASA, hydrogen (5wt%) crafted boron nitride nanotube itself has about 33% weight reduction over Al under simulated GCR environment [87]. However, the unstable hydrogen in nanotubes as well as the affected mechanical strength of nanostructures will limit its applications [88]. Other elements such as carbon have been investigated when exposed to GCR [89]. However, it is still a major challenge to replace the conventional Al shielding structures.

Multilayer polymer nanocomposites are suggested as high potential alternative materials for the structural radiation shielding application since various nanofillers with different concentrations can be embedded in each layer. Generally, homogeneously dispersing more than one filler in polymer mixtures is challenging, especially if various concentrations of different types of fillers with different shapes and sizes are embedded in a polymer matrix. Different type of nanomaterials with various concentration requires distinct dispersion method, but difficult to use one method to mix them [29][30]. To overcome this problem, different fillers can be used in a multi-layered shielding structure [26]. Kaul et al. (2010) constructed PE nanocomposite in three layers according to its lightweight and shielding effectiveness of 50% higher than Al [90]. The first layer is designed to protect spacecraft from meteoroid collisions, and it includes ceramic materials such as SiC, Al_2O_3, and B_4C. The application of this layer is to protect spacecraft. The next layer is made of a PE polymer composite with ultra-high molecular weight PE fibers as the filler, to shield the space radiation and meteoroid collision. The last layer is a nanocomposite of epoxy resin reinforced with interwoven PE fibers, which is the main layer for radiation shielding. These three layers together form a multifunctional-layered nanocomposite. It also is an excellent impact-resistance material when filled with boron nitride particles reported by Harrison [91]. The composite shows low energy neutron absorption ability with improved mechanical properties over neat PE. The weight percentage of boron nitride particles is about 0.1 - 1.5 wt.%.

The literature analysis shows that there is still a lack of information regarding the multilayer polymer nanocomposite fabrication and characterization for space radiation shielding application. Various materials and fabrication methods need to be considered and studied for this purpose to develop a corresponding shielding material with good physical and mechanical properties, to replace Al.

Chapter 3 Materials and Methods

In this chapter, the applied materials and methods for composites fabrication are introduced and illustrated. The background information of these materials and tools is useful to understanding the conducted experiments and collected results in the following chapters.

3.1 Materials

As discussed above, considering GCR and SPE space radiations, multifunctional shielding structures with less- or non-metallic materials must be developed. The applied materials to develop such a structure in this research are listed below, including PDMS as polymer matrix and various nanomaterials such as hexagonal boron nitride (h-BN), Carbon-based nanomaterials (MWCNT), 2D MXenes, and bismuth oxide (Bi_2O_3).

3.1.1 Polydimethylsiloxane (PDMS)

Polydimethylsiloxane (PDMS) is a low cost commercially available polymer with excellent thermal stability, which means upon increasing the temperature it does not show significant changes in viscosity. The working temperature range of PDMS is −40°C to 200°C with a glass temperature below -40 °C. PDMS also possess good flexibility, as well as good oxidation resistance and biocompatibility. The high flexibility of PDMS allows it to be bent, stretched, and compressed repeatedly, which makes it potential material for wearing and coating applications. It has high bonding energy (445 kJ/mol) with presence of methyl CH_3 groups in its structure which makes it chemically stable material.

Since these properties, especially the thermal stability and working temperature range, are important concerns for shielding materials and the applied materials on spacecraft, PDMS had become our prioritized candidate to develop a new radiation shielding material.

Table 3-1 includes a list of properties of PDMS and HDPE (as the reference polymer for shielding application) for more comparison [92][93].

Table 3-1. a list of the properties of HDPE and PDMS [92][93]

Materials	HDPE	PDMS
Density (g/cm^3)	0.94	0.96
Operating temperature (°C)	<71	<350
Tensile strength (MPa)	32	2.24–6.7
Thermal expansion coefficient (10^{-5} cm cm/°C)	6-7	0.031
Thermal conductivity (W/m.K)	0.33	0.27

Furthermore, previously in our group the stopping power of PDMS polymer nanocomposite under the high-energy proton beam was investigated and reported [18]. In this study, samples were irradiated by the proton beam with an incident energy of 63 and 105 MeV and a beam density of 5 nA (2 × 108 protons cm^{-2} s^{-1}). Figure 3-1 shows the dose rate characteristics (BIC/DIC vs. RS values) of the samples. Water equivalent thickness (WET) of the samples and the RS90% (range shifter) values were calculated as listed in Table 3-2. Therefore, the weight and the stopping range of materials corresponding to the same proton energy were compared. Figure 3-2A shows the calculated SR_{AD} of materials. Both pure PDMS and PDMS/SWCNT have a weight advantage of up to 18.3% and 20.84%, respectively, in comparison with Al, under the proton energy of 105 MeV.

In this research the secondary neutron generation were also evaluated. According to the results, both pure PDMS and PDMS/SWCNT has less secondary neutron in comparison with Al. In addition, with increasing the proton energy, PDMS composite has even fewer secondary neutron in comparison with pure PDMS, which indicates the secondary radiation absorption ability of SWCNT in the nanocomposite.

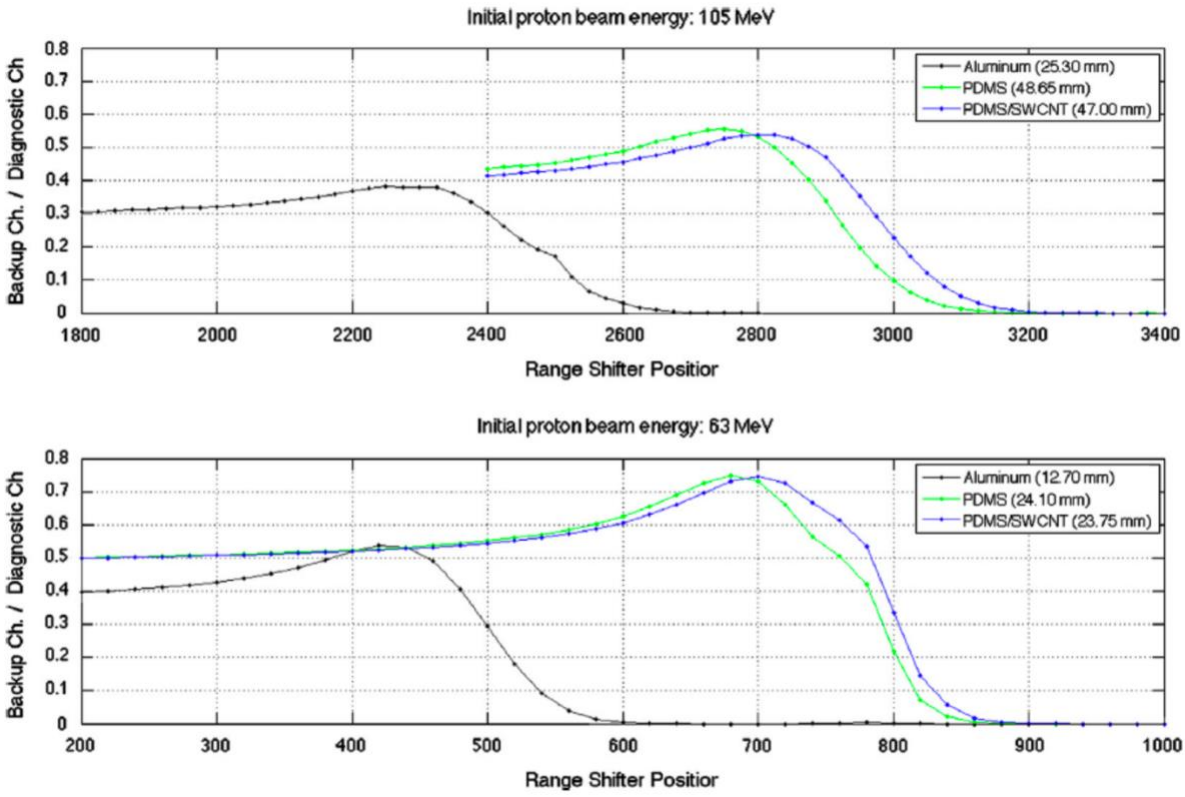

Figure 3-1. Dose rate characteristics of Al, PDMS, and PDMS/SWCNT, irradiated by proton beams with (A) 105 and (B) 63 MeV energies. The legends show the thickness of samples

Table 3-2. Calculated WETs of materials for different ion energies

Initial Proton Energy (MeV)	Material	Density (g/cm^3)	Thickness (mm)	$RS_{90\%}$	Experimental WET (mm)
105	Al	2.698	25.30	2368	52.77
105	PDMS	1.033	48.65	2844	47.22
105	PDMS/SWCNT	1.038	47.00	2889	46.70
63	Al	2.698	12.70	462	25.26
63	PDMS	1.033	24.10	717	22.30
63	PDMS/SWCNT	1.038	23.75	738	22.05

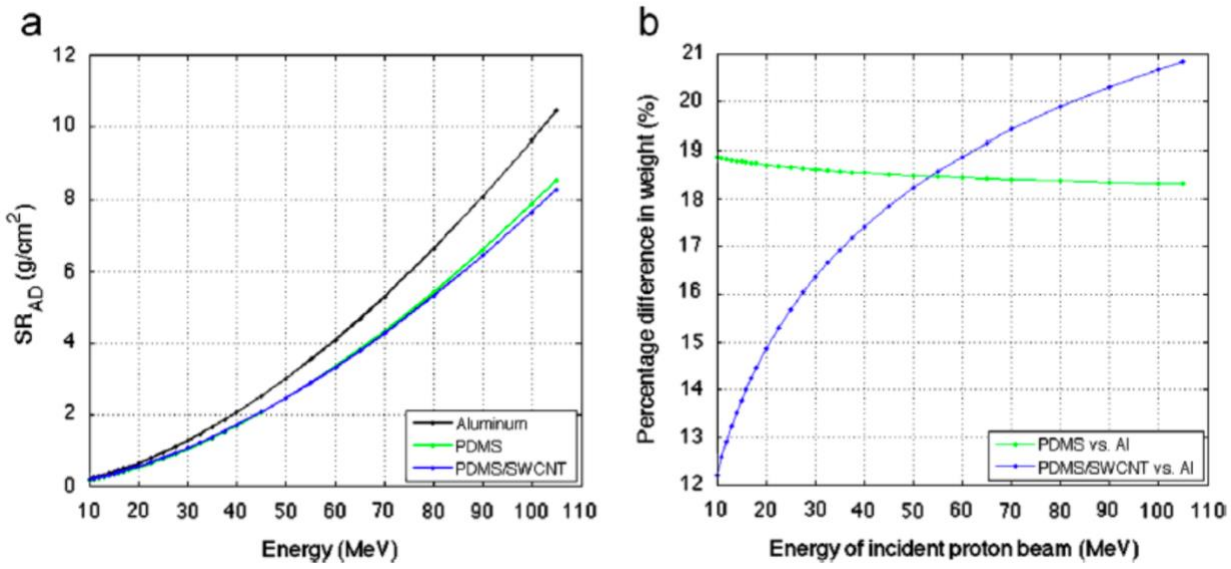

Figure 3-2. (A) SR_{AD} of PDMS, PDMS/SWCNT, and Al. (B) Percentage in weight difference of PDMS and PDMS/SWCNT with respect to Al.

Therefore, according to the promising results and excellent performance, PDMS is considered the polymer matrixes in this project for further investigations. The properties of applied PDMS are listed in Table 3.3.

Table 3-3. Properties of purchased PDMS

Formula	$(C_2H_6OSi)_n$
Density at 25 °C (g/cm^3)	0.98
Melting point (°C)	-50
Transition temperature (°C)	-150

3.1.2 Multi-Walled Carbon Nanotube (MWCNT)

When carbon-based filler materials, like carbon nanotubes, carbon micro-/nanofibers, and graphite, are applied as fillers and reinforcements in various polymers (plastics and resins), they perform high radiation resistance property, high strength-to-weight ratio, and enhanced physical properties. As a result, the carbon composites have been distinguished as suitable materials in applications requiring ultra-lightweight materials and mechanical strength [18][94].

Since the discovery of CNT in 1991 by Iijima [95], it has been studied and applied in various fields such as materials science, physics, chemistry, etc. CNT is a unique nanostructured material with remarkable chemical, mechanical, and physical properties.

Although several studies have evaluated the CNTs effect on improving the mechanical and thermal properties of polymer/CNT composites, only few groups have considered the ionizing radiation shielding performance in CNT/polymer composites [12][96][97]. In one of the very first studies, Clayton et al. (2007) fabricated and characterized PMP reinforced with 0.5 wt.% loading of SWCNT [98]. They illustrated the good mechanical properties and high shielding performance of this composite and concluded that it can be replace PE as shielding materials against GCR. Moreover, experimental results of our group show that a relatively low loading of SWCNTs (about 1.12 wt.%) can improve the proton shielding performance of PDMS polymer [18].

In addition to SWCNT, the effect of MWCNT in radiation shielding application should be evaluated. In one study, the SWCNT and MWCNT deformation after irradiation was investigated by S. Mathew et al. (2011). According to their results, MWCNT shows less disorder in Raman spectrum after 2 MeV electron irradiation [20]. Besides that, more studies confirmed that MWCNT can perform better under charged particle radiations than SWCNT [22][99]. Ionizing radiation triggers the bridging in inter-layer graphene layers of MWCNT, which leads to increasing the thermal conductivity. Therefore, MWCNT is an excellent candidate for ionizing radiation shielding applications. The properties of applied MWCNT are listed in Table 3.4.

Table 3-4. Properties of as-received MWCNT

Average Length (μm)	10 – 30
Outer Diameter (nm)	<8
Content of -COOH	5.58
Carbon Purity (wt.%)	>95

3.1.3 Hexagonal boron nitride (h-BN)

Like graphene, hexagonal boron nitride has a layered structure formed by Nitrogen and Boron atoms. Each C-C bond is replaced by a B-N bond, and the layers are holding to each other by a Van Der Waals force [100]. Among all the elements, boron has the highest neutron absorption cross section, the feature which is higher in nitrogen in comparison with carbon [101]. Recent studies on hydrogen, boron, and nitrogen containing materials have shown effective shielding against hazardous radiations including galactic cosmic radiation (GCR), secondary neutrons, and solar particles [102]. S. Thibeault. (2012) investigated hydrogen-containing boron nitride compounds shielding effectiveness against GCR and SEP at NASA Langley Research Center (LaRC). Figure 3-3 shows the results of calculated GCR dose equivalent for some of the radiation shielding materials, including boron nitride with different hydrogen percentage. Liquid hydrogen (LH_2) performs the best shielding; however, according to the safety and feasibility issues, it is not suitable to be used in spacecraft. The next best material is the BN + 20% hydrogen [87][101].

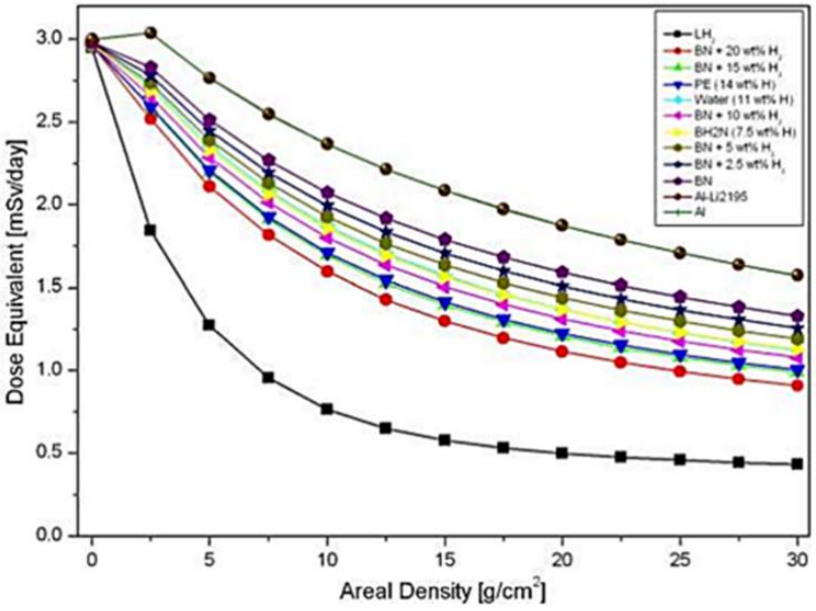

Figure 3-3. GCR dose equivalent for various materials [87]

In addition, h-BN possesses an extremely high in-plane thermal conductivity of 400 W/mK at room temperature, which almost matches that of copper and silver. Cuiping Yu. (2017) fabricated

a BN/epoxy composite with high thermal conductivity of 9 W/mK, which is enhanced by ~45 times compared with the neat epoxy (0.15–0.35 W/mK) [103].

Therefore, h-BN with high H_2 uptake and promising effects in long-term space exploration, is incorporated into the polymer matrix and investigated more for radiation shielding application. The properties of applied h-BN are listed in Table 3-5.

Table 3-5. Properties of purchased h-BN

Apparent Density (g/cm^3)	2.29
Average size (nm)	800
Specific Surface Area (m^2/g)	3.5-6
Purity (%)	>99.8

3.1.4 Bismuth oxide (B_2O_3)

Bismuth oxide (Bi_2O_3) nanoparticle has been studied as an efficient shielding material. It is provided with a high bandgap (2.3-3.3 eV), high total stopping power comparing to Pb (Bi: 2.433 and Pb: 2.407 MeV cm^2/g at electron energy of 10 MeV), and non-toxic property [104]. Therefore, addition of Bi_2O_3 in PDMS polymer is expected to potentially improve the attenuation of electron radiations. Figure 3-4 shows the stopping power of Bi_2O_3 at electron energies up to 1000 MeV.

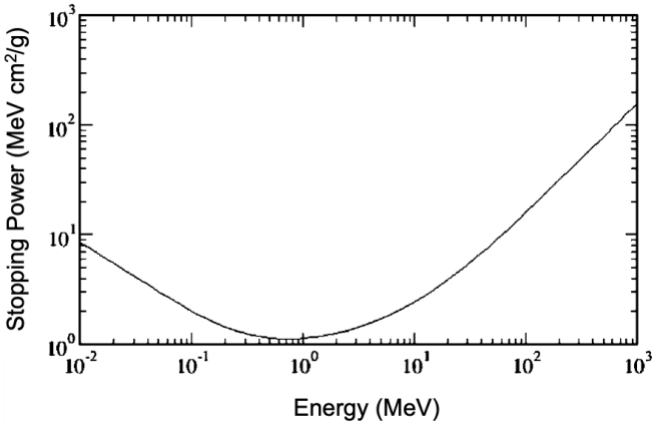

Figure 3-4. Bismuth stopping power.

The properties of applied Bi_2O_3 listed in Table 3-6.

Table 3-6. Properties of purchased Bi_2O_3

Apparent Density (g/cm^3)	8.9
Average Size (nm)	300
Purity (%)	>99.8

3.1.5 Two-Dimensional MXene

Two-dimensional (2D) materials have become major research interest since the discovery of graphene and its outstanding properties. In recent years, a new family of 2D materials has been developed, known as MXene, with distinct chemical, physical, and structural properties which makes it potential for many applications [105].

MXene has a chemical formula of $M_{n+1}X_nT_x$ in which the M represents transition metals, X refers to carbon or nitrogen, T is the surface functional groups or elements, such as OH, O, C, and/or F [106].

The synthesis of these novel materials is through selectively etching layers of sp elements from MAX phases, using HF, NH_4HF_2. MAX phases are three-dimensional (3D) layered metal carbides, nitrides, or carbonitrides, with a general formula of $M_{n+1}AX_n$ (n = 1, 2, 3), where M stands for early d-block transition metals, A represent main-group sp elements, and X represent and either or both C and N atoms. Some of established MXene family are Ti_3C_2, Ti_2C, $(Ti_{0.5}, Nb_{0.5})_2C$, $(V_{0.5}, Cr_{0.5})_3C_2$, Ti_3CN, Ta_4C_3, Nb_2C, V_2C, and Nb_4C_3. As shown in Figure 3-5, the surfaces of the exfoliated layers can be terminated with OH, O, and/or F groups during the etching process [107][108].

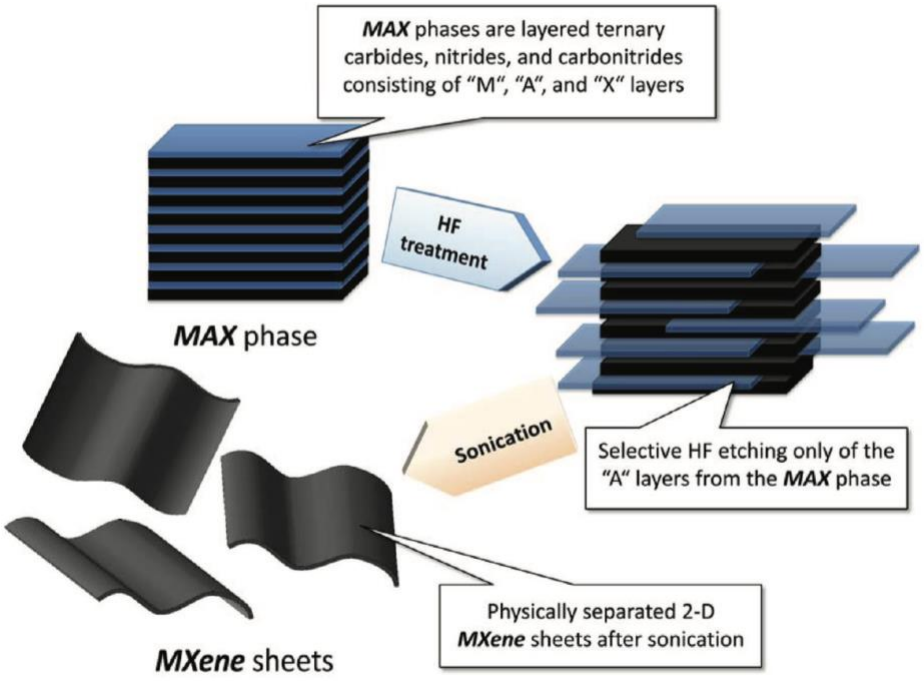

Figure 3-5. Schematic showing the MXene synthesis steps [109].

Since their discovery, MXenes have been investigate for many applications such as sensors, catalyst, electrode materials for batteries, energy storage, etc. [110][111][112] Herein, MXene was selected to be incorporated into the polymer matrix and investigated more for radiation shielding application. The two types of MXene and their properties are listed in Table 3-7.

Table 3-7. Properties of purchased MXene

Material	**Ti_3C_2T**	**Mo_2CT**
Colour	Black	Gray
Average size (nm)	50-150	50-100
Number of layers	1-5	1-5
Purity (%)	99	99

3.2 Fabrication Methods

3.2.1 Physical Blending

Physical blending is a method to prepare PDMS polymer nanocomposites. In this method, PDMS and nanomaterials such as MWCNT and Bi_2O_3 can be mixed by mechanical blending, which can disperse the nanofillers in polymer matrix by producing enough sheer stress. The mechanical shear forces, generated by the interaction process between powders and screws, separate the MWCNT and Bi_2O_3 bundles and provide a good dispersion of nanotubes and nanoparticles in the polymer matrix. Finally, the well-mixed melt can be molded into the desire shape [113].

3.2.1 Solution Mixing

Among different methods for polymer composites fabrication, solution mixing is a straight-forward method in which the prepared solution of the nanomaterial is added to polymer solution followed by mechanical stirring. This method has shown remarkable impacts in the uniform dispersion of the nanoparticles. Homogeneous dispersion of conductive nanoparticles improves the structural properties and constructs conductive networks in the composite resulting in better electrical properties [114].

The chemical solutions such as tetrahydrofuran (THF) and toluene can be used to dissolve PDMS and MXene and OHBN can be dispersed in the dissolved PDMS solution by ultrasonic dispersion method. Afterward, the resulting solution will be poured into the Teflon mold and left in a vacuum oven to evaporate the solvent [115].

It should be noted that the interfacial interactiin between the fillers and the matrix affects the nanocomposite properties. The interface interactions could be improved by treating the filler surface chemistry [116].

3.2.2 Hydrothermal treatment

Hydrothermal synthesis and treatment method is an immensely powerful technique to produce different functional nanomaterials of hydroxides and oxides of transition-metal compounds. Hydrothermal Autoclave reactors are usually applied to prepare the high temperature and high

pressure required for the hydrothermal reaction. Both high temperature and pressure help with creating an ambient condition for nanomaterials treatment and/or synthesis. The process also requires solutions with a corrosive impact on the interior material of the autoclave [117][118]. In this project, hydrogen peroxide 30% was used as the corrosive solution. Figure 3-6 shows the autoclave parts. These sealed cylinders can endure high pressure and temperature for a long duration.

Figure 3-6. The autoclave parts and the cylindrical Teflon

3.3 Radiation Shielding Tests

3.4.1 Linear Particle Accelerator (LINAC)

LINAC is a device to accelerator ions, charged subatomic particles, or photons using series of oscillating electric potentials along a linear beamline [119][120]. The medical-purpose LINAC machine, which is used in this research, is located at the Grand River Hospital (GRH), Kitchener, and can produce photons (up to 15 MeV) and electron beam (up to 20 MeV) (Figure 3-7).

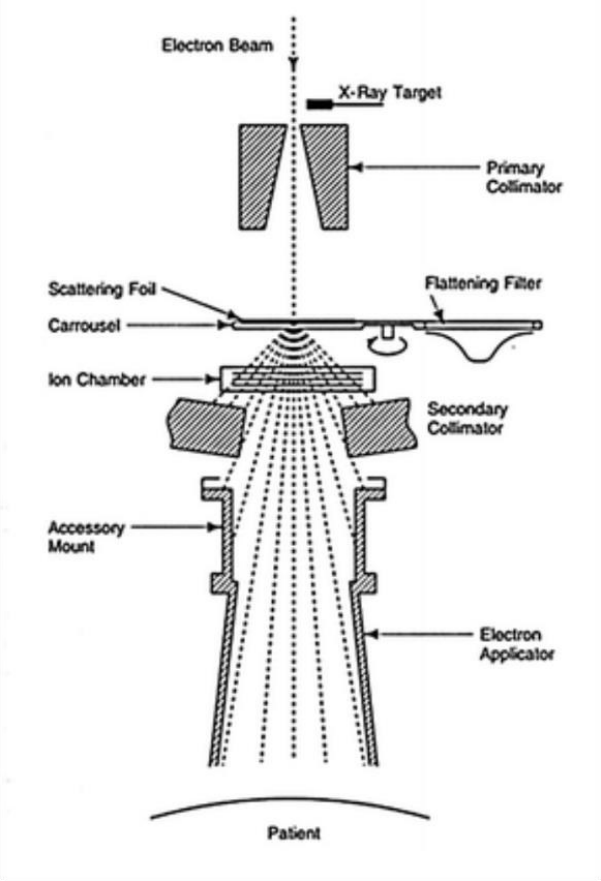

Figure 3-7. Scheme of LINAC [119]

In this research, LINAC was used to simulate the electron radiation in space. Electron beam with 6, 9, 12, 16 and 20 MeV were applied. As discussed in literature review, electron with energies up to 7 MeV have most dense dose in LEO. However, looking upon interplanetary travel, such as journey to Jupiter, electron flux with energies up to 20 MeV predominantly contribute radiation dose on spacecraft.

3.4.2 Photon Shielding Test Setup

The x-ray attenuation experiment was performed at Advanced Micro- /Nano- Devices Lab, University of Waterloo. The x-ray machine in this lab is working based on field emission method, by free-standing CNT FEAa cathode. The cathode fabrication process is explained in Appendix A. The cathode and target (tungsten) are place in a thick stainless-steel chamber which is connected to a high voltage generator, as figure shows.

To measure the dose, a calibrated “Shad-o-Box 1548 HS” detector (Teledyne DALAS, Ontario, Canada) was applied as Figure 3-8 shows.

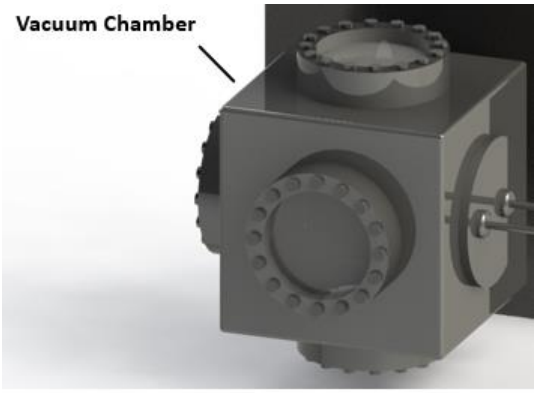

Figure 3-8. Schematic of the x ray tube

Chapter 4 Lightweight and Flexible Polymer Nanocomposite with Enhanced X-Ray Shielding Efficiency

One of the effective parameters in radiation shielding efficiency of nanocomposites is the nanofillers dispersion quality. Uniformly dispersed nanofiller in polymer matrix provides better thermal and mechanical properties and radiation shielding effectiveness.

This chapter is an initial study to develop a nanocomposite with well dispersed nanofillers. As introduced in previous chapter, Bi_2O_3 and MWCNT were selected as nanofillers. PDMS/BiO nanocomposite with 5, 10, 15, 20, and 30 wt.% Bi_2O_3 content and PDMS/CNT samples with 1, 5, and 10 wt.% MWCNT content were fabricated and characterized. All the samples have a thickness of 1 mm. Also, to evaluate the nanocomposites shielding performance, a preliminary experiment conducted through irradiating all the samples by x-ray with 60, 70, 80, and 90 KeV energies.

X-ray is one of the secondary radiations that can be produced during the electron and/or ionizing radiation interaction with shielding material. Not only it is important to prevent secondary x-ray generation in space applications, but also x-ray shielding on earth is a great concern. With the development of technology, x-ray is widely used in different applications especially for medical purposes like radiotherapy and medical diagnosis. However, human exposure to this radiation can cause biological problems, such as the development of cancer, and in extreme cases, fatality [121]. To protect individuals from x-ray exposure, lead-based products are commonly applied [122][123]. However, heavy weight, toxicity, and lack of flexibility have limited the application of lead-based products when wearability and portability are required. Therefore, conventional lead-containing protection typically needs to be replaced with novel ones [124][125].

In recent decades, polymer composites containing high atomic number (Z) fillers are characterized by good x-ray absorption and known as promising candidates to replace lead [126][127]. PDMS is one of the greatest candidates in this regard, because of its high flexibility, biocompatibility, and

easy fabrication [42][77][60]. Furthermore, bismuth oxide (Bi_2O_3) is a highly recommended nanomaterial to replace Pd due to its key features like nontoxicity, high radiation absorption (K-absorption edge 90.5 keV), and low cost. Seda Nur Yılmaz et al. (2020) explained that an 8.4 mm PDMS/Bi_2O_3 composite, containing 40 wt.% Bi_2O_3 can attenuate 96.4% of the x-ray with 100 keV tube energy [128]. Muthamma et al. (2018) also investigated polyvinyl alcohol (PVA)/Bi_2O_3 composites for x-ray protection and studied the effect of filler loading up to 50 wt.% on shielding efficiency and exhibited the weight advantages of the composite over lead (Pb) [129]. However, it is difficult to disperse a large percent of fillers uniformly in such polymer matrices, and the resulting composite may suffer from insufficient mechanical strength [121].

In addition to the effect of filler content, the shielding efficiency of multilayer structure is investigated by fabricating PDMS/BiO – PDM/CNT multilayer nanocomposite in 2 to 5 layers. As explained in Chapter 2, section 2.5.2, multilayer design is an effective approach to uniformly disperse more than one filler in polymer matrix [29][30][26]. In recent studies, Li et al (2021) fabricated a multilayered composite of bismuth/ethylene-octene and tungsten/ethylene-octene copolymers and showed the effect of multilayered structure on improving the x-ray shielding efficiency [130]. Also, Gilys et al. (2022) fabricated a layer nanocomposite of PDMS/tin, PDMS/cerium, PDMS/tungsten, and PDMS/bismuth composites which demonstrated almost the same x-ray attenuation as the conventional x-ray shielding materials [29].

4.1 Experiment

4.1.1 Method and fabrication

The fabrication schematic of composites is shown in Figure 4-1a. Firstly, PDMS was prepared by mixing the base polymer and the curing agent with a 10:1 weight ratio. For making different nanocomposites, various weight percentage of Bi_2O_3 and MWCNT, as Table 4-1 shows, was dispersed in liquid polymer using mechanical stirring (VWR hotplate stirrer) at 1000 rpm for 1 hour (Figure 4-1 A1). The mixtures were then vacuumed for 30 seconds to release the trapped air bubbles during the mixing process (Figure 4-1 A2). Finally, the prepared compounds were shaped by a 10 * 10 * 1 mm molds, with 1mm thickness, and baked in the oven at 70°C for 3 h with 20 MPa pressure (Figure 4-1 A3 and A4). Figure 4-1 B1 to B4 exhibit digital photos of fabricated

samples. Also, a specific code designated for each sample (Table 4-1) to be used in the following sections.

Table 4-1. List of prepared composites with various filler and polymer content, and the designated code to each sample

Filler type	Filler wt.%	PDMS wt.%	Sample designated code
No filler	0	100	PDMS
Bi_2O_3	5	95	PDMS/BiO5
	10	90	PDMS/BiO10
	15	85	PDMS/BiO15
	20	80	PDMS/BiO20
	30	70	PDMS/BiO30
MWCNT	1	99	PDMS/CNT1
	5	95	PDMS/CNT5
	10	90	PDMS/CNT10

Additionally, multilayer PDMS nanocomposites were fabricated through the spin coating method with the order of layers that Table 4-2 indicates. In this regard, first, a layer of PDMS/BiO30 was spin-coated on a silicon wafer (Figure 4-1 A3) and moved to the oven to bake at 70°C for 1 hour (Figure 4-1 A4). Afterward, a layer of PDMS/CNT5 was spin-coated on the top (Figure 4-1 A3), as the second layer, and moved to the oven again to bake for another hour (Figure 4-1 A4). All the layers were heating and drying out together in such a manner. Therefore, 1 mm thick multilayer composites in 2, 3, 4, and 5 layers were fabricated using two composites (PDMS/BiO30 and PDMS/CNT5) stacked on each other. Detailed information on layered samples is included in Table 4-2. Also, the thickness of each layer in different samples is included in Table 4-2. The thicknesses were defined during the fabrication prosses. For example, to fabricate the 2-layer nanocomposite, half weight of 1 mm thick PDMS/BiO30 and half weight of PDMS/CNT5 samples were considered, then fabricated the 2-layer sample using these values to have 0.5 mm thick of each composite in different layers. Same steps followed to fabricate all the samples. Figure 4-1 C shows the digital images of layered samples on a millimeter scale to confirm the thickness of samples. The images were prepared by ImageJ software. An optical microscopic image of 3-layer nanocomposite (as an example) is shown in Figure 4-1 C to confirm the layers thicknesses.

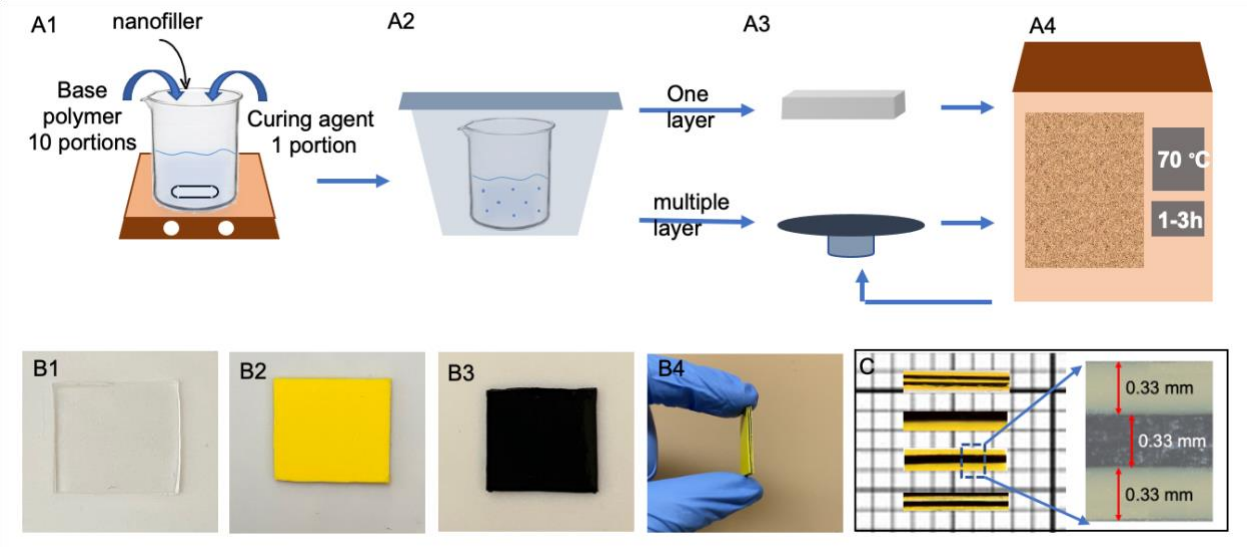

Figure 4-1. (A) schematic of the fabrication process, (A1) mixing component by a mechanical mixer, (A2) putting the mixture under vacuum to release the trapped air, (A3) molding the solution for one layer composite or applying spin coater to fabricate the layered structure, (A4) placing the samples in the oven to bake at 70 °C for 3 h, (B) digital photos of fabricated (B1) PDMS, (B2) PDMS/BiO30, (B3) PDMS/CNT5, and (B4) 5-layer nanocomposites, (C) digital images multilayer samples and an optical image of 3-layer nanocomposite to show the thickness of each layer

Table 4-2. Layered nanocomposite composition

Samples	**First layer**	**Second layer**	**Third layer**	**Fourth layer**	**Fifth layer**	**Thickness of layers (each) [mm]**	**Designated code**
1-layer	PDMS/BiO30	-	-	-	-	1	1-layer
2-layer	PDMS/CNT5	PDMS/BiO30	-	-	-	0.5	2-layer
3-layer	PDMS/BiO30	PDMS/CNT5	PDMS/BiO30	-	-	0.333	3-layer
4-layer	PDMS/CNT5	PDMS/BiO30	PDMS/CNT5	PDMS/BiO30	-	0.25	4-layer
5-layer	PDMS/BiO30	PDMS/CNT5	PDMS/BiO30	PDMS/CNT5	PDMS/BiO30	0.2	5-layer

4.1.2 Characterization

To characterize the chemical structure of fabricated nanocomposites, Fourier Transform Infrared (FTIR) spectroscopy (Bruker, tensor 27) was applied at 400 cm^{-1} to 4000 cm^{-1} wavenumbers.

FTIR spectroscopy is useful to obtain samples molecular ‘fingerprint’ and observe the possible chemical structure change in developed composites [104].

Surface morphology and fillers dispersion of developed nanocomposites was evaluated by Zeiss Ultra plus SEM at different magnitudes. The fabricated composites were cut into small pieces and placed on aluminum stubs using double-sided carbon tapes. To make the prepared samples electrically conductive and improve the image quality, a thin layer of gold (~20nm) was deposited on them by a gold sputter coater (Denton Desk II model).

Regarding the mechanical property of nanocomposite materials, the tensile strength of samples was measured by Instron 5548 Micro Tester, according to the ASTM D412, with a 10 kN load cell and 50 mm/min crosshead speed. To prepare the samples with the required shape and dimensions, a laser engraving system was applied.

An x-ray attenuation experiment was performed at Advanced Micro- /Nano- Devices Lab, University of Waterloo, with a target material of tungsten. A 1 mm aluminum filter was placed in front of the tube window, to cut low-energy photons and increase the average energy. Figure 4-2 shows the test setup. Developed samples with 1 mm thickness were placed at 50 cm in front of the x-ray source. To measure the dose, a calibrated “Shad-o-Box 1548 HS” detector (Teledyne DALAS, Ontario, Canada) was applied as Figure 4-2 shows. Applied current and irradiation time were 100 μA and 3 s, respectively, while the voltage was in a range of 60 to 90 kV to generate a continuous x-ray. X-ray images were analyzed using MATLAB and Statistics Toolbox Release 2021a, The MathWorks, Inc., Natick, Massachusetts, United States. The transmission factor values of the samples were calculated.

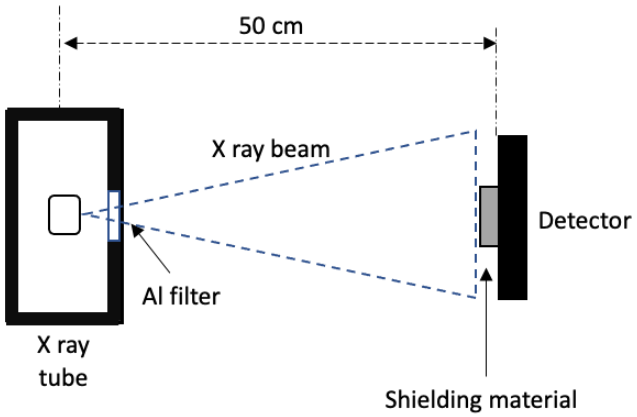

Figure 4-2. Schematic of the x ray experiment setup

Furthermore, the Archimedes method was applied to calculate the apparent density of all samples. An electrical single pan balance and ethanol were used to measure the weights and substitute in the following formula (Equation 4-1).

Equation 4-1

$$\rho = \frac{m_1}{m_2 - m_3}\,\rho_l$$

Where m is the mass of developed samples weighted on the balance (m_1), the mass of the sample hanging on balance arm in the air (m_2), and the mass of the sample hanging on the balance arm immersed in ethanol (m_3), and ρ_l represents the density of ethanol.

Equation 4-2 was applied to calculate the theoretical densities (ρ_c).

Equation 4-2

$$\rho_c = \frac{100}{(\frac{F}{\rho_f} + \frac{E}{\rho_c})}$$

Here F and E are the wt.% of the filler and PDMS, respectively. Also, ρ_f and ρ_c are densities of filler and PDMS. The results were compared with the density of lead as the reference material, afterward.

4.2 Result and discussion

4.2.1 Chemical composition analysis

The chemical bonds in all samples were evaluated and compared with neat polymer using FTIR spectroscopy. As it can be seen from Figure 4-3, PDMS main vibration is the dominant peak in both spectrums (Figure 4-3 A and B). Peaks at around 780 and 1260 cm^{-1} represent the rocking and bending peaks of the Si–CH_3, respectively. The peaks at about 1010 and 1064 cm^{-1} were assigned to the asymmetric and symmetric Si–O–Si stretching bonds, correspondingly [131], and the small peak at around 2960 cm^{-1} belongs to CH_3 asymmetric stretching in Si-CH_3. Figure 4-3 A also shows the FTIR spectrum of PDMS/BiO nanocomposite, a change in shape and intensity of the peaks appears at around 619 cm^{-1} with increasing the Bi_2O_3 content which corresponds to the Bi-O group in Bi_2O_3 [132][129].

As the arrow indicates, the peak intensity increases for PDMS/BiO20 and PDMS/BiO30, which means bismuth oxide particles have been incorporated and dispersed into the polymer, successfully. However, the peak intensity is still low compared to the other peaks since the prominent PDMS peaks are highly intense and they can overlap with other vibrations [128]. In addition, Figure 4-3B exhibits the FTIR spectra of neat polymer and PDMS/CNT nanocomposites. At about 906 cm^{-1} there is a minor peak shift towards lower wavenumbers as the concentration of MWCNT increases. In addition, comparing the black line (PDMS sample) and the green line (PDMS/CNT10) at 906 cm^{-1}, with increasing MWCNT content (PDMS/CNT10), the peak shape changes as highlighted in Figure 4-3 B. The change in peak position and peak shape confirms the Si-C bond formation, and it is in agreement with the literature [133][134].

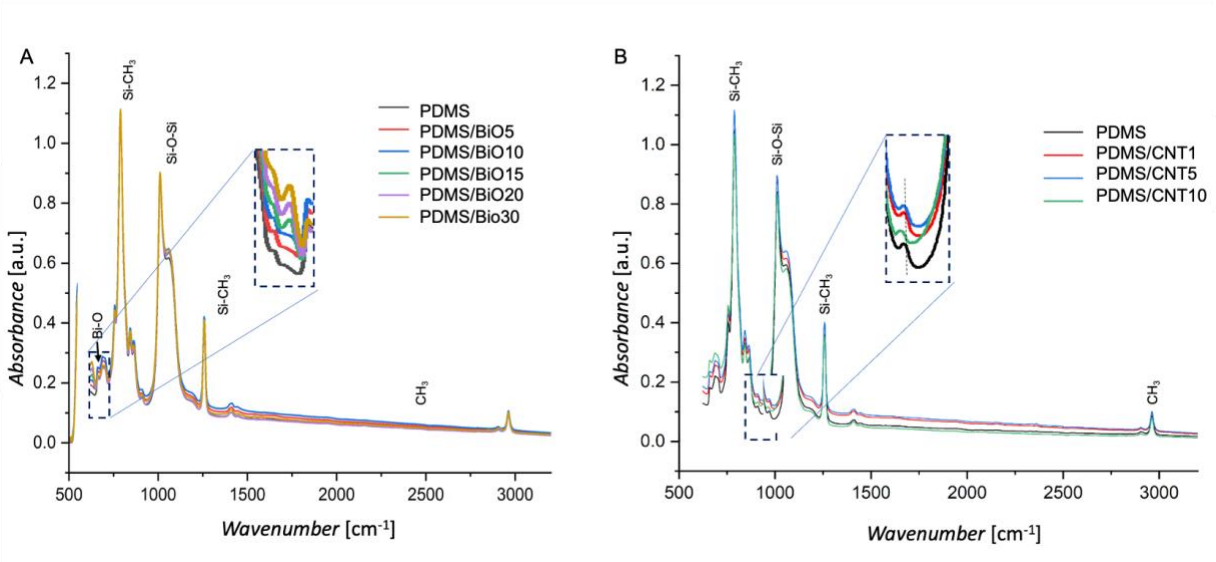

Figure 4-3. FTIR pattern of (A) neat PDMS and PDMS/BiO nanocomposites, (B) neat PDMS and PDMS/CNT samples.

4.2.2 Microstructure evaluation

The effect of increasing content of Bi_2O_3 and MWCNT nanoparticles on mechanical strength and x-ray shielding performance of nanocomposites were also studied. Filler loading in polymer-based composites leads to an increase in mechanical strength and shielding performance [42][135]. However, too much filler content is not favorable since it would increase density and decrease the flexibility of the composites, both of which limit the shielding material application. Also, in high filler loading nanocomposites, it is difficult to uniformly disperse nanoparticles. Poor nanofiller dispersion in polymer matrix leads to aggregations, creates nano and micro defects inside the composite, and decreases the tensile strength. Therefore, the microstructure of samples and the dispersion of Bi_2O_3 and MWCNT nanoparticles in the polymer matrix were characterized with SEM in various magnifications. The tensile strength test was also performed, afterward.

To better evaluate the effect of Bi_2O_3 on surface morphology, samples with the highest filler content (15, 20, and 30 wt.%) were analyzed using SEM (Figure 4-4A). The neat polymer possesses a smooth surface with no pores and cracks (Figure 4-4 A1). For the samples with 20 and 30 wt.% filler, no significant changes were observed in surface morphology (Figure 4-4 A2 and A3). Nanofiller dispersion in the polymer matrix was evaluated by looking at cross-section SEM

images (Figure 4-4 B). For low filler loading composites, particle dispersion seems homogenous. According to the nanofillers size (~300 nm) and the image magnification (x25000), the white dots in Figure 4-4 B1 and B2 seem to be uniformly distributed spherical particles in PDMS/BiO15 and PDMS/BiO20 composites. Increasing the filler content to 30 wt.%, individual nanofillers can still be recognized according to Figure 4-4 B3. In some parts, two or three particles can be seen close to each other, but no area of aggregation was noticed.

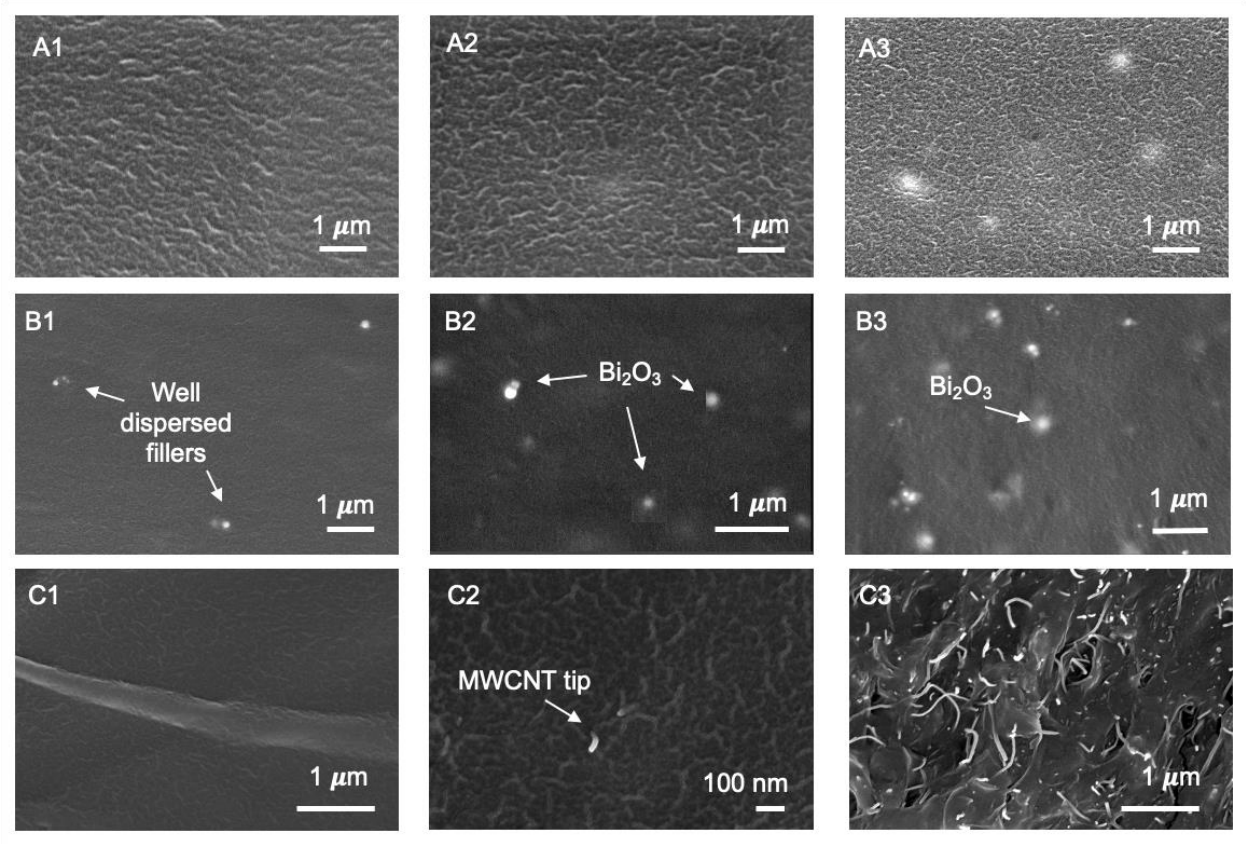

Figure 4-4. SEM images of the surface of a) samples surface (A1) PDMS, (A2) PDMS/BiO20, (A3) PDMS/BiO30. Also, the SEM pictures from the cross-section of samples are (B1) PDMS/BiO15, (B2) PDMS/BiO20, and (B3) PDMS/BiO30, (C1) PDMS/CNT1, (C2) PDMS/CNT5, (C3) PDMS/CNT10.

In addition, uniform dispersion of MWCNT is observed for PDMS/CNT1 and PDMS/CNT5 samples due to Figure 4-4 C1 and C2. However, dense areas bundle of MWCNT are considerable in higher loading composites (PDMS/CNT10) (Figure 4-4 C3), as in high nanofiller containing samples, the large aspect ratio of nanoparticles leads to a tendency to aggregation and results in poor dispersion [136][137].

4.2.3 Mechanical properties

To investigate the effect of applied nanofillers on PDMS mechanical properties, tensile strength, and elongation at break of developed nanocomposites were measured using Instron 5548 Micro Tester (Figure 4-5B). Nanofillers can lead to polymer reinforcement if they are well dispersed in the polymer matrix because uniform dispersion leads to uniform stress distribution in the matrix and efficient load transfer onto the nanofiller. According to the results in Figure 4-5A, the addition of Bi_2O_3 improves the tensile strength as well as elongation due to the stress transfer from polymer to metal oxide nanoparticles. Figure 4-5C and D SEM images indicate how Bi_2O_3 nanoparticles improve the matrix mechanical properties. As the figure exhibits, the nanofillers are stopping the microcracks from growing in the matrix and result in tensile strength enhancement. Due to the results in Figure 4-5A, PDMS/BiO30 nanocomposite with the highest tensile strength and elongation should be considered for multilayer nanocomposite.

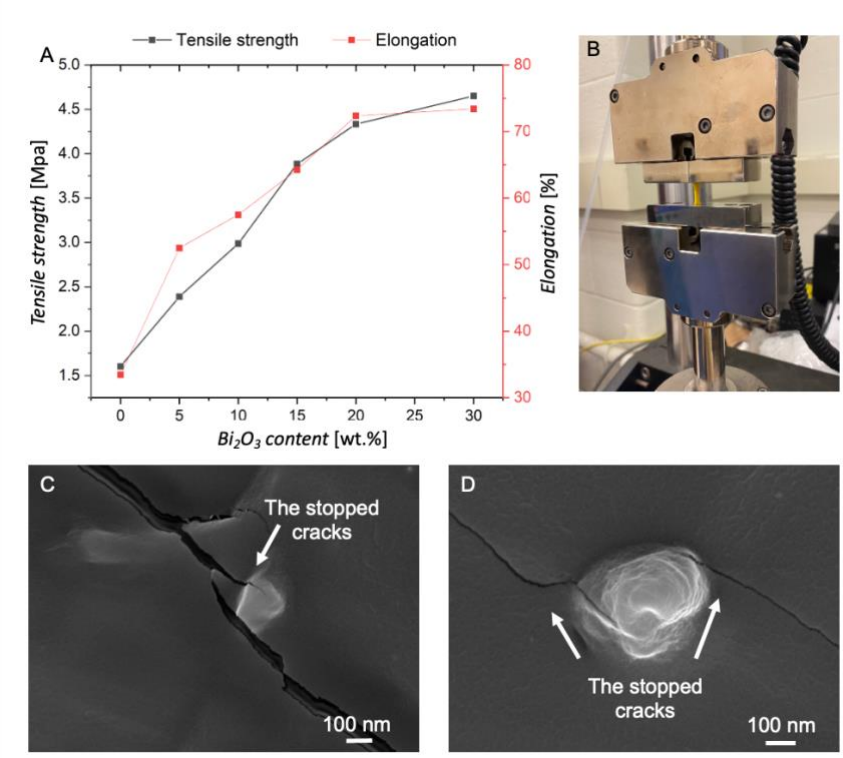

Figure 4-5. (A) Tensile properties of neat PDMS and PDMS/BiO samples with different Bi_2O_3 content, each point represents one of the PDMS/BiO samples as introduced in table 4-1, (B) the micro Instron for tensile strength test, (C), and (D) the SEM images of cracks that have been stopped by nanofiller.

Although uniform dispersion of nanofiller in the polymer matrix is the most critical parameter, there are two other strengthening mechanisms for nanotube reinforced nanocomposites: crack bridging and fiber pull-out [138]. In MWCNT reinforced nanocomposites, nanotubes form bridges across the cracks and gaps (Figure 4-6 B1) and produce a closure stress perpendicular to the crack which leads to an improvement in tensile strength. In addition, the SEM images in Figure 4-6 B2 show the MWCNTs at the fracture area which indicates the nanotube pull-out mechanism while the crack is expanding. During the crack propagation in the polymer matrix, both MWCNT ends remain adhered to the polymer chain and elastic deformation occurs in the nanotube while the crack reaches the nanotube. In fact, because of the extraordinary flexibility and high elastic modulus, MWCNT can absorb significant amounts of crack energy which leads to the elastic extension of nanotubes before collapse or fracture at either side of the fractured surfaces. This behavior leads to tensile strength improvement in samples containing MWCNTs [139][140]. It should also be noted that the large length and small diameter in this experiment help with mechanical properties enhancement since MWCNTs with a high aspect ratio are more effective reinforcements [141][142].

Figure 4-6A shows the tensile strength and elongation at break for PDMS/CNT samples containing 1, 5, and 10 wt.% MWCNT. The mechanical strength increases up to 5.6 MPa for PDMS/CNT5, however, it decreases significantly for PDMS/CNT10 sample because of the nanotube's aggregation, as it was observed in Figure 4-4 C3. Therefore, PDMS/CNT5 nanocomposite is the best candidate to be considered for multilayer nanocomposite. Figure 4-6 C1 and C2 are digital images of the 5-layer sample with great flexibility. In addition, tensile strength, and elongation at the break of multilayer samples with various layers are presented in Figure 4-6 D. The combination of PDMS/BiO30 and PDMS/CNT5 nanocomposites in multilayer structures has shown tensile strength improvement up to 70% in comparison with the neat polymer. Furthermore, tensile strength of the 5-layer sample is increased by 22.3% when compared to the 1-layer nanocomposite.

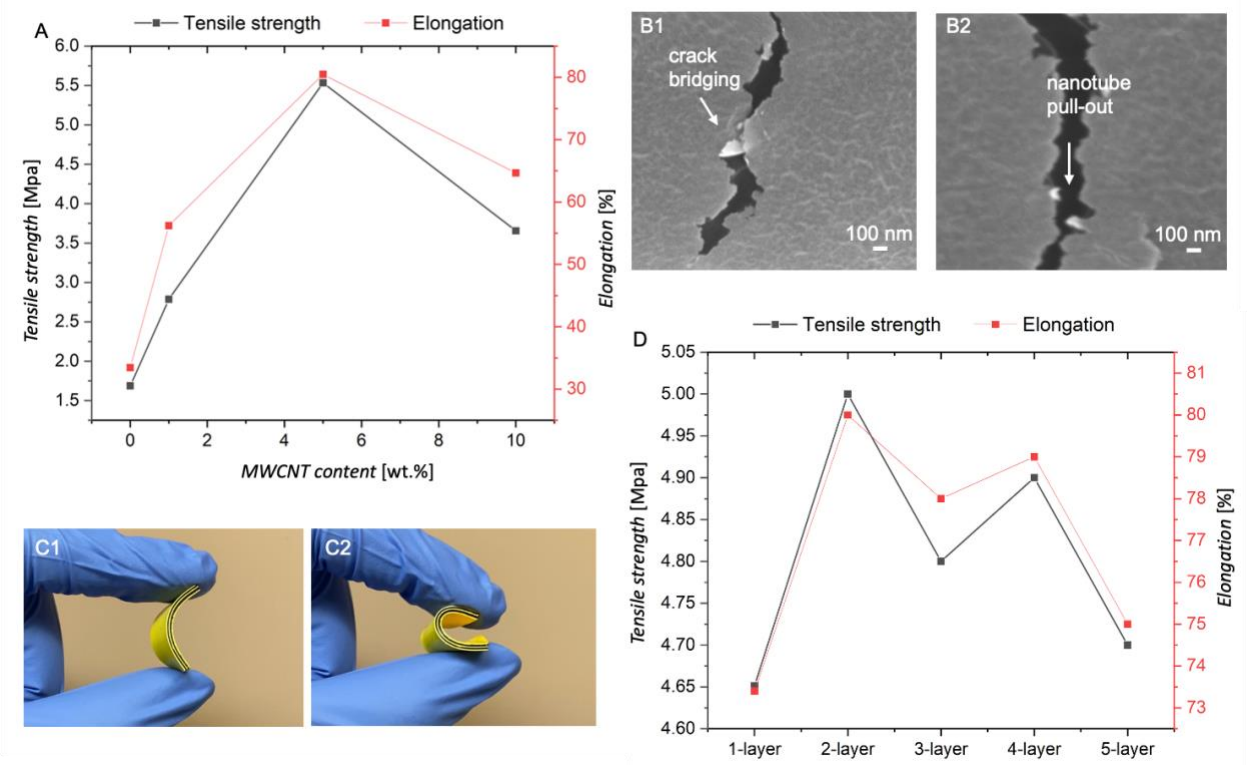

Figure 4-6. (A) elongation at break and tensile strength of PDMS and PDMS/CNT samples with various amounts of MWCNT, (B) SEM images of nanotubes that made a bridge (B1) or pulled out (B2) at cracks, C) flexible 5-layered nanocomposite, and (D) tensile strength of multilayer nanocomposites with different layers number.

4.2.4 X-ray shielding measurements

To study the x-ray shielding performance of all samples, they were irradiated by x-ray with different energies (60, 70, 80, and 90 keV) one by one. The transmitted photons were measured through the detector, as was exhibited in Figure 4-2. Schematic of the x ray experiment setup. To investigate the x-ray shielding performance of each nanocomposite, the percent of transmission factor (I/I_0%) was calculated; where I and I_0 are the number of transmitted photons with and without shielding materials, respectively.

As Figure 4-7A shows, the I/I_0% decreases by increasing the Bi_2O_3 content. The neat PDMS transmits more than 90% of x-rays with various voltages (Figure 4-7A), however, adding Bi_2O_3 into the PDMS matrix remarkably improves the x-ray shielding ability by decreasing the I/I_0% value. According to the results, the optimal I/I_0% value for the samples reached 32% for

PDMS/BiO30 nanocomposite under 60 keV X-ray radiations, which means that about 68% of photons can be shielded when interacting with PDMS/BiO30 sample. The I/I_0% of PDMS/CNT nanocomposites was also measured, and it was in the range of 82% or more, for 60, 70, 80, and 90 keV x-ray radiations, as Figure 4-7B shows.

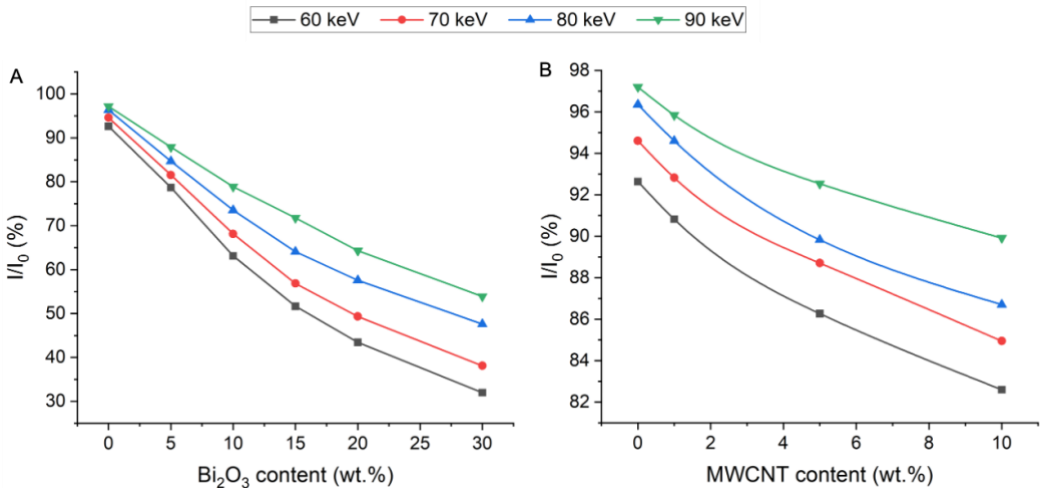

Figure 4-7. x-ray transmission rate (I/I_0 %) of (A) PDMS/BiO nanocomposites with various Bi_2O_3 content, and (B) PDMS/CNT samples with different MWCNT content. In both images, different lines represent the results for different x-ray energies.

Although the results are demonstrating PDMS/BiO30 as potential material for x-ray shielding application in the energy of 60 keV, it still does not display sufficient protection against 90 keV or higher radiation energies, as it is transmitting 53.9% of 90 keV radiation.

The I/I_0% were measured for the fabricated multilayer structures of the PDMS/BiO30 and PDMS/CNT5 nanocomposites afterward. A schematic of the photon attenuation mechanism in nanocomposites with different numbers of layers is shown in Figure 4-8. As the figure shows, more x-rays can be shielded and absorbed as the number of layers is increased from 2 to 5 layers (Figure 4-8), since the localized distribution of nanofillers is more likely to be collided by photons.

In addition, the x-ray radiation is scattered several times through the multiple layers and absorbed between the layers. Meanwhile, the produced secondary K-, L- M- X-rays from the photoelectric effect are also scattered and dissipated through the different layers. Therefore, the primary and

secondary x-rays can be attenuated in multilayer interfaces by scattering, absorption, and dissipation mechanisms [143][130].

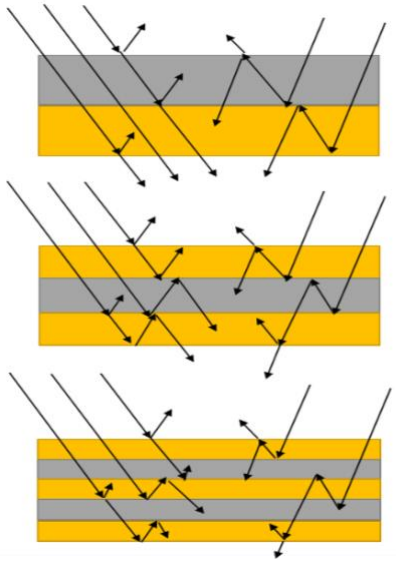

Figure 4-8. a schematic of the multilayer structure shielding mechanism and the effect of increasing the number of layers

Figure 4-9 indicates that the shielding capability of the layered composites significantly increases as the number of layers increases from 2 to 5 layers. It should be mentioned that generally in multilayer structures, the layer containing the high atomic number element is arranged in the first layer, and the lower atomic number element is applied in next layer(s) to absorb the Compton scattered radiations as well as the produced secondary x-rays due to the photoelectric effect in the first layer (the energy of secondary x-rays are lower than the initial x-ray). In this study, we applied multiple layers of PDMS composites containing Bi_2O_3 (as high atomic number filler) and MWCNT (as low atomic number filler) in multilayer composites. Based on Figure 4-9, samples with PDMS/BiO30 composite as the first layer has a lower transmission rate, since the initial x-ray hits and reacts with high atomic number elements first, then the next layers absorb or react with the scattered radiation. However, the x-ray transmutation rate of the 2-layer sample is higher than other samples, which is due to the arrangement of layers. In addition, increasing the number of layers leads to scattering and slowing down more radiations.

Therefore, the 5-layer sample can reach a transmission rate as low as 11.2% for 60 keV radiation.

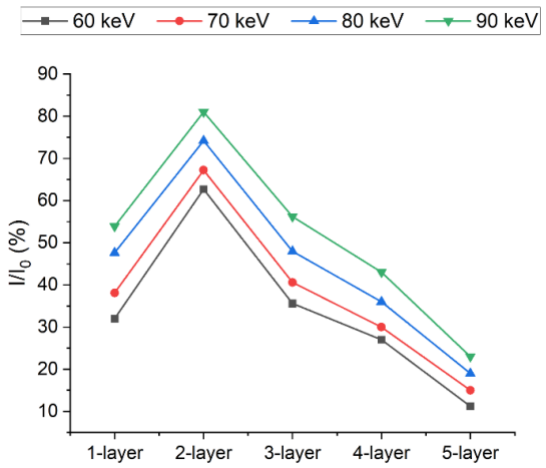

Figure 4-9. x-ray transmission rate (I/I_0 %) of layer nanocomposites with different layers numbers

It also should be noted that increasing the thickness of shielding material can result better shielding efficiency. For example, a 3-layer composite, containing up to 30% Bi_2O_3 in different layers, can reach a transmission rate of 5.8% with a thickness of 6.3 mm [78]. However, the aim of this study was to characterize the transmission rate of a specific thickness of Bi_2O_3-filled polymer (PDMS) nanocomposite and evaluate the effect of changing the structure on shielding performance.

For more comparison, the Attenuation Efficiency (AE) was calculated for samples with best I/I_0% by Equation 4-3, and plotted as Figure 4-10 shows:

Equation 4-3

$$AE\ (\%) = \frac{I_0 - I}{I_0} \times 100$$

The AE is a factor to show the amount of x-ray which is absorbed and/or stopped by the shielding material. As Figure 4-10 shows, the 5-layer nanocomposite has the highest AE number. Comparing the single layer and multilayer PDMS composites, it is observed that the 5-layer structure is associated with the highest AE, and it exhibits optimal shielding performance for x-ray radiation, as it reaches approximately 89% attenuation rate under x-ray radiations with 60 keV energy. This

enhancement is the result of the synergistic attenuation effect of the polymer, nanofillers, and multilayer interfaces [144].

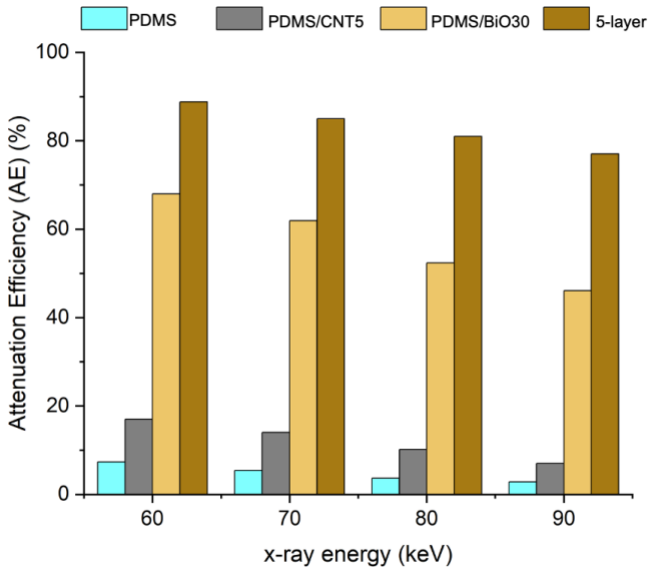

Figure 4-10. a comparison between the attenuation efficiency (AE) of neat PDMS and the nanocomposites

4.2.5 Density of samples

The material density is another crucial factor, as low-density shielding materials are required for wearable and mobile applications [121]. The experimental and theoretical density of the PDMS, PDMS/BiO30, PDMS/CNT5, and 5-layer samples were measured as shown in Table 4-3. The density of fabricated nanocomposites and lead. The small difference between the experimental and theoretical values can be due to experimental errors.

Table 4-3. The density of fabricated nanocomposites and lead

Samples	Theoretical Density (g/cm^3)	Experimental Density (g/cm^3)	% Heaviness
Pb	11.29	11.29	100
PDMS	0.96	0.98	8.54
PDMS/BiO30	1.32	1.35	11.67
PDMS/CNT5	0.99	1.00	8.78
5-layer	1.31	1.29	10.02

To compare the density of developed nanocomposite with that of the lead, percent of heaviness were calculated using Equation 4-4 [129]. Experimental density values were applied for the calculation. Also, to normalize the results, lead considered 100 percent heavy as the reference material. As Figure 4-11 shows, the density of developed nanocomposite is lower than that of the lead. The fabricated 5-layer nanocomposite achieves a transition rate of 11.2%, but with a density equal to 10.02% of the lead density.

Equation 4-4

$$\%\ heaviness = \frac{Density\ of\ samples}{Density\ of\ lead} \times 100$$

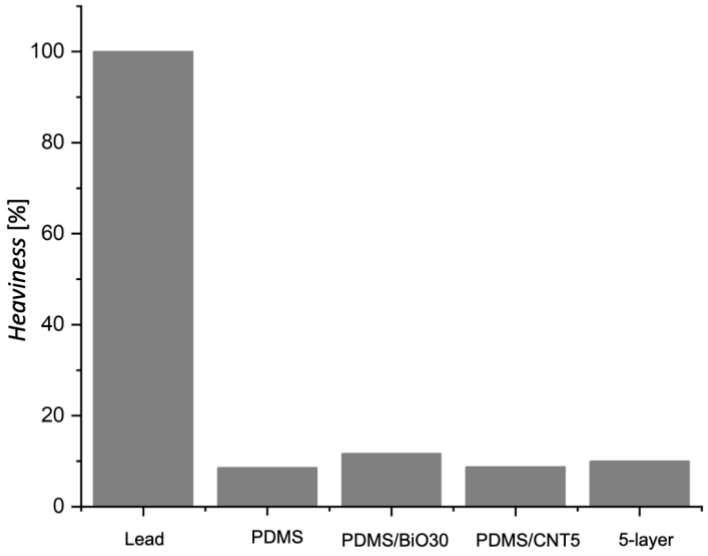

Figure 4-11. Percent heaviness of lead, PDMS, and the nanocomposites

4.3 Chapter Summary

New lead-free PDMS nanocomposites with various filler content were fabricated for x-ray shielding application. Bi_2O_3 with a higher x-ray absorption ability than pure lead (K-absorption edge 88 keV) and MWCNT were selected as nanofillers.

Structural studies showed that the well dispersed nanofillers can improve the tensile strength of the polymer matrix from 1.6 to 4.65 MPa. Also, adding a low amount of MWCNT could increase the tensile strength to 5.53 MPa, which was the result of the well dispersion, plus the outstanding inherent mechanical properties of MWCNT.

The experimental study indicated that the 1 mm thick nanocomposite containing 30 wt.% of Bi_2O_3 can only transmit up to 32% of x-ray with energy of 60 to 90 keV. Also, nanocomposites containing up to 10 wt.% MWCNT are not capable of shielding x-ray radiation with different energies between 60 to 90 keV. Therefore, to obtain low transmission rate, multilayer nanocomposites fabricated from separate Bi_2O_3 and MWCNT nanocomposite layers, containing the highest weight percentage (30 wt.%) of Bi_2O_3.

According to the result, the multilayer nanocomposite is an effective structure to decrease x-ray penetration. Increasing the layers numbers enhances the shielding efficiency in comparison with conventional nanocomposites, with higher tensile strength and elongation at break. The 5-layer nanocomposite, with a density of 1.29 g/cm^3, demonstrated shielding transmission rate to up to 11.2% for the x-ray with 60 to 90 keV energy. This result indicates the weight advantageous of layered nanocomposite over the lead and reveals the potential of these nanocomposites for wearable, lightweight, and lead-free x-ray shielding applications.

Chapter 5 Enhanced Electron Radiation Shielding Composite Developed by Well Dispersed Fillers in PDMS

Nowadays, high-energy electron beams are used for clinical applications in diagnosis and treatment of diseases, like cancer [120]. Despite the positive treatment effects, human exposure to high-energy electrons can mutate cells and result in serious health issues. In addition to clinical applications, but also in the aerospace industry, high-energy electron radiations in space present serious risks to astronauts' activities. In deep space missions, electron radiations with tens of MeV energies are threatening to the astronauts' health [145][146]. Therefore, it is necessary to protect individuals against high-energy electron radiations either on earth or in space. Commonly, metals like aluminum are applied for radiation shielding because of their low cost, excellent mechanical strength, and high thermal stability [104].

However, when the high-energy electron beam hits the metal shielding material, it can remove a valence electron and result in ionizing the metal molecules to produce secondary electron radiations. The bremsstrahlung photons are another radiation that is produced as the result of inelastic collisions of electron beam with the nucleus of aluminum atoms [147]. The production of these radiations has limited the application of aluminum for electron shielding. Furthermore, an increase in electron energy will require more material to attenuate the electron beam, which, in turn, contribute to heavier shielding structures. However, increasing the weight of shielding structures is not favourable for any applications, especially for the space industry as it leads to heavier payload, more fuel consumption, and increases the mission cost. All of which can adversely affect the feasibility of the missions [104]. Thus, the development of novel radiation shielding materials that are lightweight and provide the necessary shielding effectiveness is important [76].

A promising way to produce lightweight shielding material with sufficient attenuation is utilizing polymer reinforced composites [45]. Polymers are usually composed of low-Z elements (such as hydrogen and carbon) and have weight advantages in comparison with metallic shielding materials. Moreover, low-Z elements are less likely to produce secondary electrons and photons due to their high electron density [45][148]. Polyethylene (PE), poly (methyl methacrylate) (PMMA) [104], high-density polyethylene (HDPE) [62], epoxy, and polydimethylsiloxane (PDMS) [149] are examples of polymers for shielding several types of radiations [75][77][150][151]. However, the application of polymer for radiation shielding needs to be evaluated more, since there are still polymers that have not been studied for high-energy electron beam shielding applications so far.

In addition, shrinking the size of effective metals and dispersing them in a polymer matrix, have shown considerable enhancement in shielding efficiency of polymers [18][42]. For example, bismuth oxide (Bi_2O_3) is one of the reported materials for shielding photons energy ranging from 40-100 keV [152][153]. Bi_2O_3 with key features like nontoxicity, high radiation absorption (K-absorption edge 90.5 keV), and low cost have shown promising results in photon attenuation [128][129]. In addition to high atomic number fillers, low-Z fillers such as carbon-based nanomaterials have been evaluated for radiation shielding applications [18][94][154]. For instance, MWCNT can form cross-linking sites between polymer chains and hinder effect under electron beam irradiation. So the nanotube can enhance the tensile strength of polymer matrix, along with the thermal stability [155].

In this chapter, PDMS polymer nanocomposite is reported for high energy electron beam shielding, with weight advantages and higher attenuation efficiency in comparison with aluminum. Bismuth nanoparticles and carbon nanotubes were dispersed in PDMS (either all together; PDMS/CNT/BiO, or separately: PDMS/CNT and PDMS/BiO) and formed the shielding materials (Figure 5-2A) applied in this study. The chemical composition, mechanical strength, and thermal stability were evaluated. Electron beam shielding performance of developed composites were also assessed under electron beam energies of 9, 12, 16, and 20 MeV (similar energy to those applied for cancer treatment, and the reported electron beam energies for outer space such as) in attenuation mode and were compared to aluminum as the reference material.

5.1 Materials and Method

5.1.1 Fabrication Method

To fabricate pure PDMS and the PDMS nanocomposites, first PDMS was prepared by mixing the base polymer and the curing agent with a 10:1 weight ratio. As Table 5-1 reveals, 30 wt.% of Bi_2O_3 and 3 wt.% MWCNT was applied to fabricate PDMS/BiO, PDMS/CNT, and PDMS/CNT/BiO nanocomposites. Nanofillers were dispersed in liquid polymer using mechanical stirring (VWR hotplate stirrer) at 1500 rpm for 2 hours. The mixtures were then vacuumed for 30 seconds to release the trapped air bubbles during the mixing process. Finally, the prepared compounds were moved to 2-inch petri dishes as molds and baked in the oven at 70°C for 3 h with 20 MPa pressure. Each nanocomposite was fabricated with 5 different areal densities: 0.5, 1, 1.5, 3, and 5 g/cm^2.

Table 5-1. Chemical composition of different samples

Filler type	Filler wt.%	PDMS wt.%	Sample designated code
No filler	0	100	PDMS
Bi_2O_3	30	70	PDMS/BiO
MWCNT	3	97	PDMS/CNT
Bi_2O_3	30	67	PDMS/CNT/BiO
MWCNT	3		

5.1.2 Characterization

To evaluate the chemical bindings in the nanocomposite, x-ray diffraction (XRD) (Bruker, tensor 27) (2-theta between 7 to 90°) and X-ray photoelectron spectroscopy (XPS) (VJ ESCALAB 250) were performed.

The mechanical properties of nanocomposites were measured by Instron 5548 Micro Tester, according to the ASTM D412, with a 10 kN load cell and 50 mm/min crosshead speed. To prepare the samples with the required shape and dimensions, a laser engraving system was applied.

Nanofillers dispersion was evaluated by Zeiss Ultra plus scanning electron microscopy (SEM) and Energy-dispersive X-ray spectroscopy (EDX), plus the changes in the microstructure of nanocomposite before and after electron-beam irradiation. Small pieces of samples were cut and mounted on aluminum stubs by double-sided carbon tapes. Then samples were coated with a thin layer of gold, using Gold Sputter coater, to make them electrically conductive.

The thermal stability and thermal degradation behavior of all samples were analyzed via Thermogravimetric Analysis (TGA) tests, using TA instrument Q500 model equipment. The test temperature was ranging from 20 °C to 800 °C and a heating rate of 20 °C/min in nitrogen atmosphere. In addition, the heat transfer of different samples was visualized and compared using Hti-Xintai Thermal Imaging Camera. Samples were cut into the same diminutions, (1 cm width, 1 cm length, and 2mm thickness) and placed on an isothermal hot plate with a constant temperature of 70 °C.

5.1.3 Electron-beam attenuation test

To evaluate the electron shielding efficiency of samples, Varian TruBeam Linac (Varian Medical Systems, Palo Alto, CA, USA) machine at Grand River Regional Cancer Centre (GRRCC) (Kitchener, ON, Canada) was used. Figure 5-1 shows the digital image of the electron-beam generator and a schematic of the irradiation test setup. All the samples were studied for the electron-beam attenuation using 9, 12, 16, and 20 MeV energies. Also, a dose of 100 monitor unit (MU) was delivered to each sample with 1000 MU/min dose rate.

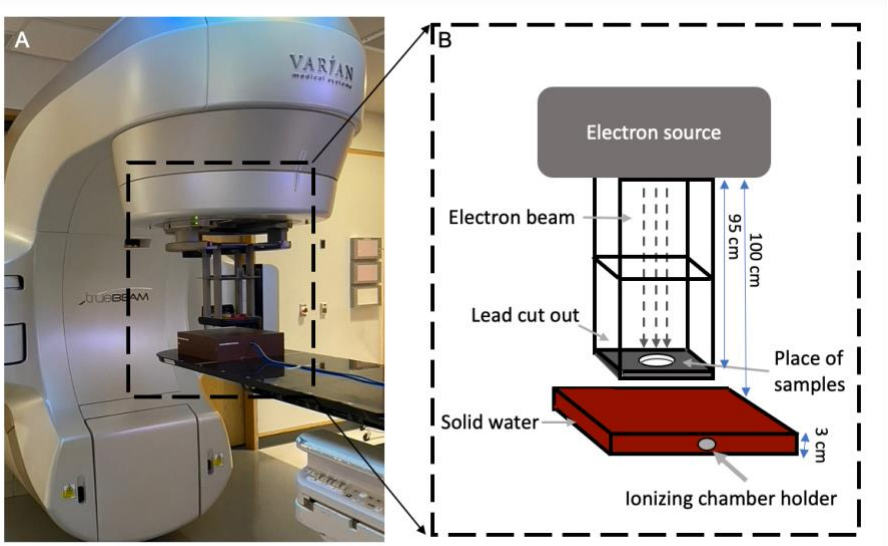

Figure 5-1. (A) Varian TruBeam Linac machine with electron-beam attenuation test setup; (B) Schematic of the test setup.

As Figure 5-1b shows, samples were placed on top of the electron cone applicator with a dimension of 6×6 cm^2, and 3 cm diameter lead cut-out insert. The distance between the electron cone and the electron source/target was 95 cm as shown in the schematic. Also, the transmitted electrons through the samples were measured using an ionization chamber (Farmer chamber) which was placed in a solid water phantom, at 100 cm from the electron target. In the first step, the ion chamber is directly irradiated by an electron beam (without the sample in place) to measure the baseline reading (I_0). Then, the ion chamber reading with samples in place was taken (I_t), for each sample. Each sample was irradiated twice to confirm the consistency. The percentage of electron Attenuation Efficiency (AE%) of each sample calculated by Equation 5-1 [121]:

Equation 5-1

$$AE(\%) = ((I_0 - I_t)/I_0) \times 100\%$$

In this study, to compare the weight of developed nanocomposites with that of the aluminum as the reference material, the attenuation results were plotted as a function of areal density (AD). The areal density of samples was calculated using Equation **5-2**:

Equation 5-2

$$AD = \rho \times t$$

Where ρ and t represent the density and the thickness of shielding materials, respectively. Each nanocomposite where fabricated with five different areal densities (0.50, 1.00, 1.50, 3.00, and 5.00 g/cm^2). Therefore, transmission characteristics of each sample were measured using four electron-beam energies (9, 12, 16, and 20 MeV). At the same electron attenuation efficiency percentage (AE%), weight advantages of samples over Al can be calculated following Equation 5-3:

Equation 5-3

$$\text{weight advantages } (\%) = ((\text{AD}_{\,aluminum} - \text{AD}_{\,\text{sample}})/\text{AD}_{\,\text{aluminum}}) \times 100\%$$

5.2 Result and discussion

The digital images of pure PDMS and the nanocomposites is shown in Figure 5-2A. To investigate the chemical composition of each sample, XRD was performed (Figure 5-2B). The XRD pattern of pure PDMS exhibits the typical amorphous peaks at about 12° and 20°. However, the intensity of both peaks decreases by adding MWCNT in PDMS/CNT sample. This result can be attributed to the formation of amorphous phases in this nanocomposite, since the dispersed MWCNT cross-links with polymer chains and decreases the chain order [156][157]. Moreover, in both PDMS/BiO and PDMS/CNT/BiO samples, XRD peaks confirm the formation of bismuth silicate and shows the successful Bi_2O_3 bonding with the silicon (Si) in polymer matrix, as is marked in Figure 5-2B [158]. Therefore, XRD patterns confirm the nanofillers incorporation with polymer matrix. Figure 5-2C shows a drawing of PDMS/CNT/BiO sample that indicates how nanofillers are distributed in polymer matrix.

To further investigate the available bindings, the XPS was performed for PDMS/CNT/BiO nanocomposite (Figure 5-2 D1 and D2). In the C1s core-level peaks (Figure 5-2 D1), the intense peak at 284.4 eV corresponds to C-C bonding and agrees with literature. The 286.2 eV binding energy is assigned to C-O bonding which can be attributed to COOH functional groups on MWCNTs [159]. Three peaks appear for Si 1s core-level (Figure 5-2 D2), where 99 eV, and 101

eV peaks correspond to Si-O, and Si-C, respectively. The peak at 103 eV shows SiO_2 bindings which can be because of interaction with either functional groups in MWCNT or the oxygen in Bi_2O_3 particles [160].

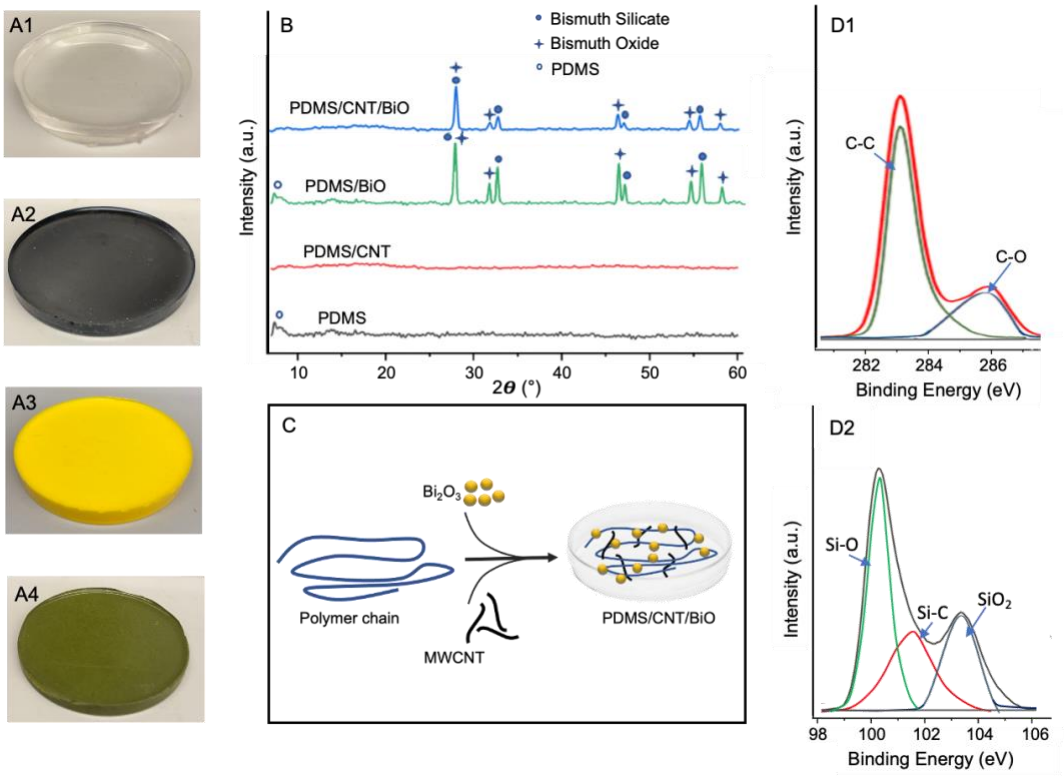

Figure 5-2. (A) Digital images of pure polymer (A1), PDMS/CNT (A2), PDMS/BiO (A3), and PDMS/CNT/BiO (A4) samples; (B) XRD pattern of all samples; (C) schematic of nanofillers distribution in polymer matrix; and (D) XPS spectra of (D1) C 1s and (D2) Si 1s in PDMS/CNT/BiO sample.

Rather than chemical binding between the nanofiller and matrix, properties of nanocomposite can be affected by the nanofillers dispersion quality. Especially in the case of electron shielding, the state of fillers determines the extent of shielding. In addition, poor nanofiller dispersion induces the nano and micro defects inside the nanocomposite and decreases the mechanical strength of final sample. Therefore, the dispersion quality of nanofillers was characterized through electron

microscopy. Figure 5-3A shows the SEM image of PDMS/CNT/BiO nanocomposite along with the EDX characterization result. The spherical particles represent Bi_2O_3 nanofillers which are uniformly distributed in polymer matrix. The individual bright nanotubes are well dispersed MWCNTs, with no sign of aggregation. The elemental composition was confirmed by EDX characterization as shown in Figure 5-3A, which reveals the presence of high-Z elements (Si and Bi) in addition to low-Z elements (O and C) in the polymer matrix.

Well dispersed nanofillers in polymer matrix helps the mechanical properties improvement by uniform stress distribution through the sample and efficient load transfer to the nanofillers. As Figure 5-3B exhibits, the addition of nanofillers enhances the mechanical strength of polymer matrix. The PDMS/ MWCNT nanocomposite has the highest tensile strength and fracture strain, according to the MWCNT interaction with the polymer matrix and exceptionally large aspect ratio.

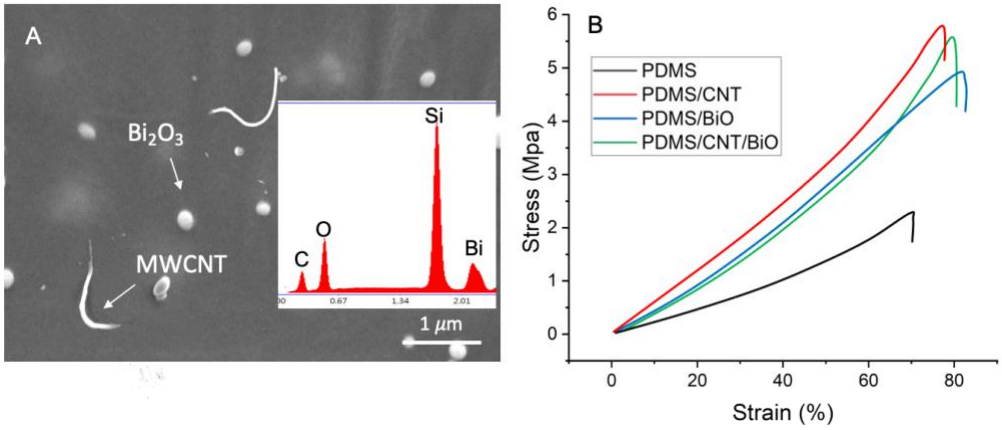

Figure 5-3. (A) SEM image of the cross-section PDMS/CNT/BiO sample including the EDX result; (B) Stress-strain diagram of pure PDMS and the nanocomposites

Besides, thermal stability of nanocomposites was evaluated by TGA analysis. Figure 5-4A shows the weight changes of samples with increasing the temperature up to 800 °C. Compared with pure PDMS, the addition of 3 wt.% MWCNT increases the thermal stability with restraining the degradation of PDMS polymer chains during the pyrolysis and increasing the initial decomposition temperature for about 8% (from 315°C to 340°C). Also, the addition of Bi_2O_3 displays significant improvement in thermal stability with initial decomposition temperature of 21% higher than that of pure PDMS, which is resulted by the high thermal stability of the well dispersed Bi_2O_3

nanoparticles. Composite containing both Bi_2O_3 and MWCNT exhibits the highest thermal stability with 30% improvement in initial decomposition temperature in comparison with pure PDMS, and increasing it to 415 °C. It should be noted that, the nanofillers can improve thermal stability of polymer matrix by slowing down and hindering the diffusion of volatile decomposition products [161].

As shown in Figure 5-4A, the initial decomposition temperature of nanocomposite after electron-beam irradiation is about the same as non-irradiated samples and indicates that samples maintain their thermal properties after electron beam irradiation.

Furthermore, with increasing the temperature to 670 °C, about 5 wt.% of residual material of PDMS was found. For PDMS/CNT, PDMS/BiO, and PDMS/CNT/BiO, about 9 wt.%, 34 wt.%, and 41 wt.% material was remained, respectively. The remaining weight of the nanocomposites could be attributed to the nanomaterials (Bi_2O_3 and MWCNT) with high heat resistant.

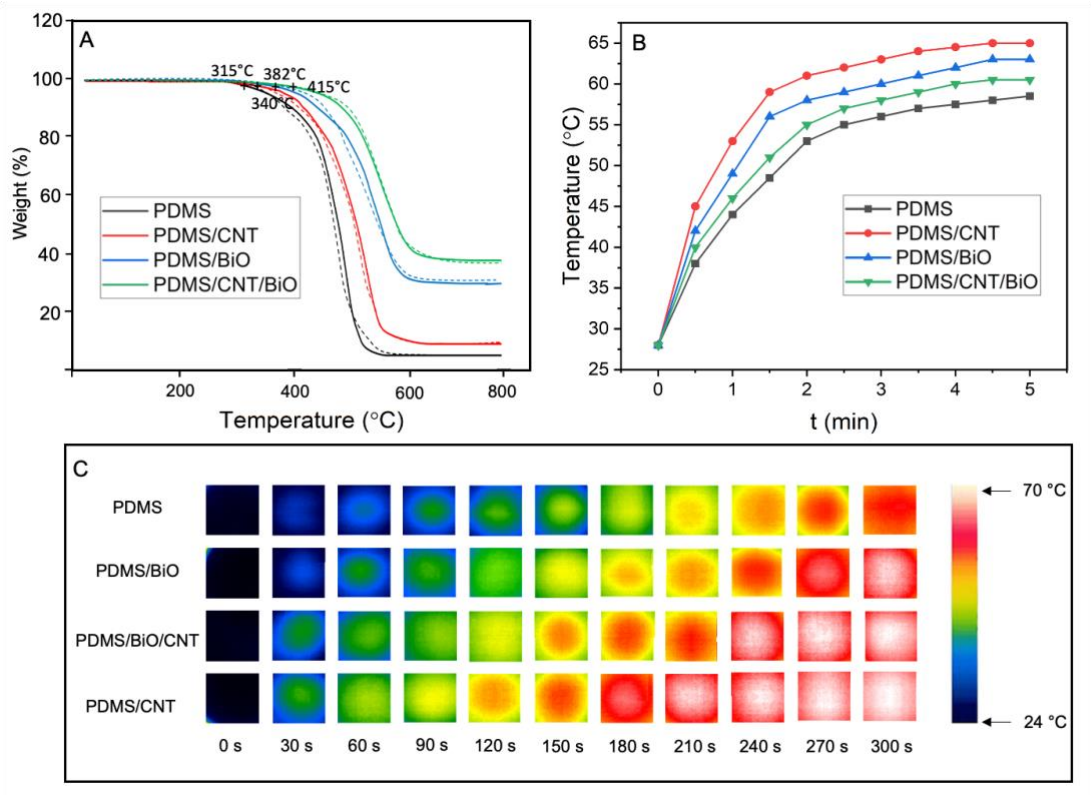

Figure 5-4. (A) TGA test results of all samples before (solid line) and after (dashed line) electron beam irradiation; (B) Surface temperature changes of all samples at different moments of heating process; (C)

Infrared thermal images of samples at different heating time.

To evaluate and visualize the effect of fillers type and fillers content on thermal conductivity, an infrared camera was utilized to record the temperature of the upper surface of samples on a heating plate. Samples were placed on an isothermal hot plate with a constant temperature of 70 °C, for 300 s (5 min). The corresponding curves of the temperature at the upper surface of samples as a function of heating time are shown in Figure 5-4B. The slope of each line reflects the rate of the temperature change. For example, the upper surface temperature of PDMS sample took 150 s to reach 55 °C, which was 2.5 times longer than that of the PDMS/CNT sample. In addition, as Figure 5-4C shows, the surface color of pure polymer and all composites was dark blue at the first moment of the heating process, corresponding to the room temperature (24 °C). Each color represents specific temperature: dark blue room temperature, green 50 °C, yellow 55 °C, red 60 °C, and white 65 °C. With increasing the temperature of samples, the surface color changes to green, yellow, red, and finally the whitish red at different rates, indicating that the temperature of samples changes at various rates. According to Figure 5-4C, the surface temperature of the PDMS/CNT composite is higher than the pure PDMS and other composite at any time, as a result of the high thermal conductivity of well-dispersed MWCNT [103].

5.3 Electron Shielding Measurement

The Attenuation Efficiency (AE%) of pure polymer, nanocomposites, and aluminum for each of the four energies (9, 12, 16, and 20 MeV) were calculated using Equation 5-1. Results are plotted as shown in Figure 5-5. According to the figure, the AE% for all the samples increases with increasing the areal density.

The overall trend of AE% of samples is similar for all energies. According to the results, the nanocomposites have better shielding properties than the pure polymer (PDMS). In addition, with increasing the electron energies from 9 MeV to 20 MeV (Figure 5-5A to D), the AE% decreases for each sample, meaning that more materials of each sample are needed to attenuate the electron beam.

As the results exhibit, both PDMS/BiO and PDMS/CNT/BiO nanocomposites perform better shielding efficiency than aluminum for any given areal densities. For example, at areal density of

1.5 g/cm^2, aluminum attenuates about 80% of electron beam with 16 MeV energy. This number increases to 90% for PDMS/CNT/BiO with the same areal density under the electron beam energy (Figure 5-5c).

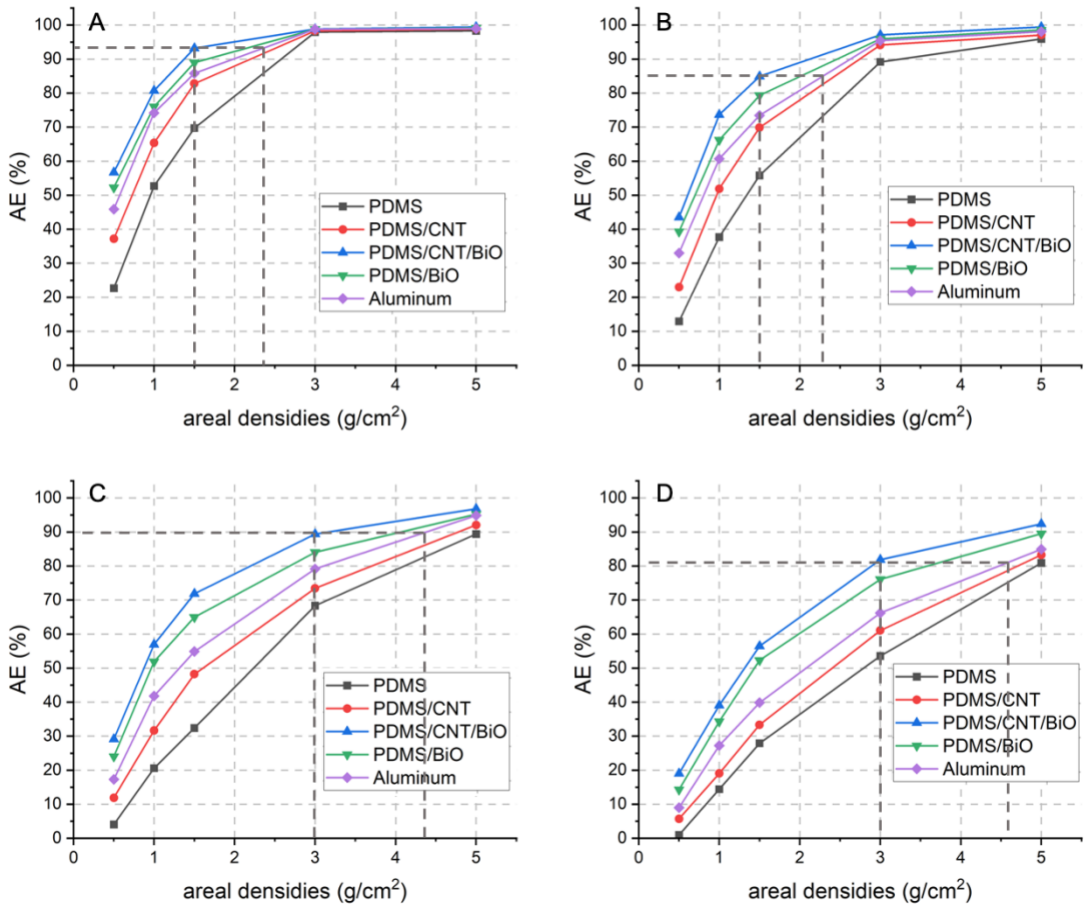

Figure 5-5. Percentage attenuation efficiency (AE%) of all samples at (A) 9 MeV, (B) 12 MeV, (C) 16 MeV, (D) 20 MeV.

Furthermore, Figure 5-5 shows that less amount of PDMS/BiO and PDMS/CNT/BiO nanocomposite is required to obtain equivalent AE% in comparison with aluminum. For instance, as Figure 5-5a shows, to attenuate 93% of 9 MeV electron beam, aluminum with an areal density of about 2.5 g/cm^2 is required. This value decreases to 1.5 g/cm^2 for PDMS/CNT/BiO nanocomposite to attenuate the same amount electron beam with the same energy. This result indicates the weight advantage of developed nanocomposites over aluminum. Among the samples, PDMS/CNT/BiO shows the highest weight advantages and AE% at any electron beam energies.

The areal densities and AE% in which the maximum weight reduction of this sample happens, are highlighted in Figure 5-5. Therefore, at different electron beam energies, maximum weight reduction is calculated and summarized in Table 5-2, in addition to the areal density and AE% at the max weight reduction.

Table 5-2. A summary of weight advantage of PDMS/CNT/BiO with respect to Al for all electron energies

Electron energy (MeV)	Maximum weight reduction (%)	Areal density of nanocomposite at the max weight reduction (g/cm^2)	Attenuation at the max weight reduction (%)
9	36.1	1.5	93.17
12	34.7	1.5	84.9
16	31.03	3	90
20	34.7	3	81

Besides, all samples reach to a maximum AE% of 98% for 9 MeV electron beam, at areal density of 3 g/cm^2 and above (Figure 5-5a). Herein, 3 g/cm^2 areal density is considered as the saturation areal density at 9 MeV electron beam, which means increasing the areal density over this value will no longer enhance the AE%. This phenomenon is also observed with electron energies of 12, 16, and 20 MeV (Figure 5-5b and 2c). This is due to the Continuous Slowing Down Approximation (CSDA) ranges of samples. CSDA ranges approximate the average distance that a charged particle (electron in this study) can travel in the matter as it slows down to rest [162]. In this study, CSDA suggests that beyond the areal density of 3 g/cm^2, few existing primary 9 MeV electrons still contribute to the 2% unshielded radiations.

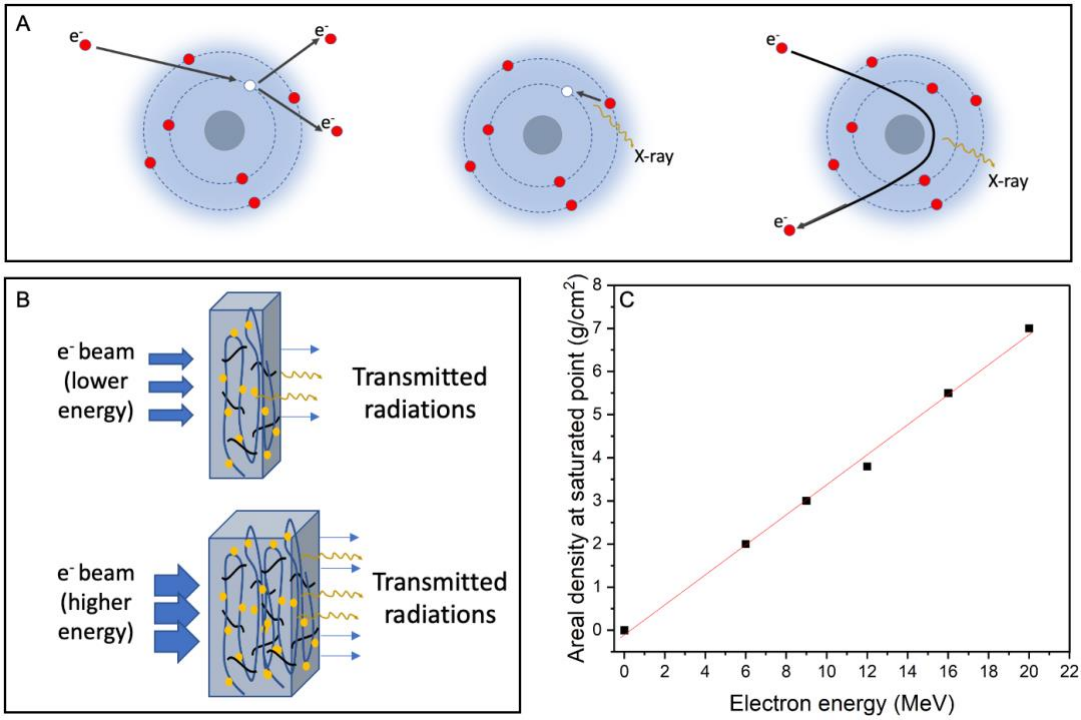

Figure 5-6. (A) A schematic of electron beam interaction with shielding material; (B) Increasing the secondary radiations when more material is using to stop the higher energy electrons; and (C) Linear fit of saturation areal density for all energies.

In addition, with increasing the primary electron radiation energy, the saturation areal density moves to higher values, however, the maximum AE% at saturation areal density decreases (Figure 5-5). This is due to the electron interaction with shielding material, as it is illustrated in Figure 5-6A. During the electron beam interaction with the atoms of shielding material, high-energy electrons can hit and remove a valence electron and produce the secondary electron radiations. The bremsstrahlung photons are another radiation that is produced either when outer shell electron fills the inner shell electron vacancies, or as the result of electron beam inelastic collisions with the nucleus of atoms. When more shielding materials are used to stop the higher energy electrons, greater quantity of secondary radiations (like x-ray) can be generated (Figure 5-6B). Therefore, the AE% would be lower at saturation areal density for electron beams with higher energies.

The areal density at the saturation point as a function of the electron energy is illustrated in Figure 5-6C. The plot indicates that with increasing the primary electron beam energy, more material is needed to reach the saturation point of areal density. In addition, there is a linear relationship

between saturation areal density and the electron beam energy, which can help to estimate the areal densities at the saturation point for higher electron energies. This helps with designing shielding material against the highest electron beam energy than what we have presented in this article.

Finally, the AE% of PDMS/CNT/BiO nanocomposite and aluminum is visualized in Figure 5-7 for more comparison. As Figure 5-7 shows, the AE% of both materials increases with increasing the areal density, however, PDMS/CNT/BiO has higher AE% than aluminum all the time. The difference between the attenuation values decreases for higher areal densities, but in the areal density of 0.5, 1, and 1.5 g/cm^2, the nanocomposite attenuates more electron beam than aluminum.

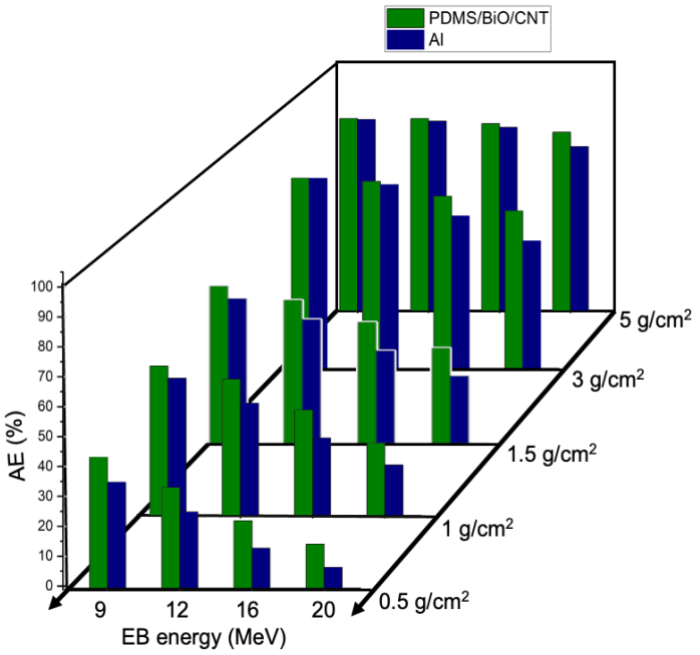

Figure 5-7. AE% of PDMS/CNT/BiO (green column) composite and Al (navy column) as a function of energy at different areal densities

5.4 Chapter Summary

To protect astronauts from electron radiations, metallic materials like aluminum constructed units are in use. However, application of aluminum results inkey issuess such as heavy weight and generation of secondary electron. As such, the development of innovative lightweight shielding

materials is ofsignificant importancee. The lightweight radiation shield presented in this paper demonstrates that MWCNT and Bi_2O_3 hybrid nanocomposites are capable to attenuate more than 70% of electron beams with energies ranging from 9 to 20 MeV. The nanocomposites have an average weight advantage of about 34% in comparison with aluminum. However, when above a saturation point, the areal density of nanocomposites has no additional weight advantage. Furthermore, the change in saturation point of shielding materials changes linearly with increasing electron beam energy.

The characterization results indicate that the thermal stability of pure PDMS was improved by homogenously dispersing MWCNT and Bi_2O_3 nanoparticles for about 30 %. Based on the TGA results, no sign of distortions was found in samples after the electron beam irradiation. Additionally, MWCNT was found to be greatly effective in increasing the rate of heat flow. In terms of mechanical strength, nanocomposite filled with MWCNT and Bi_2O_3 exhibited a tensile strength as high as 3.7 MPa, which is about twice bigger than that of the pure PDMS. However, the mechanical strength is still smaller that of Al. So, in conclusion, the developed nanocomposite can is suggested to be use as part of the radiation shielding material with Al or other structural materials for shielding structures in space applications.

Chapter 6 Multilayer Design Fabrication and Characterization for Space Radiation Shielding Application

Radiation shielding technology has been developing for several decades and has opened many opportunities for humans to explore the expansive universe. In recent years, the conditions for undertaking long space journeys, such as the Mars space missions, have been observed. Requirements for such trips are higher payload, space radiation shielding and more astronauts in the spacecrafts. Conventional radiation shielding materials, such as Al, HDPE, and water, can barely support this type of missions due to the low ratio of shielding effectiveness and cost. One approach to reduce this cost is applying light-weight materials to replace heavily equipped radiation shields.

One of the current trends in modern space missions is applying multilayer design as shielding for extreme and complex hazardous space radiations that are difficult to shield by a single material. Each part of a multilayer structure should be able to associate with the other components in the structure, whilst accomplishing specific functions. This approach results in a multifunctional structure with excellent shielding efficiency, and thermal and mechanical properties for space applications.

Based on the previous study in previous chapter, PDMS/CNT/Bi_2O_3 nanoparticles, possesses 27%-37% weight advantage at 90% electron beam attenuation in comparison with Al. The advantages of nanocomposites vary for different electron energies. Additionally, the saturated attenuation points were introduced, which can be reached when real densities increase until minor electron beam attenuation advantage is achieved for all materials. However, high loading of Bi_2O_3 increases the chance of secondary radiation generation. In addition, adopting radiation shielding advantages of the different nanocomposites onto a single structure is expected to further improve overall

properties of the shielding materials. Therefore, a polymer-based multifunctional nanocomposite has been developed and described in this chapter.

6.2 Material and Methods

6.2.1 Fabrication prosses

The layer of PDMS polymers containing Bi_2O_3, MWCNT, MXene, and h-BN nanofillers were fabricated in three steps.

First surface treatment was required for uniform dispersion of nanofillers in the polymer matrix. In this regard, 50 mg/mL h-BN-water solution was placed in a sonication bath. The solution was moved to a cylindrical Teflon autoclave (h 70 mm, d 30 mm, wall thickness 3–4 mm, rated pressure 2–3 atm) afterward, and mixed with 9 mL hydrogen peroxide 30%. The solution was stirred for an hour. The prepared mixture was moved into the oven to be hydrothermally treated at 120 °C for 24 h. Figure 6-2A shows a schematic of the process. After 24 h, the powder dried out, however, the dried powder aggregates and so is difficult to disperse in the polymer matrix. Therefore, it was necessary to exfoliate the hydrogenated-BN (OHBN) powder in DI water by sonicating it for 1 hour. The solution was then filtered to remove water.

In the next step, three different mixtures were prepared by mixing the nanofillers directly into the PDMS polymer. Each mixture was to be applied as a single layer in the multilayer nanocomposite. Table 6-1. The prepared composites for different layers with various filler and polymer content, and the designated code to each sample shows the composition of each of these layers. A mechanical mixer was used for 2 hours to disperse the nano powder uniformly.

Table 6-1. The prepared composites for different layers with various filler and polymer content, and the designated code to each sample

Layer #	Sample designated code	PDMS wt.%	Filler type	Filler wt.%
First layer	PDMS/BN	80	OHBN	20
Second layer	PDMS/MXene	80	MXene (Ti_3C_2)	10
			MXene (Mo_2C)	10
Third layer	PDMS/CNT/BiO	65	Bi_2O_3	30
			MWCNT	5

Finally, the prepared mixtures were molded and baked into the desired shapes for shielding measurements. Figure 6-1A to C shows a schematic of the molding process. PDMS/CNT/BiO was the first layer to be molded. After baking it at 70 °C for 1 hour, the PDMS/MXene layer mixture was molded as the middle layer. The two layers were baked at 70 °C for another 1 hour before, adding the final layer, PDMS/BN. Finally, the three layers were baked together for two more hours to bake all the layers fully. It should be noted that we chose to bake each layer for an hour since at this time the mixture will become firm, but it would not be fully baked. After adding the other layer on top, the two layers do not mix, but they will stick together due to chemical bonding at the interface.

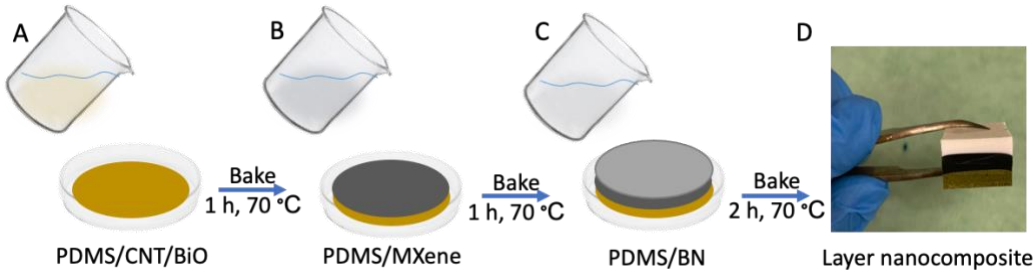

Figure 6-1. schematic of the fabrication process.

PDMS composites needs three hours of baking at 70 °C to cure completely. The step-by-step curing and molding of the layers result in good attachment in layers interfaces.

Five samples with areal densities of 0.5, 1, 1.5, 3, and 5 g/cm^2 were fabricated in this way. The portion of layers was kept equal in all areal densities. For example, the layered nanocomposite with a 1.5 g/cm^2 areal density was composed of three layers, each layer with an areal density of 0.5 g/cm^2. Figure 6-1D shows the cross-section of 1.5 g/cm^2 layer nanocomposite, which is composed of three layers: PDMS/BN (the white layer), PDMS/MXene (the black layer), and PDMS/CNT/BiO (the dark-green layer).

On top of fabricating a multilayer structure, one-layer nanocomposites of each of the PDMS/BN, PDMS/MXene, and PDMS/CNT/BiO were fabricated with an areal density of 1 g/cm^2, to compare directly with the multilayered structure.

6.2.2 Characterizations

To evaluate the chemical bindings in the nanocomposites, XPS characterization method was performed. Nanofillers dispersion was evaluated by SEM and EDX. Also, TGA analysis was conducted to characterize the thermal stability and thermal degradation behavior of all samples

DSC was performed on Q2000 from TA instruments to measure the working temperature. The heat flow change versus temperature change ranging from -90 °C to 210 °C was recorded. The temperature of the whole measurement process was first increased from 25 °C to 210 °C with a rate of 10 °C min^{-1} and then decreased from 210 °C to -90 °C with a rate of 5 °C min^{-1}, then increased from -90 °C to 210 °C. In addition, the heat transfer between different samples was visualized and compared using Hti-Xintai Thermal Imaging Camera. Electron attenuation measurements were performed in Grand River Hospital, as explained previously in section 5.1.3.

6.3 Result and discussion

6.3.1 Chemical composition analysis

To evaluate the successful treatment of h-BN powder, the chemical bonds before and after hydrothermal treatment were evaluated by FTIR spectroscopy. As can be seen from Figure 6-2B, the main vibrations of h-BN are at around about 759 and 1323 cm^{-1} which can be attributed to the in-plane B–N stretching and B–N–B out-of-plane bending vibration, respectively [163]. The sharp

peak at approximately 3236 cm^{-1} indicates the percent of more OH groups of boric acid [164]. The appearance of the B–OH stretching vibrations suggests successful functionalization. Furthermore, the small vibration band at 1200 cm^{-1} could indicate the presence of the B-OH in-plane bending, and the peak at about 890 cm^{-1} shows the B−OH out-of-plane bending [165].

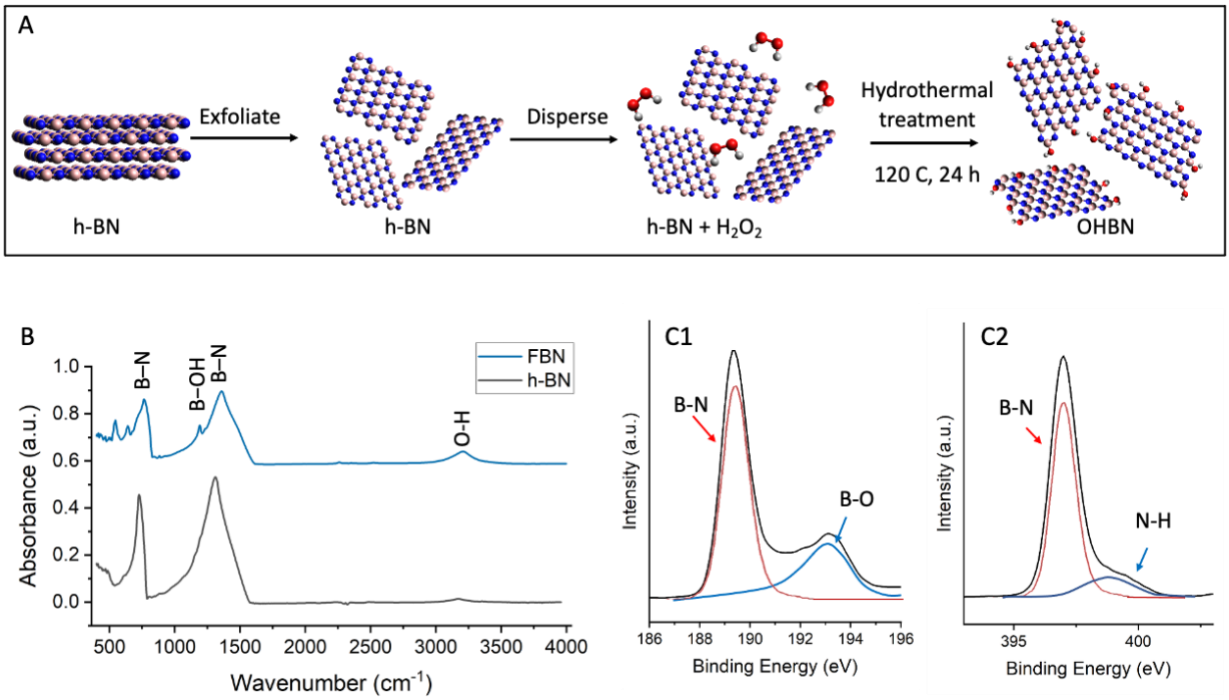

Figure 6-2. (A) The schematic of h-BN hydrothermal treatment, (B) FTIR spectrum of h-BN before and after hydrothermal process, and XPS results of (C1) the B 1s and (C2) N 1s core levels.

To further investigate the available bindings, the XPS was performed (Figure 6-2C) to explain the elemental composition, functional groups, and bonding nature of compounds. The Gaussian–Lorentzian function of Origin Pro® was used to plot the fitting curves of nanomaterials and composites. In the B1s core-level peaks (Figure 6-2 C1), 190.3 eV and 191.1 eV peaks correspond to B-N and B-O, respectively [159]. Two peaks appear for N 1s core-level (Figure 6-2 C2), where the intense peak at 397.9 eV corresponds to B-N bonding and agrees with the literature. The peak at 399 eV binding energy is assigned to N-H bonding which can be attributed to OH functional groups [166][167][116].

In addition, the XPS result of PDMS/BN nanocomposite reveals the SiO_2 presence. Figure 6-3 shows the Si 1s core-level of PDMS polymer before (A) and after (B) mixing with hydrogenated

BN (OHBN). According to Figure 6-3, the oxygen functional groups in OHBN can bond with Si elements in PDMS, which means the OHBN nanopowder is successfully embedded in the polymer matrix.

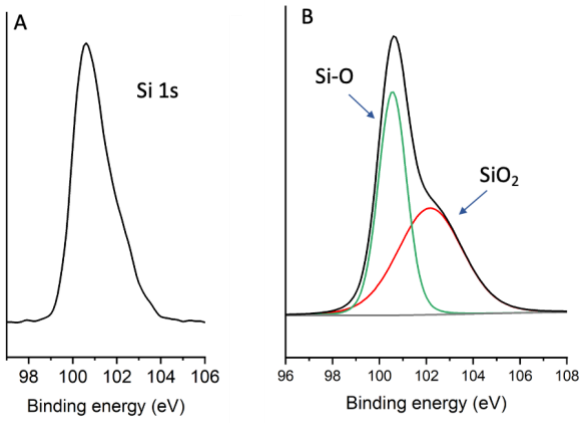

Figure 6-3. Si 1s peak of (A) pure PDMS, and (B) PDMS/BN nanocomposite.

The XPS was performed for PDMS/MXene nanocomposite too. The fitting curves shown in Figure 6-4 give various information about the bonding nature and functional groups of MXene and the composite sample. The peaks of Si 1s at 104 eV is due to the bonding with functional groups in MXene (Figure 6-4A). The oxygen functional group gives rise to the Ti 2p peaks at 455 and 464 eV (B). The C–Ti, C–C, and Mo-C peaks of C 1s confirms the presence of the Ti and Mo and their bonding with C (Figure 6-4C).

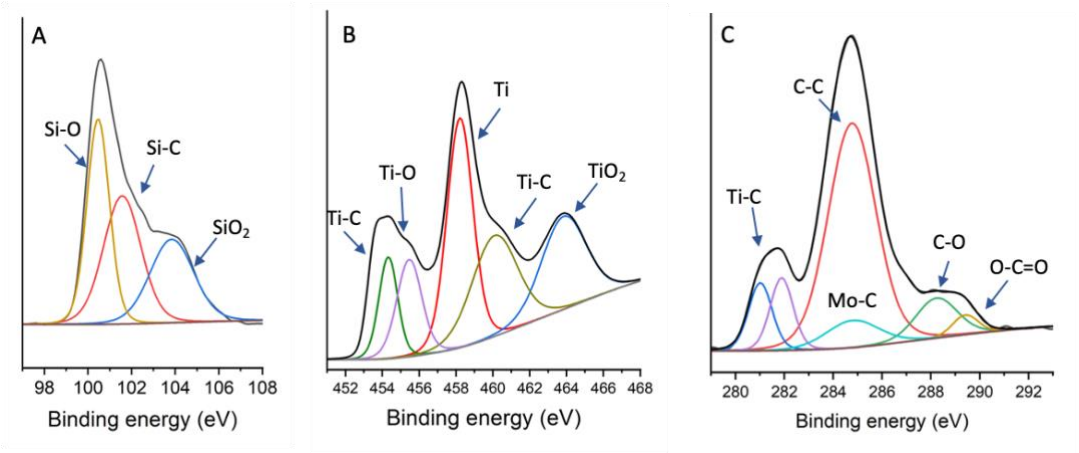

Figure 6-4. XPS result of PDMS/MXene nanocomposite, the Si 1s (A), Ti 2p (B), and C 1s (C).

6.3.2 Microstructure evaluation

The dispersion quality of nanofillers can be seen in cross-section SEM images. According to fillers size (<1um), the SEM images were taken in high magnification to confirm the well dispersion of nanofillers. Figure 6-5 shows the SEM images of PDMS/BN and PDMS/MXene layers, separately. As Figure 6-5 shows, no aggregated areas were detected in the samples. Also, the EDAX spectrum performed to confirm the purity of prepared samples.

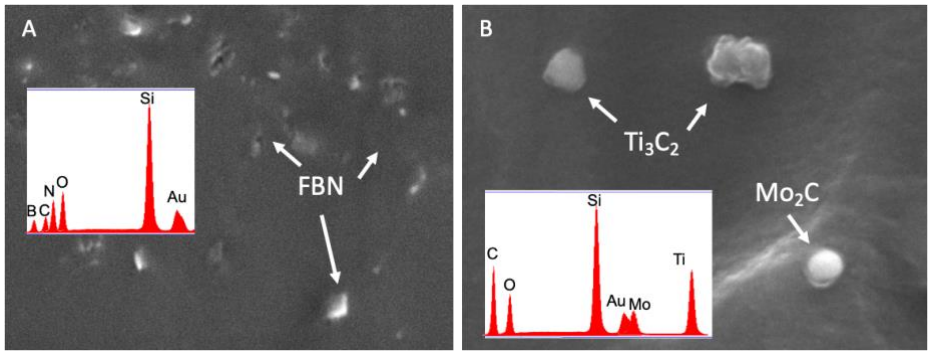

Figure 6-5. SEM images of (A) PDMS/BN and (B) PDMS/MXene nanocomposite, including the EDAX results.

EDAX and elemental mapping were performed to further confirm the composition and the homogeneous distribution of elements in the nanocomposite layers, especially in the interfaces of layers area. Figure 6-5 shows the EDAX spectrum of PDMS/BN – PDMS/MXene interface. The presence of B and N in PDMS/BN layer can be observed. Also, the Figure 6-5 shows Ti and Mo distribution through the PDMS/MXene layer. It is evident from the Figure 6-5 that OHBN, Ti_3C_2 and Mo_2C are homogeneously distributed in different layers. Elemental mapping also further indicates the well attached layers at interface as for example the B and N elements are defused for a few microns PDMS/BN layer into the PDMS/MXene layer.

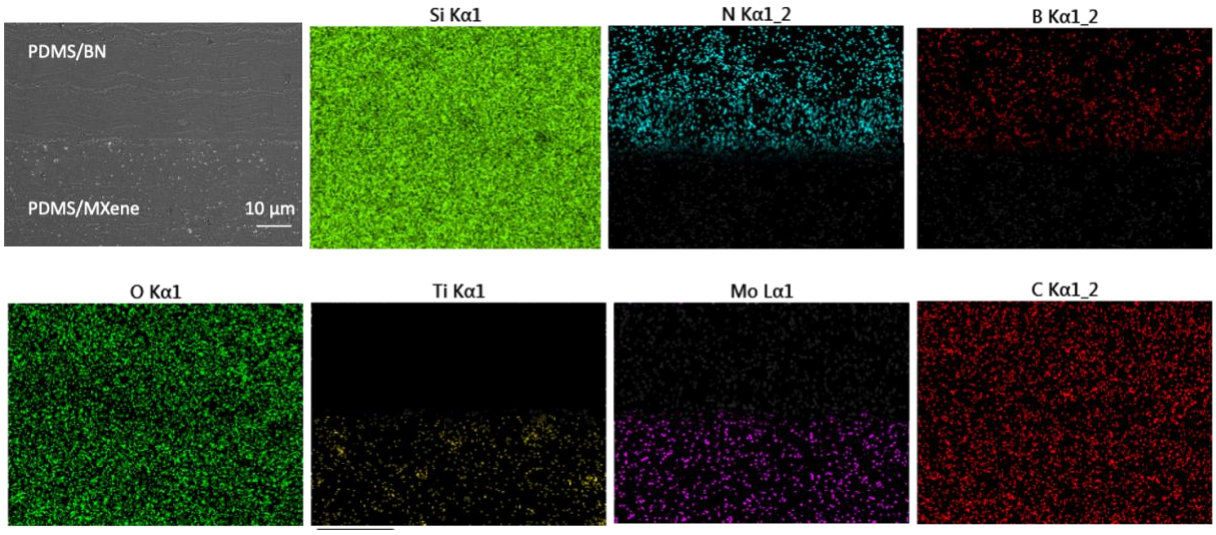

Figure 6-6. SEM image of PDMS/BN and PDMS/MXene interface in layer nanocomposite, and the elemental mapping analysis.

The EDAX was performed at PDMS/MXene – PDMS/CNT/BiO interface, too. Figure 6-7 indicates the the presence of Bi in PDMS/CNT/BiO layer, and Ti and Mo distribution through the PDMS/MXene layer. It is evident from the Figure 6-7 that Bi_2O_3, Ti_3C_2 and Mo_2C are homogeneously distributed in different layers. In addition, the well attached layers at interface can be confirmed, since the elements are defused for a few microns from one layer into the other layer, such as Mo, as Figure 6-7 exhibits.

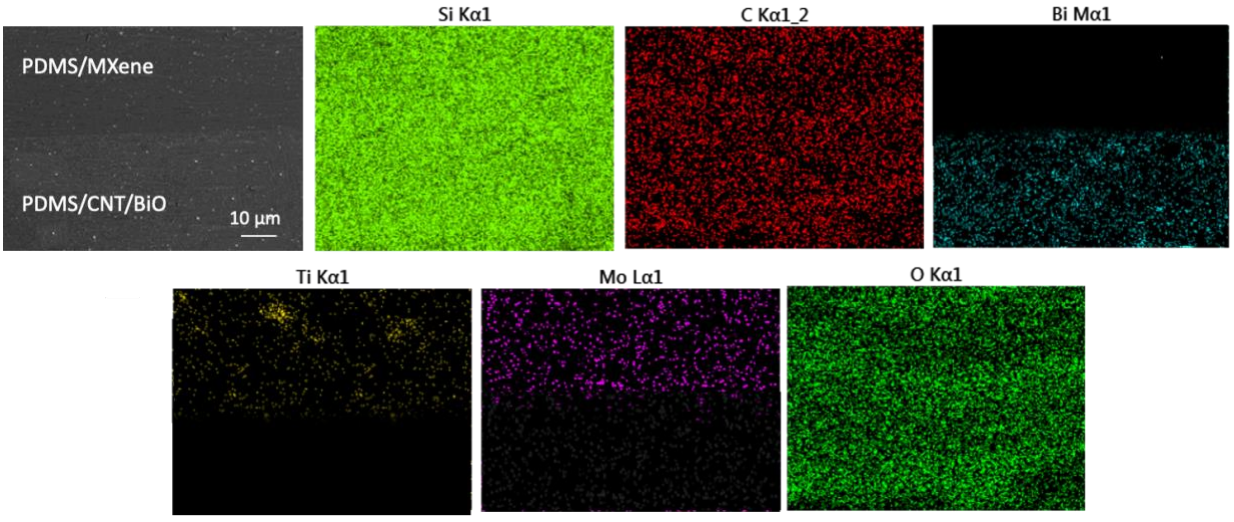

Figure 6-7. SEM image of PDMS/MXene and PDMS/CNT/BiO interface in layer nanocomposite, and the

elemental mapping analysis.

6.3.3 Thermal properties

The thermal stability of the layer nanocomposite depends on the thermal behaviour of each layer. So, layers were heated up separately by TGA analysis and evaluated for compared to the pure PDMS, as shown in Figure 6-8A. PDMS decomposition begins at 315 °C and continues until 560 °C, resulting in the final weight loss of about 90 wt.%. However, by adding OHBN filler, the decomposition temperature of PDMS/BN nanocomposite raises to 388 °C, at filler contents of 20 wt.%. The sample degradation finishes at about 600 °C with 54 wt.% weight loss which is due to the high thermal stability of OHBN filler. Also, adding MXene to PDMS changes the thermal stability with slowing down the decomposition of nanocomposite. As Figure 6-8A shows, the PDMS/MXene shows the slowest decomposition rate, as the degradation of this layer starts at 325 °C but continues until 600 °C. The weight loss of PDMS/MXene sample decreases to 38 wt.% which is a considerable difference. As Figure 6-8A shows, PDMS/CNT/BiO layer has the highest thermal stability with initial decomposition temperature of 415 °C. According to Figure 6-8A all the layers are stable up to 325 °C.

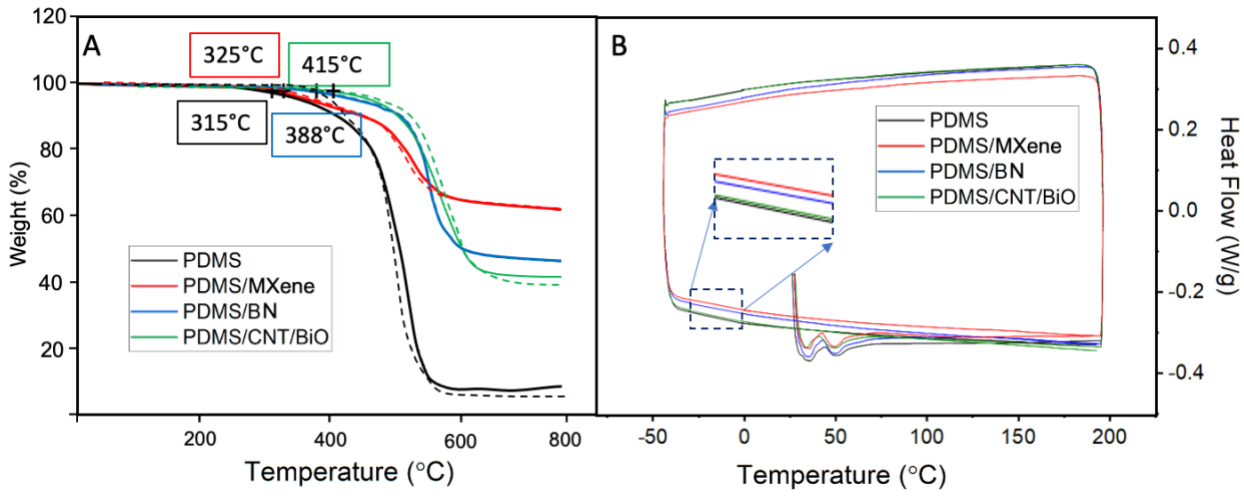

Figure 6-8. (A) TGA and (B) DSC test results of all samples. Percentage of weight loss (%) and heat flow

are plotted as a function of temperature.

DSC data of each layer materials are shown in Figure 6-8B. Upon heating up all the samples show an exothermic peak at around 20 to 40 °C which disappears in second round of heating up and can be due to the trapped gas during the sample preparation. Generally, in DSC results any signal and changes during the heating or cooling process can show phase changes in material such as melting. However, no peaks can be observed in second round of heating process (Figure 6-8B), which indicates the samples stability in -40 to 190 °C temperature range. Therefore, all samples show a working temperature range of -40 to 190 °C which is ideal for space applications. The radiation shielding components, used in space missions in the low earth orbit, require a wide range of working temperatures (up to 100 °C) in order to avoid potential risks of thermal degradation due to the harsh environment [3].

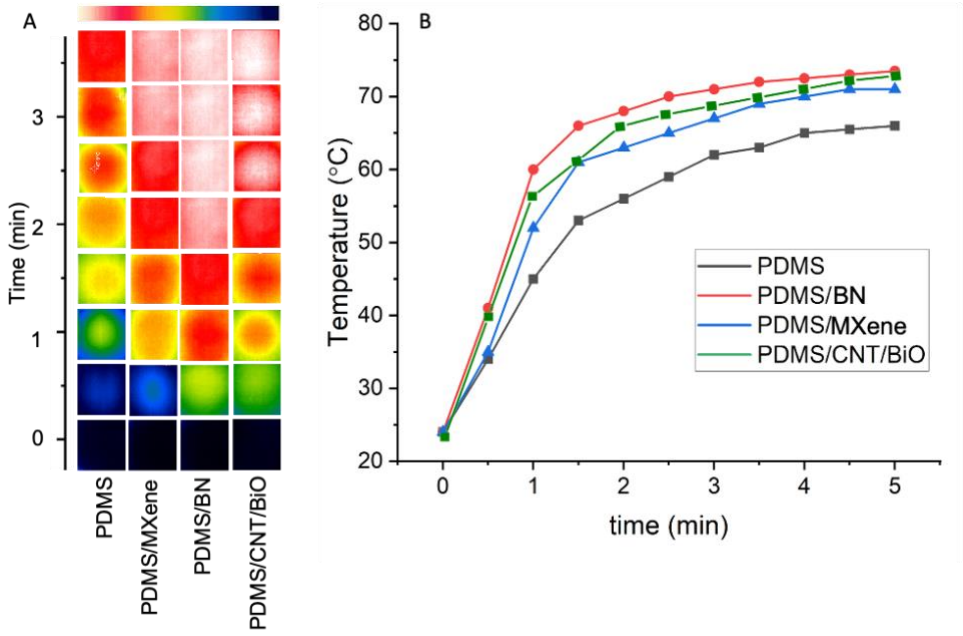

Figure 6-9. (A) Infrared thermal images of samples at different heating time, (B) Surface temperature changes of all samples at different moments of heating process.

The effect of filler types on thermal conductivity of each layer also visualized utilizing an infrared camera to record the temperature of the upper surface of samples on a heating plate. Such as what

previous measurement is chapter 5, samples were placed on an isothermal hot plate with a constant temperature of 70 °C, for 5 minutes. The measured temperature at the upper surface of samples were plotted as a function of heating time (Figure 6-9B). The slope of each line reflects the rate of the temperature change. Nanocomposite containing boron nitride shows the highest rate of temperature change. In addition, as Figure 6-9A shows, the surface color of pure polymer and all composites was dark blue at the first moment of the heating process, corresponding to the room temperature (24 °C). With increasing the temperature of samples, the surface color changes to green, yellow, red, and finally the whitish red at different rates, indicating that the temperature of samples changes at various rates. According to Figure 6-9, the surface temperature of the PDMS/BN composite is higher than the other samples at any time, because of the high thermal conductivity of well-dispersed OHBN [103].

6.3.4 Electron shielding results

To evaluate the shielding efficiency of layered nanocomposite, first the AE% of each nanocomposite with areal density of 1 g/cm^2 were measured and compared to that of the layered sample with same areal density. Figure 6-10 A1 to A4 shows the irradiated samples. Results indicate that the PDMS/BN nanocomposite has lower AE % of all samples (12 to 63 % lower than that of the PDMS/CNT/BiO). As can be seen in Figure 6-10 B, PDMS/MXene nanocomposite also shows lower AE% than PDMS/CNT/BiO. However, applying all the nanocomposites in layer sample result in AE % enhancement. Although the attenuation value for layer nanocomposite is up to 4.8 % smaller than that of the PDMS/CNT/BiO, but the percentage of Bi_2O_3 in layer sample is about 60 wt.% fewer than PDMS/CNT/BiO nanocomposite which is a considerable difference. In addition, other nanofillers applied in layer nanocomposite such as boron nitride, enhance the different properties of shielding nanocomposite such as thermal management. All these advantages result in considering layer nanocomposite for further evaluation.

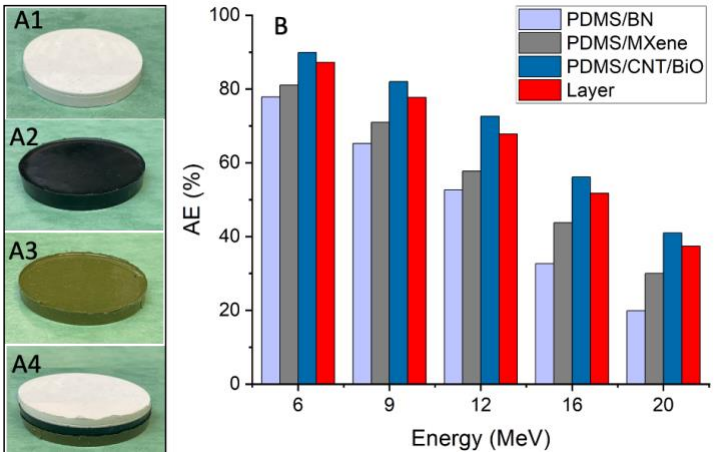

Figure 6-10. (A) The fabricated nanocomposites: PDMS/BN (A1), PDMS/MXene (A2), PDMS/CNT/BiO (A3), and layer nanocomposite (A4). (B) Attenuation efficiency (%) of 1 g/cm^2 PDMS/BN, PDMS/MXene, PDMS/CNT/BiO, and the layer composite for comparison.

The Attenuation Efficiency (AE%) of layered nanocomposites wear measured at five electron beam energies (6, 9, 12, 16, and 20 MeV) and compared to that of the PDMS/CNT/BiO and aluminum. Results are plotted as shown in. According to the Figure 6-11, the AE% for all the samples increases with increasing the areal density.

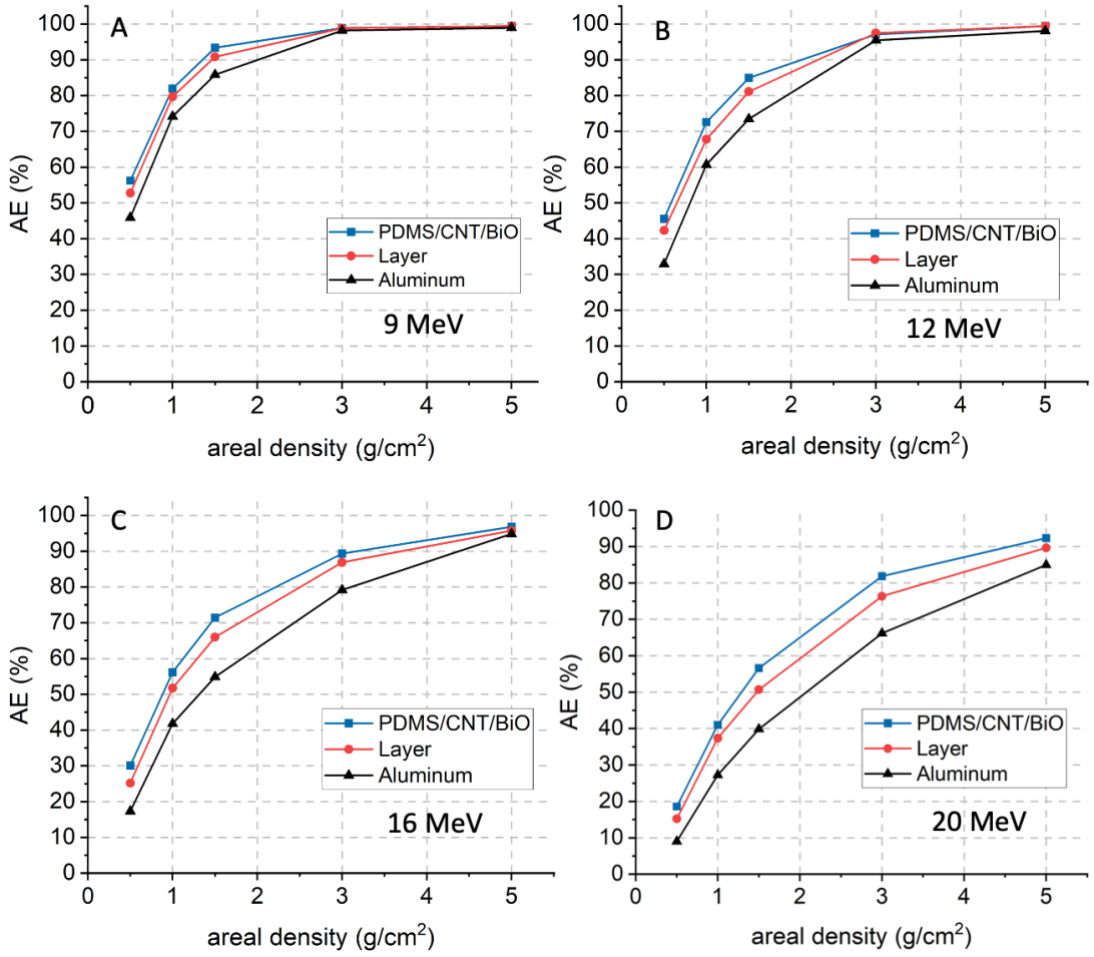

Figure 6-11. Percentage of attenuation efficiency (AE%) of all samples at (A) 6 MeV, (B) 9 MeV, (C) 12 MeV, (D) 16 MeV, and (20) MeV.

For all the areal densities, the layered nanocomposite shows higher AE% than Al. The difference at areal densities <3 g/cm^2 (Figure 6-11) is more considerable. For example, at areal density of 1.5 g/cm^2 under the 16 MeV electron beam, the layer nanocomposite attenuates efficiency is about 20 % more than that of the Al. In addition, at higher areal densities than 3 g/cm^2, both layer nanocomposite and PDMS/CNT/BiO sample show attenuation advantage at 16 and 20 MeV electron beam energies. As can be seen in Figure 6-11D, the attenuation efficiency of Al sample with an aerial density of 5 g/cm^2, is about 85%. However, this value is $\geq$90% for both nanocomposite samples.

As mentioned previously, the areal density is indicative of the weight required for each of the materials for shielding the electron radiation. The percentage attenuation characteristic of layer nanocomposite is similar and/or close to the control sample (PDMS/CNT/BiO in this experiment). However, it has less high-Z (Bi) content, but more low-Z fillers (B and N). For instance, Figure **6-12** shows, the AE% of the three samples at 9 MeV electron beam energy. Both nanocomposite samples have the same AE% at many aerial densities, but they both have better AE% of Al. Also, the maximum electron attenuation of 98% was obtained at areal density of ~2.5 g/cm^2 which was introduced as saturated point of areal density in Chapter 5.

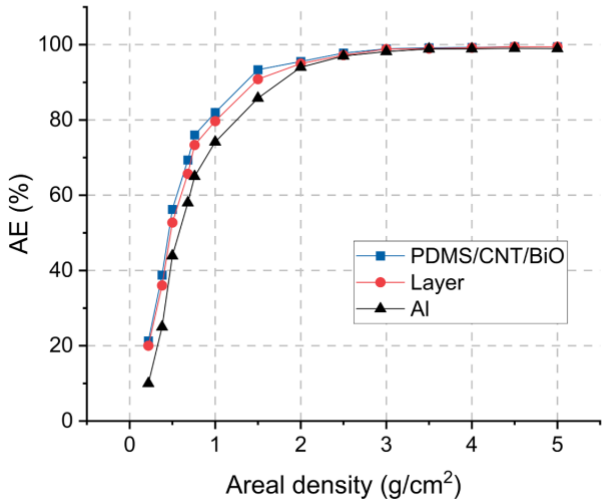

Figure 6-12. A point-by-point AE % of the materials at 9 MeV

Finally, as noted above, both the PDMS/CNT/BiO nanocomposite and layer sample show higher AE% than Al. This means, for the same AE% lighter nanocomposite is required compared to Al. Since the AE of 90% and higher is important in space radiation shielding application [6][168], the weight advantage of layer nanocomposite with respect to Al for beam attenuation of 90% for all energies is summarized in Table 6-2.

Table 6-2. Weight advantage of PDMS/CNT/BiO and layer nanocomposite with respect to Al for all electron energies.

Electron Beam Energy (MeV)	**Weight advantage of layer composite at 90% e-beam attenuation comparing to Al (%)**	
	PDMS/CNT/BiO	**Layer nanocomposite**
6	37	31
9	35	30
12	28.5	17.8
16	31.8	26
20	19.6	15

6.4 Chapter Summary

Although the previously developed nanocomposite had a weight advantage of up to 34% over Al, and higher AE% in any areal densities, but It still has an extremely high content of high-Z filler (Bi). Therefore, layer nanocomposite was considered and developed to not only keep the weight advantage, but also increase the low-Z filler content and reduce the chance of secondary radiation generation.

Boron nitride and MXene with high thermal stability and thermal conductivity was chosen in this regard. The chemical composition analysis revealed that both OHBN and MXene nanoporticles can attach to polymer chain and creat chemical bindings. Also, SEM images confirm the dispersion of nanofillers in polymer matrix.

According to the TGA and DSC results, both PDMS/BN and PDMS/MXene nanocomposites higher thermal stability that pure PDMS, and they can work in a temperature range of -40 to 190 °C. Also, the heat flow was observed to be enhanced in both nanocomposites comparing to the pure PDMS.

In terms of shielding efficiency, the AE% of PDMS/BN and PDMS/MXene samples was up to 63% lower than that of the PDMS/CNT/BiO, however, applying all these nanocomposites in layer structure resulted in an AE% similar to that of the PDMS/CNT/BiO sample, with up to 30 % weight advantage over Al.

Chapter 7 Conclusion and Future Studies

7.1 Conclusion

Although several studies have been conducted on materials for space applications, but the current applied shielding materials are still limited by the low functions to weight ratio, insufficient shielding efficiency, complications in manufacturing and handling process, and excessive cost. Up until now, many composites have been considered for the application in space missions to reduce the overall weight with same or better shielding efficiency compared to metallic materials such as Al. One of the promising materials for developing novel radiation shielding design, are the polymer-based nanocomposites. According to the ease of tuning material properties by applying nanofillers and the unique physical and mechanical properties of carbon-base nanomaterials, carbon nanotube and MXene were targeted to be applied as effective nanofillers providing multifunctional reinforcement in polymer matrix. In addition, bismuth oxide and hexagonal boron nitride were selected for further shielding efficiency enhancement considering their superior comprehensive material properties. Developed nanocomposites were evaluated by radiation shielding tests and characterization to clarify their properties and potentials. The major contributions of this research study are listed here:

After reviewing the literature, PDMS, MWCNT, and Bi_2O_3 were selected for polymer-based nanocomposite fabrication. First, Pure PDMS, PDMS/BiO, and PDMS/CNT nanocomposites with different wt.% of fillers content (5, 10, 15, 20, and 30 wt.% Bi_2O_3, 1, 5, and 10 wt.% MWCNT) and 1 mm thickness were fabricated and characterized. Regarding the mechanical properties, tensile strength of all samples was measured, and the order was found: PDMS: 1.6 MPa < PDMS/30 wt.% Bi_2O_3: 4.65 MPa < PDMS/5 wt.% MWCNT: 5.53 MPa. Afterward, to study the selected materials shielding potentials, samples were irradiated by x-ray with 60 to 90 keV energy and photon transmission was calculated. The experimental study indicated that the 1 mm thick nanocomposite containing 30 wt.% of Bi_2O_3 can transmit up to 32% of x-ray with energy of 60 to 90 keV. According to the measured properties, PDMS/30 wt.% Bi_2O_3 (PDMS/BiO) and PDMS/5

wt.% MWCNT (PDMS/CNT) was selected for further characterization and radiation shielding test.

To investigate the layer structure effect on transmission rate, multilayer nanocomposites in 2 to 5 layers were fabricated with alternately PDMS/BiO and PDMS/CNT layers and were characterized for mechanical strength and x-ray transmission rate. The 5-layer nanocomposite improves the mechanical strength from 1.7 MPa in neat PDMS to 4.68 MPa. It is also capable of attenuating 89% of the scattered x-rays generated at a tube potential of 60 keV.

For more comparison and radiation shielding measurements, PDMS/CNT/BiO nanocomposite were also fabricated, in addition to previously fabricated nanocomposites (PDMS/CNT and PDMS/BiO). Then, thermal stability of pure PDMS and all the nanocomposites was studied form room temperature to 800 °C, applying TGA analysis. The temperature of thermal decomposition was observed about 15% higher for nanocomposites containing both MWCNT and Bi_2O_3 compared to PDMS.

Regarding electron shielding test, all the samples were fabricated with five different areal densities (0.5, 1, 1.5, 3, and 5 g/cm^2) and irradiated by electron beam with 6, 9, 12, 16, and 20 MeV energies. Also, Al samples with same areal densities was prepared and irradiated by electron beam to compare the results with that of the nanocomposites. Both PDMS/BiO and PDMS/CNT/BiO nanocomposites presented higher attenuation efficiency than aluminum. For example, at areal density of 1.5 g/cm^2, aluminum attenuates about 80% of electron beam with 16 MeV energy. This number increases to 90% for PDMS/CNT/BiO with the same areal density under the electron beam energy. In addition, the developed nanocomposites have a weight advantage of up to 36% in comparison with aluminum.

To further improve the shielding efficiency of nanocomposites and reduce the high-Z filler content (Bi_2O_3), a layer structure was fabricated in three layers. For each layer different nanocomposite were designed, using various nanofillers but same polymer matrix (PDMS). According to high radiation shielding potentials of boron nitride and carbon-based 2D MXene, these nanofillers were selected for the layer nanocomposite fabrication. Afterward, a layer nanocomposite containing PDMS/BN (in first layer)/ PDMS/MXene (in second layer)/ PDMS/CNT/BiO (in third layer). TGA results indicated that all the layers have higher temperature of thermal decomposition than

pure PDMS. Also, the working temperature of all the layers are between -40 to <200 °C, which indicates they can fulfill the requirements for space radiation shielding application.

Electron attenuation efficiency of layer nanocomposite were evaluated too. First, PDMS/BN, PDMS/MXene, and layer samples with an areal density 1 g/cm^2 were irradiated by 6, 9, 12, 16, and 20 MeV electron beam to compare the AE % of them with that of the PDMS/CNT/BiO. According to the results, PDMS/BN and PDMS/MXene nanocomposites has up to 63% lower AE % than PDMS/CNT/BiO. However, applying all these nanocomposites in layer structure improves the AE %. The layer structure, with 60 wt.% less high-Z (BiO) content, and more low-Z (BN) and medium-Z (Ti and Mo MXenes) filler contents, exhibited AE % of up to 20 % higher than Al. The weight advantage of layer nanocomposite was up to 31 % under 6 MeV electron beam in comparison with Al.

7.2 Future Work

The conducted work in this research has developed and evaluated a light-weight radiation shielding nanocomposite, which is greatly promising for industrial and/or commercial application.

However, there are still research and unexplored possibilities that can be done for further improvement, as listed here:

- Electron shielding simulation: according to the electron shielding results of layer nanocomposite, simulations such as Monte Carlo method can be applied optimize the portion of layers for the highest attenuation efficiency.

- Proton shielding evaluation: Regarding the proven potential of PDMS composites in energetic proton radiation shielding, the fabricated layer nanocomposite is expected to stop high energy proton particles efficiently. The shielding performance can be evaluated and compared with Al to further investigate the weight advantage.

- Secondary neutron radiation absorption: Boron (^{10}B) with a neutron absorption cross section of 3835 barns, has been proven an ideal filler for thermal neutron absorption. Therefore, boron nitride, as a boron rich material and with high thermal conductivity, is a

promising candidate for reducing the secondary neutron generation and absorbing the neutron radiations. The 3-layer nanocomposite with outer layer of nanocomposite with high-Z material, such as Bi_2O_3, should be investigated for this purpose.

References

[1] F. A. Cucinotta, M. H. Y. Kim, and L. Ren, "Evaluating shielding effectiveness for reducing space radiation cancer risks," *Radiat. Meas.*, vol. 41, no. 9–10, pp. 1173–1185, 2006, doi: 10.1016/j.radmeas.2006.03.011.

[2] W. R. Webber and T. L. Villa, "The Galactic Cosmic Ray Electron Spectrum from 3-70 MeV Measured by Voyager 1 Beyond the Heliopause – What This Tells Us About the Propagation of Electrons and Nuclei In and Out of the Galaxy at Low Energies," *arXiv Prepr.*, pp. 1–21, 2017.

[3] E. R. Benton and E. V. Benton, "Space radiation dosimetry in low-Earth orbit and beyond," *Nucl. Instruments Methods Phys. Res. Sect. B Beam Interact. with Mater. Atoms*, vol. 184, no. 1–2, pp. 255–294, 2001, doi: 10.1016/S0168-583X(01)00748-0.

[4] J. C. Chancellor, G. B. I. Scott, and J. P. Sutton, "Space radiation: The number one risk to astronaut health beyond low earth orbit," *Life*, vol. 4, no. 3, pp. 491–510, 2014, doi: 10.3390/life4030491.

[5] M. Durante, "Space radiation protection: Destination Mars," *Life Sci. Sp. Res.*, vol. 1, no. 1, pp. 2–9, 2014, doi: 10.1016/j.lssr.2014.01.002.

[6] F. a Cucinotta, M. Y. Kim, and L. J. Chappell, "Evaluating Shielding Approaches to Reduce Space Radiation Cancer Risks," *Tm-2012-217361*, no. May, pp. 1–46, 2012.

[7] A. J. Piekutowski, K. L. Poormon, E. L. Christiansen, and B. A. Davis, "Performance of whipple shields at impact velocities above 9 km/s," *Int. J. Impact Eng.*, vol. 38, no. 6, pp. 495–503, 2011, doi: 10.1016/j.ijimpeng.2010.10.021.

[8] N. J. Carron, "An introduction to the passage of energetic particles through matter," *An Introd. to Passage Energ. Part. Through Matter*, no. January 2006, pp. 1–355, 2006, doi: 10.1201/9781420012378.

[9] J. H. Adams *et al.*, "Revolutionary Concepts of Radiation Shielding for Human

Exploration of Space," *Nasa*, no. March, pp. 1–110, 2005, [Online]. Available: http://hdl.handle.net/2060/20050180620.

[10] E. R. Jawin, S. N. Valencia, R. N. Watkins, J. M. Crowell, C. R. Neal, and G. Schmidt, "Lunar Science for Landed Missions Workshop Findings Report," *Earth Sp. Sci.*, vol. 6, no. 1, pp. 2–40, 2019, doi: 10.1029/2018EA000490.

[11] K. K. D. E. Groh *et al.*, *NASA Glenn Research Center's Materials International Space Station Experiments (MISSE 1-7)*, no. December 2008. 2008.

[12] L. N. M. Clayton, T. G. Gerasimov, M. Cinke, M. Meyyappan, and J. P. Harmon, "Dispersion of single-walled carbon nanotubes in a non-polar polymer, poly(4-methyl-1-pentene).," *J. Nanosci. Nanotechnol.*, vol. 6, no. 8, pp. 2520–2524, 2006, doi: 10.1166/jnn.2006.537.

[13] P. Zhou, "MULTI-FUNCTIONAL LAYERED STRUCTURE HAVING STRUCTURAL AND RADIATION SHIELDING ATTRIBUTES," *New York*, vol. 1, no. 19, pp. 1–29, 2010.

[14] A. Märki, "Radiation Analysis for Moon and Mars Missions," *Int. J. Astrophys. Sp. Sci.*, vol. 8, no. 3, p. 16, 2020, doi: 10.11648/j.ijass.20200803.11.

[15] P. A. O'Rourke *et al.*, "Effects of gamma radiation on poly(methyl methacrylate)/single-wall nanotube composites," *J. Mater. Res.*, vol. 17, no. 10, pp. 2507–2513, 2002, doi: 10.1557/jmr.2002.0365.

[16] Z. Yang, H. Peng, W. Wang, and T. Liu, "Processing and properties of carbon nanotube/poly(methyl methacrylate) composite films," *J. Appl. Polym. Sci.*, vol. 116, no. 5, pp. 2658–2667, 2010, doi: 10.1002/app.

[17] E. Cheraghi, S. Chen, and J. T. W. Yeow, "Boron Nitride-Based Nanomaterials for Radiation Shielding: A Review," *IEEE Nanotechnol. Mag.*, vol. 15, no. 3, pp. 8–17, 2021, doi: 10.1109/MNANO.2021.3066390.

[18] Z. Li, S. Nambiar, W. Zheng, and J. T. W. Yeow, "PDMS/single-walled carbon nanotube

composite for proton radiation shielding in space applications," *Mater. Lett.*, vol. 108, pp. 79–83, 2013, doi: 10.1016/j.matlet.2013.06.030.

[19] E. Najafi and K. Shin, "Radiation resistant polymer-carbon nanotube nanocomposite thin films," in *Colloids and Surfaces A: Physicochemical and Engineering Aspects*, 2005, doi: 10.1016/j.colsurfa.2004.10.076.

[20] S. Mathew *et al.*, "The effect of layer number and substrate on the stability of graphene under MeV proton beam irradiation," *Carbon N. Y.*, vol. 49, no. 5, pp. 1720–1726, 2011, doi: 10.1016/j.carbon.2010.12.057.

[21] R. H. Telling, C. P. Ewels, A. A. El-Barbary, and M. I. Heggie, "Wigner defects bridge the graphite gap," *Nat. Mater.*, vol. 2, no. 5, pp. 333–337, 2003, doi: 10.1038/nmat876.

[22] A. V. Krasheninnikov and F. Banhart, "Engineering of nanostructured carbon materials with electron or ion beams," *Nat. Mater.*, vol. 6, no. 10, pp. 723–733, 2007, doi: 10.1038/nmat1996.

[23] C.-H. Ho, C.-H. Chan, Y.-S. Huang, L.-C. Tien, and L.-C. Chao, "The study of optical band edge property of bismuth oxide nanowires α-Bi2O3," *Opt. Express*, vol. 21, no. 10, p. 11965, 2013, doi: 10.1364/oe.21.011965.

[24] L. Leontie, M. Caraman, M. Alexe, and C. Harnagea, "Structural and optical characteristics of bismuth oxide thin films," *Surf. Sci.*, vol. 507–510, pp. 480–485, 2002, doi: 10.1016/S0039-6028(02)01289-X.

[25] V. P. Singh, N. M. Badiger, N. Chanthima, and J. Kaewkhao, "Evaluation of gamma-ray exposure buildup factors and neutron shielding for bismuth borosilicate glasses," *Radiat. Phys. Chem.*, vol. 98, pp. 14–21, 2014, doi: 10.1016/j.radphyschem.2013.12.029.

[26] A. Sonsilphong and N. Wongkasem, "Light-weight radiation protection by non-lead materials in X-ray regimes," *Proc. - 2014 Int. Conf. Electromagn. Adv. Appl. ICEAA 2014*, no. February, pp. 656–658, 2014, doi: 10.1109/ICEAA.2014.6903939.

[27] Q. Li *et al.*, "Enhanced Radiation Shielding with Conformal Light-Weight Nanoparticle-

Polymer Composite," *ACS Appl. Mater. Interfaces*, vol. 10, no. 41, pp. 35510–35515, 2018, doi: 10.1021/acsami.8b10600.

[28] H. Wu *et al.*, "Layer-by-Layer Assembly of Multifunctional NR/MXene/CNTs Composite Films with Exceptional Electromagnetic Interference Shielding Performances and Excellent Mechanical Properties," *Macromol. Rapid Commun.*, vol. 2200387, p. 2200387, 2022, doi: 10.1002/marc.202200387.

[29] L. Gilys, E. Griškonis, P. Griškevi˘cius, and D. Adlienė, "Lead Free Multilayered Polymer Composites for Radiation Shielding," *Polymers (Basel).*, vol. 14, no. 9, p. 1696, 2022.

[30] D. Adlienė, L. Gilys, and E. Griškonis, "Development and characterization of new tungsten and tantalum containing composites for radiation shielding in medicine," *Nucl. Instruments Methods Phys. Res. Sect. B Beam Interact. with Mater. Atoms*, vol. 467, no. November 2019, pp. 21–26, 2020, doi: 10.1016/j.nimb.2020.01.027.

[31] G. A. Nelson, "Space Radiation and Human Exposures, A Primer," *Radiat. Res.*, vol. 185, no. 4, pp. 349–358, 2016, doi: 10.1667/rr14311.1.

[32] G. Reitz, "Characteristic of the radiation field in low earth orbit and in deep space," *Z. Med. Phys.*, vol. 18, no. 4, pp. 233–243, 2008, doi: 10.1016/j.zemedi.2008.06.015.

[33] J. C. Chancellor *et al.*, "Limitations in predicting the space radiation health risk for exploration astronauts," *npj Microgravity*, vol. 4, no. 1, pp. 1–11, 2018, doi: 10.1038/s41526-018-0043-2.

[34] M. Durante, A. Golubev, W. Y. Park, and C. Trautmann, "Applied nuclear physics at the new high-energy particle accelerator facilities," *Phys. Rep.*, vol. 800, pp. 1–37, 2019, doi: 10.1016/j.physrep.2019.01.004.

[35] N. Gopalswamy, P. Mäkelä, S. Yashiro, H. Xie, S. Akiyama, and N. Thakur, "High-energy solar particle events in cycle 24," *J. Phys. Conf. Ser.*, vol. 642, no. 1, 2015, doi: 10.1088/1742-6596/642/1/012012.

[36] I. G. Usoskin and G. A. Kovaltsov, "Occurrence of extreme solar particle events:

Assessment from historical proxy data," *Astrophys. J.*, vol. 757, no. 1, 2012, doi: 10.1088/0004-637X/757/1/92.

[37] F. Cucinotta, M. Kim, and L. Chappell, "Space radiation cancer risk projections and uncertainties-2010," *NASA Tech. Pap.*, no. July, pp. 1–132, 2011, [Online]. Available: http://www.csc.caltech.edu/references/SpaceRadiationCancerRiskProjectionsandUncertainties.pdf.

[38] J. F. Hochedez *et al.*, "Solar weather monitoring," *Ann. Geophys.*, vol. 23, no. 9, pp. 3149–3161, 2005, doi: 10.5194/angeo-23-3149-2005.

[39] R. Schwenn, "Space Weather : The Solar Perspective Imprint / Terms of Use," *Living Rev. Sol. Phys.*, no. 2006, 2010.

[40] J. L. Barth, C. S. Dyer, and E. G. Stassinopoulos, "Space, atmospheric, and terrestrial radiation environments," *IEEE Trans. Nucl. Sci.*, vol. 50 III, no. 3, pp. 466–482, 2003, doi: 10.1109/TNS.2003.813131.

[41] J. W. Wilson, "Shielding Strategies for Human Space Exploration NASA Conference Publication 3360 Shielding Strategies for Human Space Exploration Edited by," no. April, 1998.

[42] S. Nambiar and J. T. W. Yeow, "Polymer-composite materials for radiation protection," *ACS Appl. Mater. Interfaces*, vol. 4, no. 11, pp. 5717–5726, 2012, doi: 10.1021/am300783d.

[43] G. Williams, R. Trask, and I. Bond, "A self-healing carbon fibre reinforced polymer for aerospace applications," *Compos. Part A Appl. Sci. Manuf.*, vol. 38, no. 6, pp. 1525–1532, 2007, doi: 10.1016/j.compositesa.2007.01.013.

[44] L. W. Townsend and R. J. M. Fry, "Radiation protection guidance for activities in low-Earth orbit," *Adv. Sp. Res.*, vol. 30, no. 4, pp. 957–963, 2002, doi: 10.1016/S0273-1177(02)00160-6.

[45] C. V. More, Z. Alsayed, M. S. Badawi, A. A. Thabet, and P. P. Pawar, *Polymeric*

composite materials for radiation shielding: a review, vol. 19, no. 3. Springer International Publishing, 2021.

[46] Y. Lu, Q. Shao, H. Yue, and F. Yang, "A Review of the Space Environment Effects on Spacecraft in Different Orbits," *IEEE Access*, vol. 7, pp. 93473–93488, 2019, doi: 10.1109/ACCESS.2019.2927811.

[47] K. A. LaBel, "SEECA - Single Event Effect Criticality Analysis," *Nieznane Czas.*, 1996, doi: 10.1149/1.2127238.

[48] F. Miller *et al.*, "Characterization of single-event burnout in power MOSFET using backside laser testing," *IEEE Trans. Nucl. Sci.*, vol. 53, no. 6, pp. 3145–3152, 2006, doi: 10.1109/TNS.2006.885376.

[49] J. W. Norbury *et al.*, "Galactic cosmic ray simulation at the NASA Space Radiation Laboratory," *Life Sci. Sp. Res.*, vol. 8, no. February, pp. 38–51, 2016, doi: 10.1016/j.lssr.2016.02.001.

[50] M. E. Vazquez, "Neurobiological problems in long-term deep space flights," *Adv. Sp. Res.*, vol. 22, no. 2, pp. 171–183, 1998, doi: 10.1016/S0273-1177(98)80009-4.

[51] B. M. Rabin, K. L. Carrihill-Knoll, and B. Shukitt-Hale, "Operant responding following exposure to HZE particles and its relationship to particle energy and linear energy transfer," *Adv. Sp. Res.*, vol. 48, no. 2, pp. 370–377, 2011, doi: 10.1016/j.asr.2011.03.008.

[52] S. R. Manohara, S. M. Hanagodimath, K. S. Thind, and L. Gerward, "On the effective atomic number and electron density: A comprehensive set of formulas for all types of materials and energies above 1 keV," *Nucl. Instruments Methods Phys. Res. Sect. B Beam Interact. with Mater. Atoms*, vol. 266, no. 18, pp. 3906–3912, 2008, doi: 10.1016/j.nimb.2008.06.034.

[53] X. Li, D. Warden, and Y. Bayazitoglu, "Analysis to evaluate multilayer shielding of galactic cosmic rays," *J. Thermophys. Heat Transf.*, vol. 32, no. 2, pp. 525–531, 2018, doi: 10.2514/1.T5292.

[54] A. Al-Okour, “Radiation Physics: Radiation interaction with matter,” *Mater. Today Proc.*, no. xxxx, 2021, doi: 10.1016/j.matpr.2020.11.566.

[55] J. Sharif, W. M. Z. W. Yunus, K. Z. H. M. Dahlan, and M. H. Ahmad, “Preparation and properties of radiation crosslinked natural rubber/clay nanocomposites,” *Polym. Test.*, vol. 24, no. 2, pp. 211–217, 2005, doi: 10.1016/j.polymertesting.2004.08.008.

[56] A. Saxena, H. Singh, P. Agrawal, S. K. Rathi, and A. S. Verma, “Stopping Power of Electrons and Positrons for C, Al, Cu, Ag, Au, Pb, Fe, U, Ge, Si and Mo,” *Appl. Phys. Res.*, vol. 2, no. 2, 2010, doi: 10.5539/apr.v2n2p176.

[57] J. C. Williams and E. A. Starke, “Progress in structural materials for aerospace systems,” *Acta Mater.*, vol. 51, no. 19, pp. 5775–5799, 2003, doi: 10.1016/j.actamat.2003.08.023.

[58] I. A. Tsekmes, R. Kochetov, P. H. F. Morshuis, and J. J. Smit, “Thermal conductivity of polymeric composites: A review,” *Proc. IEEE Int. Conf. Solid Dielectr. ICSD*, pp. 678–681, 2013, doi: 10.1109/ICSD.2013.6619698.

[59] S. A. Thibeault *et al.*, “Radiation Shielding Materials Containing Hydrogen, Boron, and Nitrogen: Systematic Computational and Experimental Study,” pp. 1–29, 2012, [Online]. Available: https://ntrs.nasa.gov/search.jsp?R=20160010096.

[60] S. Nambiar, E. K. Osei, and J. T. W. Yeow, “Polymer nanocomposite-based shielding against diagnostic X-rays,” *J. Appl. Polym. Sci.*, vol. 127, no. 6, pp. 4939–4946, 2013, doi: 10.1002/app.37980.

[61] K. Chikaoui, M. Izerrouken, M. Djebara, and M. Abdesselam, “Polyethylene terephthalate degradation under reactor neutron irradiation,” *Radiat. Phys. Chem.*, 2017, doi: 10.1016/j.radphyschem.2016.10.002.

[62] M. E. Mahmoud, A. M. El-Khatib, M. S. Badawi, A. R. Rashad, R. M. El-Sharkawy, and A. A. Thabet, “Recycled high-density polyethylene plastics added with lead oxide nanoparticles as sustainable radiation shielding materials,” *J. Clean. Prod.*, vol. 176, pp. 276–287, 2018, doi: 10.1016/j.jclepro.2017.12.100.

[63] C. Zeitlin, S. B. Guetersloh, L. H. Heilbronn, and J. Miller, “Measurements of materials shielding properties with 1 GeV/nuc 56Fe,” *Nucl. Instruments Methods Phys. Res. Sect. B Beam Interact. with Mater. Atoms*, vol. 252, no. 2, pp. 308–318, 2006, doi: 10.1016/j.nimb.2006.08.011.

[64] Carraher Jr. Charles E., “Introduction to Polymer Chemistry Macromolecular Chemistry – Chemistry of Plastics.” 2017.

[65] T. Zhang and T. Luo, “Role of Chain Morphology and Stiffness in Thermal Conductivity of Amorphous Polymers,” *J. Phys. Chem. B*, vol. 120, no. 4, pp. 803–812, 2016, doi: 10.1021/acs.jpcb.5b09955.

[66] J. W. Shin *et al.*, “Polyethylene/boron-containing composites for radiation shielding,” *Thermochim. Acta*, vol. 585, pp. 5–9, 2014, doi: 10.1016/j.tca.2014.03.039.

[67] S. Paul, *Biomedical Engineering and its Applications in Healthcare*. 2019.

[68] A. I. Wozniak, V. S. Ivanov, O. A. Zhdanovich, V. I. Nazarov, and A. S. Yegorov, “Modern approaches to polymer materials protecting from ionizing radiation,” *Orient. J. Chem.*, vol. 33, no. 5, pp. 2148–2163, 2017, doi: 10.13005/ojc/330502.

[69] H. M. S. Iqbal, S. Bhowmik, R. Benedictus, J. B. Moon, C. G. Kim, and A. H. I. Mourad, “Processing and characterization of space-durable high-performance polymeric nanocomposite,” *J. Thermophys. Heat Transf.*, vol. 25, no. 1, pp. 87–95, 2011, doi: 10.2514/1.50841.

[70] A. Kumar, K. Sharma, and A. R. Dixit, “A review of the mechanical and thermal properties of graphene and its hybrid polymer nanocomposites for structural applications,” *J. Mater. Sci.*, vol. 54, no. 8, pp. 5992–6026, 2019, doi: 10.1007/s10853-018-03244-3.

[71] R. I. Rubel, M. H. Ali, M. A. Jafor, and M. M. Alam, “Carbon nanotubes agglomeration in reinforced composites: A review,” *AIMS Mater. Sci.*, vol. 6, no. 5, pp. 756–780, 2019, doi: 10.3934/matersci.2019.5.756.

[72] S. K. Soni, B. Thomas, and V. R. Kar, “A Comprehensive Review on CNTs and CNT-

Reinforced Composites: Syntheses, Characteristics and Applications," *Mater. Today Commun.*, vol. 25, no. June, p. 101546, 2020, doi: 10.1016/j.mtcomm.2020.101546.

[73] C. D. Cress, J. J. McMorrow, J. T. Robinson, B. J. Landi, S. M. Hubbard, and S. R. Messenger, "Radiation effects in carbon nanoelectronics," *Electron.*, vol. 1, no. 1, pp. 23–31, 2012, doi: 10.3390/electronics1010023.

[74] P. J. Boul *et al.*, "Single wall carbon nanotube response to proton radiation," *J. Phys. Chem. C*, vol. 113, no. 32, pp. 14467–14473, 2009, doi: 10.1021/jp808553u.

[75] M. Dejangah, M. Ghojavand, R. Poursalehi, and P. R. Gholipour, "X-ray attenuation and mechanical properties of tungsten-silicone rubber nanocomposites," *Mater. Res. Express*, vol. 6, no. 8, 2019, doi: 10.1088/2053-1591/ab1a89.

[76] Y. Wang *et al.*, "Lightweight and Wearable X-Ray Shielding Material with Biological Structure for Low Secondary Radiation and Metabolic Saving Performance," *Adv. Mater. Technol.*, vol. 5, no. 7, pp. 1–8, 2020, doi: 10.1002/admt.202000240.

[77] D. Toyen, A. Rittirong, W. Poltabtim, and K. Saenboonruang, "Flexible, lead-free, gamma-shielding materials based on natural rubber/metal oxide composites," *Iran. Polym. J. (English Ed.*, vol. 27, no. 1, pp. 33–41, 2018, doi: 10.1007/s13726-017-0584-3.

[78] T. Özdemir and S. N. Yılmaz, "Mixed radiation shielding via 3-layered polydimethylsiloxane rubber composite containing hexagonal boron nitride, boron (III) oxide, bismuth (III) oxide for each layer," *Radiat. Phys. Chem.*, vol. 152, no. December 2017, pp. 17–22, 2018, doi: 10.1016/j.radphyschem.2018.07.007.

[79] Y. Zhu, J. Liu, T. Guo, J. J. Wang, X. Tang, and V. Nicolosi, "Multifunctional Ti3C2TxMXene Composite Hydrogels with Strain Sensitivity toward Absorption-Dominated Electromagnetic-Interference Shielding," *ACS Nano*, vol. 15, no. 1, pp. 1465–1474, 2021, doi: 10.1021/acsnano.0c08830.

[80] X. Huang and P. Wu, "A small amount of delaminated Ti3C2 flakes to greatly enhance the thermal conductivity of boron nitride papers by assembling a well-designed interface," *Mater. Chem. Front.*, vol. 4, no. 1, pp. 292–301, 2020, doi: 10.1039/c9qm00616h.

[81] S. Yuan, J. Bai, C. K. Chua, J. Wei, and K. Zhou, “Highly enhanced thermal conductivity of thermoplastic nanocomposites with a low mass fraction of MWCNTs by a facilitated latex approach,” *Compos. Part A Appl. Sci. Manuf.*, vol. 90, pp. 699–710, 2016, doi: 10.1016/j.compositesa.2016.09.002.

[82] C. W. Chang, W. Q. Han, and A. Zettl, “Thermal conductivity of B-C-N and BN nanotubes,” *Appl. Phys. Lett.*, vol. 86, no. 17, pp. 1–3, 2005, doi: 10.1063/1.1914963.

[83] K. Herrman, L. N. Baxter, K. Mishra, E. Benton, R. P. Singh, and R. K. Vaidyanathan, “Mechanical characterization of polyethylene-based thermoplastic composite materials for radiation shielding,” *Compos. Commun.*, vol. 13, no. February, pp. 37–41, 2019, doi: 10.1016/j.coco.2019.02.007.

[84] C. V. Oramas, D. D. Keluarga, and C. V. Oramas, “EVALUATION OF EFFICIENCY OF VARIOUS MATERIALS TO SHIELD FROM RADIATION IN SPACE USING THE MONTE CARLO TRANSPORT CODE CALLED FLUKA,” no. December, p. 2016, 2016.

[85] H. Daneshvar, K. G. Milan, A. Sadr, S. H. Sedighy, S. Malekie, and A. Mosayebi, “Multilayer radiation shield for satellite electronic components protection,” *Sci. Rep.*, vol. 11, no. 1, pp. 1–12, 2021, doi: 10.1038/s41598-021-99739-2.

[86] A. Emmanuel and J. Raghavan, “Influence of structure on radiation shielding effectiveness of graphite fiber reinforced polyethylene composite,” *Adv. Sp. Res.*, vol. 56, no. 7, pp. 1288–1296, 2015, doi: 10.1016/j.asr.2015.06.028.

[87] S. Thibeault, “Radiation Shielding Materials Containing Hydrogen, Boron, and Nitrogen: Systematic Computational and Experimental Study,” 2012, doi: 10.1016/S0092-8674(00)00005-2.

[88] J. E. Estevez, M. Ghazizadeh, J. G. Ryan, and A. D. Kelkar, “Simulation of Hydrogenated Boron Nitride Nanotube ’ s Mechanical Properties for Radiation Shielding Applications,” vol. 8, no. 1, pp. 63–67, 2014.

[89] A. Emmanuel, “Design and Development of a Multifunctional Composite Radiation

Shield for Space Applications," 2017.

[90] U. S. Patent, "United States Patent : 5861366 United States Patent : 5861366," *New York*, pp. 1–29, 2010.

[91] C. Harrison, E. Burgett, N. Hertel, and E. Grulke, "Polyethylene/boron composites for radiation shielding applications," *AIP Conf. Proc.*, vol. 969, no. January, pp. 484–491, 2008, doi: 10.1063/1.2845006.

[92] K. Patel, S. H. Chikkali, and S. Sivaram, "Ultrahigh molecular weight polyethylene: Catalysis, structure, properties, processing and applications," *Prog. Polym. Sci.*, vol. 109, 2020, doi: 10.1016/j.progpolymsci.2020.101290.

[93] I. Miranda *et al.*, "Properties and applications of PDMS for biomedical engineering: A review," *J. Funct. Biomater.*, vol. 13, no. 1, 2022, doi: 10.3390/jfb13010002.

[94] Z. Li *et al.*, "PMMA/MWCNT nanocomposite for proton radiation shielding applications," *Nanotechnology*, vol. 27, no. 23, 2016, doi: 10.1088/0957-4484/27/23/234001.

[95] S. Iijima, "Helical microtubules of graphitic carbon," *Nature*, vol. 354, pp. 737–740, 1991.

[96] A. M. Marconnet, N. Yamamoto, M. A. Panzer, B. L. Wardle, and K. E. Goodson, "Thermal conduction in aligned carbon nanotube-polymer nanocomposites with high packing density," *ACS Nano*, vol. 5, no. 6, pp. 4818–4825, 2011, doi: 10.1021/nn200847u.

[97] V. A. Basiuk, K. Kobayashi, T. Kaneko, Y. Negishi, E. V. Basiuk, and J. M. Saniger-Blesa, "Irradiation of Single-Walled Carbon Nanotubes with High-Energy Protons," *Nano Lett.*, vol. 2, no. 7, pp. 789–791, 2002, doi: 10.1021/nl025601y.

[98] M. CA. and K. R., "Dispersion of single-walled carbon nanotubes in poly(epsilon-caprolactone).," *Macromolecules*, vol. 40, no. 5, pp. 1538–45, 2007.

[99] E. A. Secretary and E. Management, "Review of Potential Wigner Effect Impacts on the

Irradiated Graphite in Decommissioned Hanford Reactors."

[100] S. Yu *et al.*, "Boron nitride-based materials for the removal of pollutants from aqueous solutions: A review," *Chem. Eng. J.*, vol. 333, no. September 2017, pp. 343–360, 2018, doi: 10.1016/j.cej.2017.09.163.

[101] S. A. Thibeault, J. H. Kang, G. Sauti, C. Park, C. C. Fay, and G. C. King, "Nanomaterials for radiation shielding," *MRS Bull.*, vol. 40, no. 10, pp. 836–841, 2015, doi: 10.1557/mrs.2015.225.

[102] T. Özdemir and S. N. Yılmaz, "Hexagonal boron nitride and polydimethylsiloxane: A ceramic rubber composite material for neutron shielding," *Radiat. Phys. Chem.*, vol. 152, no. July, pp. 93–99, 2018, doi: 10.1016/j.radphyschem.2018.08.008.

[103] C. Yu *et al.*, "Enhanced through-plane thermal conductivity of boron nitride/epoxy composites," *Compos. Part A Appl. Sci. Manuf.*, vol. 98, pp. 25–31, 2017, doi: 10.1016/j.compositesa.2017.03.012.

[104] S. Chen *et al.*, "Bismuth oxide-based nanocomposite for high-energy electron radiation shielding," *J. Mater. Sci.*, vol. 54, no. 4, pp. 3023–3034, 2019, doi: 10.1007/s10853-018-3063-0.

[105] X. Zhan, C. Si, J. Zhou, and Z. Sun, "MXene and MXene-based composites: Synthesis, properties and environment-related applications," *Nanoscale Horizons*, vol. 5, no. 2, pp. 235–258, 2020, doi: 10.1039/c9nh00571d.

[106] J. C. Lei, X. Zhang, and Z. Zhou, "Recent advances in MXene: Preparation, properties, and applications," *Front. Phys.*, vol. 10, no. 3, pp. 276–286, 2015, doi: 10.1007/s11467-015-0493-x.

[107] Y. Gogotsi and B. Anasori, "The Rise of MXenes," *ACS Nano*, vol. 13, no. 8, pp. 8491–8494, 2019, doi: 10.1021/acsnano.9b06394.

[108] W. T. Cao *et al.*, "Binary Strengthening and Toughening of MXene/Cellulose Nanofiber Composite Paper with Nacre-Inspired Structure and Superior Electromagnetic Interference

Shielding Properties," *ACS Nano*, vol. 12, no. 5, pp. 4583–4593, 2018, doi: 10.1021/acsnano.8b00997.

[109] M. Naguib *et al.*, "Two-dimensional transition metal carbides," *ACS Nano*, vol. 6, no. 2, pp. 1322–1331, 2012, doi: 10.1021/nn204153h.

[110] J. Wang *et al.*, "Self-Healed and Shape-Adaptive MXene Integrated Hydrogel for Wearable Electronic Applications," *Proc. IEEE Conf. Nanotechnol.*, vol. 2021-July, pp. 310–313, 2021, doi: 10.1109/NANO51122.2021.9514315.

[111] X. Xu *et al.*, "MXenes with applications in supercapacitors and secondary batteries: A comprehensive review," *Mater. Reports Energy*, vol. 2, no. 1, p. 100080, 2022, doi: 10.1016/j.matre.2022.100080.

[112] M. M. Tunesi, R. A. Soomro, X. Han, Q. Zhu, Y. Wei, and B. Xu, "Application of MXenes in environmental remediation technologies," *Nano Converg.*, vol. 8, no. 1, 2021, doi: 10.1186/s40580-021-00255-w.

[113] J. H. Park and S. C. Jana, "The relationship between nano- and micro-structures and mechanical properties in PMMA-epoxy-nanoclay composites," *Polymer (Guildf).*, vol. 44, no. 7, pp. 2091–2100, 2003, doi: 10.1016/S0032-3861(03)00075-2.

[114] M. J. Roshan, A. Jeevika, A. Bhattacharyya, and D. R. Shankaran, "One-pot fabrication and characterization of graphene/PMMA composite flexible films," *Mater. Res. Bull.*, vol. 105, no. September 2017, pp. 133–141, 2018, doi: 10.1016/j.materresbull.2018.04.034.

[115] G. Mittal, K. Y. Rhee, and S. J. Park, "Processing and characterization of PMMA/PI composites reinforced with surface functionalized hexagonal boron nitride," *Appl. Surf. Sci.*, vol. 415, pp. 49–54, 2017, doi: 10.1016/j.apsusc.2016.10.029.

[116] B. H. Xie, X. Huang, and G. J. Zhang, "High thermal conductive polyvinyl alcohol composites with hexagonal boron nitride microplatelets as fillers," *Compos. Sci. Technol.*, vol. 85, pp. 98–103, 2013, doi: 10.1016/j.compscitech.2013.06.010.

[117] R. Namitha, D. Radhika, and G. Krishnamurthy, "Hydrothermally synthesized carbon

nanotubes for electrochemical hydrogen storage application," *Vopr. Khimii i Khimicheskoi Tekhnologii*, vol. 2019, no. 3, pp. 30–34, 2019, doi: 10.32434/0321-4095-2019-124-3-30-34.

[118] A. S. Nazarov *et al.*, "Functionalization and dispersion of hexagonal boron nitride (h-BN) nanosheets treated with inorganic reagents," *Chem. - An Asian J.*, vol. 7, no. 3, pp. 554–560, 2012, doi: 10.1002/asia.201100710.

[119] A. D. Steinfeld, *Physics of Radiotherapy Planning and Delivery, in Technical Basis of Radiation Therapy*, vol. 21, no. 4. 1980.

[120] A. Pashazadeh, A. Boese, and M. Friebe, "Radiation therapy techniques in the treatment of skin cancer: an overview of the current status and outlook," *J. Dermatolog. Treat.*, vol. 30, no. 8, pp. 831–839, 2019, doi: 10.1080/09546634.2019.1573310.

[121] Y. Wang *et al.*, "Advanced X-ray Shielding Materials Enabled by the Coordination of Well-Dispersed High Atomic Number Elements in Natural Leather," *ACS Appl. Mater. Interfaces*, vol. 12, no. 17, pp. 19916–19926, 2020, doi: 10.1021/acsami.0c01663.

[122] E. Calzada, F. Grünauer, B. Schillinger, and H. Türck, "Reusable shielding material for neutron- and gamma-radiation," *Nucl. Instruments Methods Phys. Res. Sect. A Accel. Spectrometers, Detect. Assoc. Equip.*, vol. 651, no. 1, pp. 77–80, 2011, doi: 10.1016/j.nima.2010.12.239.

[123] N. Z. N. Azman, S. A. Siddiqui, R. Hart, and I. M. Low, "Microstructural design of lead oxide-epoxy composites for radiation shielding purposes," *J. Appl. Polym. Sci.*, vol. 128, no. 5, pp. 3213–3219, 2013, doi: 10.1002/app.38515.

[124] L. B. T. La, C. Leatherday, Y. K. Leong, H. P. Watts, and L. C. Zhang, "Green lightweight lead-free Gd2O3/epoxy nanocomposites with outstanding X-ray attenuation performance," *Compos. Sci. Technol.*, vol. 163, no. February 2017, pp. 89–95, 2018, doi: 10.1016/j.compscitech.2018.05.018.

[125] M. Mirzaei, M. Zarrebini, A. Shirani, M. Shanbeh, and S. Borhani, "X-ray shielding behavior of garment woven with melt-spun polypropylene monofilament," *Powder*

Technol., vol. 345, pp. 15–25, 2019, doi: 10.1016/j.powtec.2018.12.069.

[126] P. Mehnati, R. Malekzadeh, and M. Y. Sooteh, "Application of personal non-lead nano-composite shields for radiation protection in diagnostic radiology: a systematic review and meta-analysis," *Nanomedicine J.*, vol. 7, no. 3, pp. 170–182, 2020, doi: 10.22038/nmj.2020.07.0001.

[127] D. He *et al.*, "Complete-Lifecycle-Available, Lightweight and Flexible Hierarchical Structured Bi2WO6/WO3/PAN Nanofibrous Membrane for X-Ray Shielding and Photocatalytic Degradation," *Adv. Mater. Interfaces*, vol. 8, no. 7, pp. 1–13, 2021, doi: 10.1002/admi.202002131.

[128] S. N. Yılmaz, A. Güngör, and T. Özdemir, "The investigations of mechanical, thermal and rheological properties of polydimethylsiloxane/bismuth (III) oxide composite for X/Gamma ray shielding," *Radiat. Phys. Chem.*, vol. 170, no. November 2019, p. 108649, 2020, doi: 10.1016/j.radphyschem.2019.108649.

[129] M. V. Muthamma, S. G. Bubbly, S. B. Gudennavar, and K. C. S. Narendranath, "Poly(vinyl alcohol)–bismuth oxide composites for X-ray and γ-ray shielding applications," *J. Appl. Polym. Sci.*, vol. 136, no. 37, pp. 1–10, 2019, doi: 10.1002/app.47949.

[130] Z. Li, W. Zhou, X. Zhang, Y. Gao, and S. Guo, "High-efficiency, flexibility and lead-free X-ray shielding multilayered polymer composites: layered structure design and shielding mechanism," *Sci. Rep.*, vol. 11, no. 1, pp. 1–13, 2021, doi: 10.1038/s41598-021-83031-4.

[131] A. Pakdel, Y. Bando, and D. Golberg, "Plasma-assisted interface engineering of boron nitride nanostructure films," *ACS Nano*, vol. 8, no. 10, pp. 10631–10639, 2014, doi: 10.1021/nn5041729.

[132] A. Hezam, K. Namratha, Q. A. Drmosh, Z. H. Yamani, and K. Byrappa, "Synthesis of heterostructured Bi2O3–CeO2–ZnO photocatalyst with enhanced sunlight photocatalytic activity," *Ceram. Int.*, vol. 43, no. 6, pp. 5292–5301, 2017, doi: 10.1016/j.ceramint.2017.01.059.

[133] M. Nour *et al.*, “Nanocomposite carbon-PDMS membranes for gas separation,” *Sensors Actuators, B Chem.*, vol. 161, no. 1, pp. 982–988, 2012, doi: 10.1016/j.snb.2011.11.079.

[134] M. I. Shahzad *et al.*, “Study of carbon nanotubes based Polydimethylsiloxane composite films,” *J. Phys. Conf. Ser.*, vol. 439, no. 1, 2013, doi: 10.1088/1742-6596/439/1/012010.

[135] S. Fu, Z. Sun, P. Huang, Y. Li, and N. Hu, “Some basic aspects of polymer nanocomposites: A critical review,” *Nano Mater. Sci.*, vol. 1, no. 1, pp. 2–30, 2019, doi: 10.1016/j.nanoms.2019.02.006.

[136] M. A. Ashraf, W. Peng, Y. Zare, and K. Y. Rhee, “Effects of Size and Aggregation/Agglomeration of Nanoparticles on the Interfacial/Interphase Properties and Tensile Strength of Polymer Nanocomposites,” *Nanoscale Res. Lett.*, vol. 13, 2018, doi: 10.1186/s11671-018-2624-0.

[137] A. M. K. Esawi, K. Morsi, A. Sayed, M. Taher, and S. Lanka, “The influence of carbon nanotube (CNT) morphology and diameter on the processing and properties of CNT-reinforced aluminium composites,” *Compos. Part A Appl. Sci. Manuf.*, vol. 42, no. 3, pp. 234–243, 2011, doi: 10.1016/j.compositesa.2010.11.008.

[138] M. Jagannatham, P. Chandran, S. Sankaran, P. Haridoss, N. Nayan, and S. R. Bakshi, “Tensile properties of carbon nanotubes reinforced aluminum matrix composites: A review,” *Carbon N. Y.*, vol. 160, pp. 14–44, 2020, doi: 10.1016/j.carbon.2020.01.007.

[139] P. M. Ajayan and T. W. Ebbesen, “Nanometre-size tubes of carbon,” *Reports Prog. Phys.*, vol. 60, no. 10, pp. 1025–1062, 1997, doi: 10.1088/0034-4885/60/10/001.

[140] I. Ahmad, H. Cao, H. Chen, H. Zhao, A. Kennedy, and Y. Q. Zhu, “Carbon nanotube toughened aluminium oxide nanocomposite,” *J. Eur. Ceram. Soc.*, vol. 30, no. 4, pp. 865–873, 2010, doi: 10.1016/j.jeurceramsoc.2009.09.032.

[141] J. W. An and D. S. Lim, “Effect of carbon nanotube additions on the microstructure of hot-pressed alumina,” *J. Ceram. Process. Res.*, vol. 3, no. 3 PART 2, pp. 201–204, 2002.

[142] R. K. Abu Al-Rub, A. I. Ashour, and B. M. Tyson, “On the aspect ratio effect of multi-

walled carbon nanotube reinforcements on the mechanical properties of cementitious nanocomposites," *Constr. Build. Mater.*, vol. 35, pp. 647–655, 2012, doi: 10.1016/j.conbuildmat.2012.04.086.

[143] Y. Shang *et al.*, "Multilayer polyethylene/ hexagonal boron nitride composites showing high neutron shielding efficiency and thermal conductivity," *Compos. Commun.*, vol. 19, no. March, pp. 147–153, 2020, doi: 10.1016/j.coco.2020.03.007.

[144] X. Zhang, X. Zhang, and S. Guo, "Simple approach to developing high-efficiency neutron shielding composites," *Polym. Eng. Sci.*, vol. 59, no. s2, pp. E348–E355, 2019, doi: 10.1002/pen.25065.

[145] S. Furukawa *et al.*, "Space Radiation Biology for 'Living in Space,'" *Biomed Res. Int.*, vol. 2020, 2020, doi: 10.1155/2020/4703286.

[146] F. A. Cucinotta, M. Alp, F. M. Sulzman, and M. Wang, "Space radiation risks to the central nervous system," *Life Sci. Sp. Res.*, vol. 2, pp. 54–69, 2014, doi: 10.1016/j.lssr.2014.06.003.

[147] F. Krumeich, "Properties of Electrons, their Interactions with Matter," *ETH Zurich*, no. 1, pp. 1–24, 2015, [Online]. Available: www.microscopy.ethz.ch.

[148] S. Chen, "Polymer Based Nanocomposites as Multifunctional Structure for Space Radiation Shielding : A Study of Nanomaterial Fabrications and Evaluations by," 2018.

[149] Q. Li *et al.*, "Enhanced Radiation Shielding with Conformal Light-Weight Nanoparticle-Polymer Composite," *ACS Appl. Mater. Interfaces*, vol. 10, no. 41, pp. 35510–35515, 2018, doi: 10.1021/acsami.8b10600.

[150] J. H. Kang, S. H. Oh, J. Il Oh, S. H. Kim, Y. S. Choi, and E. H. Hwang, "Protection evaluation of non-lead radiation-shielding fabric: preliminary exposure-dose study," *Oral Radiol.*, vol. 35, no. 3, pp. 224–229, 2019, doi: 10.1007/s11282-018-0338-8.

[151] N. J. AbuAlRoos, N. A. Baharul Amin, and R. Zainon, "Conventional and new lead-free radiation shielding materials for radiation protection in nuclear medicine: A review,"

Radiat. Phys. Chem., vol. 165, no. August, 2019, doi: 10.1016/j.radphyschem.2019.108439.

[152] Q. Li, R. Zhong, X. Xiao, J. Liao, X. Liao, and B. Shi, "Lightweight and Flexible Bi@Bi-La Natural Leather Composites with Superb X-ray Radiation Shielding Performance and Low Secondary Radiation," *ACS Appl. Mater. Interfaces*, vol. 12, no. 48, pp. 54117–54126, 2020, doi: 10.1021/acsami.0c17008.

[153] O. Zare, R. Afzalipour, and M. S. Golvardi Yazdi, "Review of Alloy Containing Bismuth Oxide Nanoparticles on X-Ray Absorption in Radiology Shields," *Dis. Diagnosis*, vol. 11, no. 1, pp. 31–35, 2022, doi: 10.34172/ddj.2022.07.

[154] H. Nallabothula, Y. Bhattacharjee, L. Samantara, and S. Bose, "Processing-Mediated Different States of Dispersion of Multiwalled Carbon Nanotubes in PDMS Nanocomposites Influence EMI Shielding Performance," *ACS Omega*, vol. 4, no. 1, pp. 1781–1790, 2019, doi: 10.1021/acsomega.8b02920.

[155] J. Yang, X. Li, C. Liu, E. Rui, and L. Wang, "Effects of electron irradiation on LDPE/MWCNT composites," *Nucl. Instruments Methods Phys. Res. Sect. B Beam Interact. with Mater. Atoms*, vol. 365, pp. 55–60, 2015, doi: 10.1016/j.nimb.2015.04.013.

[156] M. Salahchini Javanmardi and E. Ameri, "Pervaporation characteristics of PDMS/PMHS nanocomposite membranes inclusive multi-walled carbon nanotubes for improvement of acetic acid–methanol esterification reaction," *Polym. Bull.*, vol. 77, no. 5, pp. 2591–2609, 2020, doi: 10.1007/s00289-019-02875-z.

[157] B. Zhang, B. Li, and S. Jiang, "Poly(phenylmethylsiloxane) functionalized multiwalled carbon nanotube/poly(dimethylsiloxane) nanocomposites with high piezoresistivity, low modulus and high conductivity," *J. Mater. Sci. Mater. Electron.*, vol. 28, no. 9, pp. 6897–6906, 2017, doi: 10.1007/s10854-017-6390-z.

[158] S. S. Batool *et al.*, "Study of electric conduction mechanisms in bismuth silicate nanofibers," *Sci. Rep.*, vol. 10, no. 1, pp. 1–11, 2020, doi: 10.1038/s41598-020-59563-6.

[159] I. I. Kabir *et al.*, "PDMS/MWCNT nanocomposite films for underwater sound absorption

applications," *J. Mater. Sci.*, vol. 55, no. 12, pp. 5048–5063, 2020, doi: 10.1007/s10853-020-04349-4.

[160] O. M. Ntwaeaborwa, G. H. Mhlongo, S. S. Pitale, M. S. Dhlamini, R. E. Kroon, and H. C. Swart, "Cathodoluminescence Properties of SiO2: Ce3+,Tb3+, SiO2:Ce3+, Pr3+ and SiO2: PbS," *Cathodoluminescence*, no. June 2014, 2012, doi: 10.5772/35100.

[161] Y. H. Zhao, Z. K. Wu, and S. L. Bai, "Study on thermal properties of graphene foam/graphene sheets filled polymer composites," *Compos. Part A Appl. Sci. Manuf.*, vol. 72, pp. 200–206, 2015, doi: 10.1016/j.compositesa.2015.02.011.

[162] M. Usta, "Continuous slowing-down approximation ranges of biological materials for 0.05-10 MeV alpha particles by using different approach methods," *Appl. Radiat. Isot.*, vol. 178, no. December 2020, p. 109951, 2021, doi: 10.1016/j.apradiso.2021.109951.

[163] T. Sainsbury *et al.*, "Oxygen radical functionalization of boron nitride nanosheets," *J. Am. Chem. Soc.*, vol. 134, no. 45, pp. 18758–18771, 2012, doi: 10.1021/ja3080665.

[164] M. T. Huang and H. Ishida, "Surface study of hexagonal boron nitride powder by diffuse reflectance Fourier transform infrared spectroscopy," *Surf. Interface Anal.*, vol. 37, no. 7, pp. 621–627, 2005, doi: 10.1002/sia.2055.

[165] P. M. Sudeep *et al.*, "Functionalized boron nitride porous solids," *RSC Adv.*, vol. 5, no. 114, pp. 93964–93968, 2015, doi: 10.1039/c5ra19091f.

[166] C. Y. Zhi, Y. Bando, T. Terao, C. C. Tang, H. Kuwahara, and D. Golberg, "Chemically activated boron nitride nanotubes," *Chem. - An Asian J.*, vol. 4, no. 10, pp. 1536–1540, 2009, doi: 10.1002/asia.200900158.

[167] V. Yadav and V. Kulshrestha, "Boron nitride: A promising material for proton exchange membranes for energy applications," *Nanoscale*, vol. 11, no. 27, pp. 12755–12773, 2019, doi: 10.1039/c9nr03094h.

[168] M. I. Dobynde, Y. Y. Shprits, A. Y. Drozdov, J. Hoffman, and J. Li, "Beating 1 Sievert: Optimal Radiation Shielding of Astronauts on a Mission to Mars," *Sp. Weather*, vol. 19,

no. 9, pp. 1–13, 2021, doi: 10.1029/2021SW002749.